UNIVERSITY OF OKLAHOMA
GRADUATE COLLEGE

COLD NITRIC OXIDE MOLECULES FROM A STARK GUIDE

A Dissertation
SUBMITTED TO THE GRADUATE FACULTY
in partial fulfillment of the requirements for the
degree of
Doctor of Philosophy

By

Bryan J. Bichsel

Norman, Oklahoma

2005

UMI Number: 3179078

UMI Microform 3179078

ProQuest Information and Learning Company
300 North Zeeb Road
P.O. Box 1346
Ann Arbor, MI 48106-1346

COLD NITRIC OXIDE MOLECULES FROM A STARK GUIDE

A Dissertation APPROVED FOR THE
DEPARTMENT OF PHYSICS AND ASTRONOMY

By

Eric R. I. Abraham

Chung-Lin Kao

Michael Morrison

James Shaffer

Neil Shafer-Ray

Ralph Wheeler

Dedication

To Jacob and Tyler

Acknowledgements

First, I would like to thank my advisors Dr. Eric Abraham and Dr. Neil Shafer-Ray for giving me the opportunity to be a part of an exciting experiment. The knowledge that they have imparted on me has allowed me to develop as a physicist in ways that I never imagined. Second, I want to thank all the graduate and undergraduate students that have been a part of this project over the past four years. Especially, I want to thank Jason Alexander and Chris McRaven whose countless hours of help, advice, and companionship have made my time at OU unforgettable.

I would also like to thank my family. My parents, brother, and sister, who have always been there for me, pushing me to excel and offering their encouragement. My in-laws, who have made raising a family and going to graduate school a possibility. Jacob and Tyler, who have been willing to share me with something they do not even yet understand. Finally, Rebecca has been there for me through thick and thin. Without her, I would not be where I stand today, and it is her support and love that has made me the person I am.

Contents

Dedication **iv**

Acknowledgements **v**

Abstract **viii**

1 Introduction **1**

2 Cold Atoms and Molecules **3**
2.1 Techniques . . . 3
2.1.1 Atoms . . . 4
2.1.2 Molecules . . . 7
2.2 Applications . . . 9
2.2.1 Spectroscopy . . . 9
2.2.2 Measuring the EDM . . . 10

3 Properties of Molecules and the Stark Effect **12**
3.1 Structure of Diatomic Molecules . . . 13
3.1.1 Electron Terms . . . 13
3.1.2 Vibrational and Rotational Structure . . . 15
3.2 The Stark Effect . . . 23
3.3 Nitric Oxide . . . 25

4 Apparatus **31**
4.1 Source Chamber . . . 31
4.1.1 Cryogenic refrigerator . . . 32
4.1.2 Copper can assembly . . . 34
4.1.3 Manifold . . . 35
4.2 Guide . . . 36
4.3 Detection Region . . . 40
4.3.1 Detector . . . 40
4.3.2 Laser system . . . 41

5 Data Collection and Analysis **45**
5.1 Field Stabilized Molecular Rydberg Time of Flight 45
5.1.1 Rydberg States 46
5.1.2 Rydberg Time of Flight 49
5.2 Modeling the Speed Distribution 52
5.3 Another Collection Technique 55

6 Experiments: Producing Cold Molecular NO **56**
6.1 Output of a Hexapole Guide 57
6.2 Time of Flight Measurements 65
6.3 Producing Cold NO 70

7 Conclusion **81**

Bibliography **83**

Appendix A
Supplying NO to the Experiment 90
A.1 Construction 90
A.2 Operation 93

Appendix B
Dye Lasers 95
B.1 Operation 95
B.2 Optical setup and laser dye 97

Appendix C
Published work 101

Abstract

The success of laser cooling and trapping led to an explosion of new physics and had a major impact on atomic physics. However, the requirement of particles with simple internal structure has limited its use to a few atomic species. Currently, atomic and molecular physicists are looking to expand the scope of cold and ultracold physics by developing new techniques that will produce cold samples of other atoms and molecules.

One possible technique is the use of a modified straight Stark guide to filter the slow moving molecules from a thermal source. Here I present such a technique and the design of the necessary apparatus. Furthermore, I present experimental results for creating a molecular source of nitric oxide (NO) whose temperature is controlled. Results showing the effects of the guide on the lowest ro-vibrational states of NO and a new technique for measuring the speed distribution of a cold molecular sample are also discussed. Finally, the use of the guide to produce cold NO molecules at a temperature of 7 ± 2 K is described.

Chapter 1

Introduction

The development of laser cooling and trapping of atoms and the formation of Bose-Einstein Condensation[1, 2, 3] has led to an explosion of new physics. Both discoveries have received Nobel Prizes and produced an abundance of new fundamental and applied physics, including Fermi degenerate gases[4], atom lasers[5], atomic clocks[6], and atom interferometry[7]. However, due to limitations of laser cooling, only the alkali-metal atoms and a few other atoms have been cooled using this technique. Unfortunately, molecules and much of the periodic table have been left untouched.

Currently, atomic and molecular physicists are actively developing new techniques to expand the scope of cold ($T \lesssim 1$ K) and ultracold ($T \lesssim 1$ mK) physics to include molecules and other atoms. Some of these techniques are discussed in Chapter 2. One technique to produce cold molecules uses an electric or magnetic guide to extract the cold fraction or slow-moving particles from a Maxwell-Boltzmann distribution of a thermal source. This technique is applicable to both atoms and molecules provided the particle has a magnetic or an electric dipole moment, depending on the type of guide being used. Since many molecules and atoms have one

of these properties, the technique can be used with a wide variety of particles. In the experiments described below, applicable molecules must have a sufficient electric dipole moment and possible species include NH_3 (1.5 Debye)[8], CO (.1 Debye)[9], and OH (1.6 Debye)[10]. Furthermore, the technique is straightforward to implement and extremely low-cost when compared to other cooling techniques.

In the chapters that follow, I will discuss the use of this technique to produce cold nitric oxide (NO) molecules. In Chapter 3, the properties of molecules, specifically NO, are discussed. This chapter also contains a brief description of the Stark effect and how it pertains to NO. The design of the guide and apparatus used is described in Chapter 4.

Chapters 5 and 6 describe the experimental work that was done in order to show production of cold NO molecules. In Chapter 5, I discuss the data collection, analysis techniques, and a detailed explanation of a new application of Rydberg time of flight spectroscopy, namely the use of field stabilized Rydberg states to measure the velocity distribution of cold molecules. Finally, Chapter 6 shows the results of the experimental measurements.

Chapter 2

Cold Atoms and Molecules

2.1 Techniques

Atomic physicists have been developing techniques to cool atoms since the early 1980s. The first experiments involved cooling hydrogen using a helium-coated cell that is cooled to milliKelvin temperatures[11]. The development of laser cooling[12, 13, 14] made dramatic impact in cooling of the alkali metals and a few other atomic species. The use of these cooling techniques led to the design of magnetic traps[15] to contain and further cool atoms through the development of evaporative cooling[16, 17]. The combination of laser cooling, magnetic trapping, and evaporative cooling lead to the creation of Bose-Einstein Condensation[1, 2, 3]. Today, labs across the world use this combination of techniques to cool atoms. Recently, new techniques have been developed to produce distributions of cold atoms. These techniques include the use of a magnetic octupole filter[18, 19] and buffer gas cooling of atoms[20]. New techniques are also being developed to produce distributions of cold molecules (see reference [21]). These techniques include Stark slowing[22],

buffer gas cooling of molecules[23], the use of a rapid rotor source[24], inelastic collisional cooling[25], and velocity selection[26, 27]. Table 2.1 shows current results for these techniques. Two other techniques used to create cold molecules are photoassociation[28] and the use of Feshbach resonances[29]. Both of these techniques require laser cooled atoms in order to create cold molecules. Although these methods have been used to produce molecules with μK temperatures, the molecules to which this can be applied are limited to dimers and combinations of the alkali-metal atoms and a few other atoms. Since a main goal of the development of new techniques to create cold atoms and molecules is to expand the cold and ultracold regime to atoms and molecules other than those that can be laser cooled, photoassociation and Feshbach resonances are not discussed in this section.

2.1.1 Atoms

Laser cooling

Laser cooling is a method used for creating μK distributions of atoms. In a common approach, atoms travel in a region with six laser beams. These beams are oriented such that a set of two beams coincide with each of the three orthogonal axes. These lasers are detuned to the red of the atomic resonance line. Therefore, whichever direction an atom is propagating photons which opposes its motion are Doppler shifted into resonance, and thus absorbed most often. Through conservation of momentum, the absorbed photon's momentum reduces the atom's momentum, thus decreasing its velocity and translational energy. When the excited atom decays, a

photon is emitted in a random direction and the atom regains the momentum of the emitted photon. However, since the momentum lost is in the forward direction, and the momentum gained is in a random direction, the momentum gained can be averaged away. In order to do this, the atom must absorb tens of thousands of photons. For efficient laser cooling, the transition must be nearly closed-cycle, which means that all of the atoms decay to their original state. If this is not the case, then another laser (or lasers) is (are) used to re-pump the atoms back to the ground state from all the states to which the atoms can decay. For this reason, atoms with the simplest structure (alkali-metals) are the easiest to laser cool. This nearly closed-cycle requirement makes it difficult to apply laser cooling to molecules because of their complex internal structure (see Chapter 3).

Magnetic octupole guide

Another technique that has produced ultracold atoms uses an apparatus called a magnetic octupole guide and is applicable to all atoms that have a large magnetic dipole moment. This technique is based on the principle that slow moving atoms already exist in the speed distribution of an atomic beam. The magnetic octupole guide consists of a series of magnet arrays arranged in a 90-degree arc. This arrangement creates a continuous magnetic field that is zero at the center with a large barrier. This type pf field causes the low-field seeking atoms (particles whose energy increases with increasing field) to be guided around the arc, as they are repelled by the large electric field barrier. Meanwhile, the fast-moving particles collide with the walls, stick, and are filtered away. An advantage of this technique is that it does

Technique	*Species*	*Trans. temp.* (K)	*Beam vel.* (m/s)	*Number density*(cm^{-3})	*Ref.*
Stark	ND_3	0.025	15	10^7	[22]
slowing	CO	-	98	-	[32]
	OH	-	140	-	[33]
	YbF	-	270	-	[34]
Buffer gas	CaH	0.4	x	10^8	[23]
cooling	PbO, NH	4	x	10^{12}	[35]
	CaF	1.5	x	10^{13}	[36]
Rapid rotor	O_2	<10	-	-	[24]
Collisions	NO	0.4	-	-	[25]
Velocity	H_2CO, ND_3	a few K	-	-	[26]
selection	NO	7	46	-	this work

Table 2.1: Current experimental results for several techniques being used to create cold molecules. A "-" means that no value was given in the listed reference. A "x" means that this measurement is not applicable in the technique.

not require a "cooling" laser enabling the technique to be applied to atoms (and molecules) for which laser cooling is not possible. Currently, only cold Li [18] and Rb [19] atoms have been produced using this technique.

Buffer gas cooling

The use of a cold buffer gas to cool atoms is another technique currently being used and developed. Several different types of atoms have been cooled using this technique. These include Eu and Cr [20], Rb [30], and several of the rare earth atoms[31]. Since this technique is also applicable to molecules, an explanation of how these atoms are cooled can be found in Section 2.1.2.

2.1.2 Molecules

Stark slowing

One way to obtain high densities of cold molecules is using a supersonic expansion of molecules. The result of this expansion is a molecular beam with a narrow speed distribution. However, the velocities of the molecules in the lab frame are typically much greater than 250 m/s. Stark slowing [22, 32] is one method that has been developed to try to reduce these velocities. To do this an array of electric fields, called a Stark decelerator, is used to remove kinetic energy from polar molecules via the Stark effect. This occurs because as the molecules enter the electric fields their Stark energy is increased. Then, the fields are turned off rapidly, leaving the molecules at a lower velocity. This process is then repeated down the entire length of the decelerator, as the guides are turned on and off. The technique has successfully slowed ND_3[22] to 25 mK. Other molecules that have been slowed are CO[32], OH[33], and YbF[34].

Buffer gas cooling

As previously mentioned, buffer gas cooling has been used to cool both atoms and molecules[23, 35, 36]. Cooling is achieved through thermalization with a cold buffer gas, usually ^{3}He or ^{4}He. As the atoms or molecules elastically collide with the buffer gas, a small amount of its translational energy is carried away. To cool the molecules to sub-Kelvin temperatures requires hundreds of collisions. This means that the buffer gas must have a high density (10^{16}cm^{-3}) at a low temperature (0.25

K), which is why ^{3}He or ^{4}He is used. Once the atoms or molecules are cooled, they are loaded into a trap. This technique has been used to successfully cool CaH to 400 mK[23], PbO and NH to 4 K[35], and CaF to 1.5 K[36]. It is important to note that even though buffer gas cooling has been shown to be applicable to a wide variety of species, the current technique has a major disadvantage. The apparatus used to perform the experiments is large, complicated, and expensive, limiting its use to elite groups.

Other approaches

Other methods for producing cold molecules are the use of a rapid rotor source[37] and inelastic collisional cooling[25]. The common feature of these techniques is that their source of molecules is a supersonic expansion. In the rapid rotor technique, this source is mounted near a high-speed rotor. This rotor provides a means to shift the velocity distribution of the beam to slower or faster velocities. Using this technique, O_2 can be cooled to a translational temperature of 10 K[24]. The inelastic collision technique relies on the collision of molecules from the supersonic expansion with Ar atoms. Using this method, NO has been cooled to 400 mK[25].

Velocity selection

The method of state selection does not directly cool the molecules. Instead, it relies on the fact that in a room-temperature Maxwell-Boltzmann gas there exists a fraction of molecules that have translational energies in the sub-Kelvin range. This fraction can be filtered off by using an apparatus like the previously mentioned

magnetic octupole guide[18, 19] or an electric Stark guide [26, 38, 39]. Using this method, distributions of ND_3 and H_2CO at a few Kelvin[26] have been produced. The technique is relatively simple to implement as compared to other techniques, though it requires polar or paramagnetic molecules to be effective.

2.2 Applications

The development of laser cooling and trapping has led to a number of achievements, including Bose Einstein Condensation[1, 2, 3], Fermi degenerate gases[4], atom lasers[5], and atom interferometry[7]. Atomic and molecular physicists now wish to duplicate, improve, or develop new applications with cold molecules because molecules have a number of properties not found in atoms. For example, molecules have both vibrational and rotational degrees of freedom and posses both electric and magnetic dipole moments. In addition, there are proposed applications, specific to cold molecules, such as precision spectroscopy and a method to improve the precision in the measurement of the electric dipole moment (EDM) of the electron[35, 40, 41].

2.2.1 Spectroscopy

Molecular spectroscopic measurements are performed using a vapor cell or in a molecular beam. These measurements often involve examining single ro-vibrational levels and the precision of the measurement is limited by photon-counting statistics. In a vapor cell, the vapor pressure curve determines the total number density, while the Boltzmann distribution determines the population of individual rotational states.

Furthermore, attempts to increase the counting rate by raising the cell temperature lead to a larger number of rotational states being populated. In a molecular beam, the molecules are typically cold, both internally and translationally, in a moving frame. However, the beam velocity is very high in the lab frame, limiting the measurements to the time, it takes the molecules to transverse the apparatus, which affects photon statistics. Using molecules that are cold in both the moving and lab frames results in an increase in the populations of the lowest rotational levels. In addition, since the molecules are moving slowly, their interaction times are increased. These properties would allow for improvements in ultra-high resolution molecular spectroscopy and are relevant to the study of molecular structure. For example, cold molecules could be used to study highly forbidden transitions.

2.2.2 Measuring the EDM

One particular application of precision spectroscopy is its use on heavy (high-Z atom) molecules, such as PbO[40] and YbF[41], to determine the value of the electric dipole moment (EDM) of the electron. Currently, the published experimental upper bound on the measurement is $1.8 \times 10^{-27} e$ cm[42] and has already narrowed the number of theoretical predictions beyond the standard model[43]. The use of molecules to make this measurement could further reduce this bound for several reasons. First, the EDM measurement requires that an unpaired electron be subject to an extremely large electric field. For molecules like PbO and YbF, the internal fields are very large, thus reducing the external fields needed. Second, the measurement requires that this

field be orient able. For molecules, the internal field is oriented in the laboratory frame by orienting the molecular axis. Finally, using cooled molecules increases the measurement times in the ground rotational state, leading to better statistics.

Chapter 3

Properties of Molecules and the Stark Effect

Diatomic molecules are good candidates for cooling because, while they are more complicated than atoms, their structure is relatively simple as compared to polyatomic molecules. As the complexity of a molecule increases, the complexity of the internal structure also increases. This means that there are more states that are populated at low temperatures. Since most techniques only produce cold particles using one or a few number of states, this complex internal structure can lead to a reduction in the population of the state being cooled. To avoid this, many methods used to obtain cold molecules, including the one presented in this work, use diatomic molecules.

In this chapter, I will first briefly discuss the structure of diatomic molecules. A more sophisticated approach can be found in references [44, 45, 46, 47]. Next, I will discuss the general form of the Stark effect and how it effects the molecular structure of diatomic molecules. Finally, in Section 3.3, I will examine the properties of NO and will discuss the reasons for choosing NO. The structure of NO and the requirements for allowed transitions will also be discussed.

3.1 Structure of Diatomic Molecules

The description of the internal structure of molecules is significantly more complicated than that of a single atom. However, this description is simplified by the fact that the nuclei are much more massive than the electrons, thus their motion is much slower. This means that the motion of the electrons can be considered to be about fixed nuclei that are separated by a given distance. This large difference in mass also allows the electronic and nuclear motions to be treated independently. The discussion presented in Sections 3.1.1 and 3.1.2 is an overview of similar chapters in references [44, 45, 46, 47].

3.1.1 Electron Terms

I will begin by examining the electronic motion in diatomic molecules. For all molecules, the Born-Oppenheimer potential energy curves associated with the electronic energy are called the electron terms of the molecule. In the general molecular case, the electron terms are a function of the distances between nuclei in the molecule and the energy due to the electrostatic interaction between nuclei. In diatomics, however, the description of the energy levels is simpler because there are only two nuclei and thus the energy levels are only a function of the internuclear distance r.

$$U(r) \equiv \text{Energy due to electronic motion.} \tag{3.1}$$

Recall that in atoms the value of the electronic orbital angular momentum L is used to classify the atomic terms. In molecules, L is not conserved because the electric field due to multiple nuclei is not spherically symmetric. However, in diatomics, the field is symmetric about the internuclear axis $\hat{n}$. This means that the projection of L onto this axis is conserved. The absolute value of this projection is denoted by Λ and takes the values

$$\Lambda = 0, 1, 2, \ldots . \tag{3.2}$$

Analogous to the atomic term classification, where increasing values of L (i.e. 0, 1, 2, 3, etc.) correspond to the letters S, P, D, F, etc., the same values of Λ are represented by the corresponding Greek letters. That is, if $\Lambda = 0, 1, 2$, then the corresponding term letters are Σ, Π, and Δ.

Each electron term is characterized by the total spin S of all the electrons in the molecule. The degeneracy, or multiplicity, of the term is given by $2S+1$. This value is written as a superscript before the term letter so that the term symbol appears as

$$^{2S+1}\Lambda. \tag{3.3}$$

Therefore, the symbol $^2\Pi$ denotes a term with $\Lambda = 1$ and $S = \frac{1}{2}$.

Due to the intrinsic symmetry of diatomic molecules, it is possible to rotate them through any angle about the internuclear axis without changing their electronic energy. This symmetry also allows for reflections in any plane that contains the

internuclear axis. If such a reflection is made, then the energy of the molecule also goes unchanged. However, the new state of the molecule is not identical to the original state. Such a reflection changes the direction of the projection of the electronic orbital angular momentum. Thus, electronic terms with $\Lambda \neq 0$ are doubly degenerate. That is, for each value of the energy, there correspond two states that differ only by the direction of Λ. For the case when $\Lambda = 0$, the terms are not degenerate. In this case, a reflection of the molecule only changes the wave function by the multiple of a constant. Since a double reflection must return the molecule to its original state, this constant is ± 1. To distinguish between terms whose wave function change sign upon reflection and those that do not, a superscript "-" is placed after the term for the former (i.e. Σ^-) and a superscript "+" for the latter (i.e. Σ^+).

3.1.2 Vibrational and Rotational Structure

I now consider the nuclear motion of the molecule for a given electronic state. This motion consists of translations of the molecule, rotations of the molecule about its center of mass, and vibrations of the nuclei about their equilibrium position. The translational motion can be disregarded by simply fixing the center of mass. This means that the molecule moves like a free particle in the absence of external fields.

The simplest type of molecules to examine when describing rotational and vibrational structure are those that have total spin of zero. For these molecules, the

rotational motion can be reduced to the motion of a particle, with mass μ[48], moving in a potential field. In this case, the effective potential is given by

$$U_{\mathcal{E}} = U(r) + U_c \tag{3.4}$$

where U_c is the centrifugal or rotational potential energy. The rotational Hamiltonian is then given by

$$H_r = \frac{\hbar^2}{2mr^2}(\vec{N} - \vec{L})^2. \tag{3.5}$$

Here $\vec{N}$ is the total orbital angular momentum excluding electronic and nuclear spin of the molecule, i.e.

$$\vec{N} = \vec{L} + \vec{R} \tag{3.6}$$

where $\vec{R}$ is the rotational angular momentum of the molecule. Operating on the given electron state (for a particular r), the rotational potential energy is given by

$$U_c = B(r)[N(N+1) - 2\vec{L}\cdot\vec{N} + \vec{L}^2] \tag{3.7}$$

where $B(r) = \frac{\hbar^2}{2mr^2}$. Here I have assumed that $\vec{N}$ is a good quantum number for the particular electronic state. Since Λ is also a good quantum number, one can determine that the final two terms in Eq. 3.7 are functions of r and independent of

$\vec{N}$. Thus, by including these in the electron energy term U(r), the effective potential becomes

$$U_{\mathcal{E}} = U(r) + B(r)N(N+1). \tag{3.8}$$

The vibrational motion in the molecule is due to vibrations of the nuclei about their equilibrium positions. To calculate the change in the effective potential due to this motion, a power series expansion of U(r) about $\delta = r - r_e$, where r_e is the equilibrium distance, is used. This expansion yields

$$U(r) = U_e + \frac{1}{2}\mu\omega_e^2\delta^2 \tag{3.9}$$

where $U_e = U(r_e)$ and ω_e is the vibrational frequency. Note that this approximation is only valid for low-lying vibrational states and molecules whose electronic energy can be approximated by a simple harmonic potential. This leads to an effective potential of

$$U_{\mathcal{E}} = U_e + B_eN(N+1) + \frac{1}{2}\mu\omega_e^2\delta^2 \tag{3.10}$$

where $B_e = \frac{\hbar^2}{2mr_e^2}$ and is often called the rotational constant.

Solving the one-dimensional Schrödinger equation using this effective potential yields energy levels given by

$$E = U_e + B_eN(N+1) + \hbar\omega_e(v + \frac{1}{2}). \tag{3.11}$$

Here I have introduced the vibrational quantum number v, which takes the values $v = 0, 1, 2, \ldots$ and is used to denumerate the energy levels for a given value of N in increasing order. One can see from Eq. 3.11 that in this approximation the energy levels are made up of three parts. The first term corresponds to the electron energy E_{el}. The second term is the energy due to the rotation of the molecule or rotational energy E_{rot}, and the third term is the molecule's vibrational energy E_v due to vibrations of the nuclei within the molecule.

To determine the spacing between energy levels, consider the relationship of each term of Eq. 3.11 with the reduced mass μ. In the rotational term, B_e is proportional to $1/\mu$, which means that the interval between rotational levels $\Delta\mathrm{E}_{rot}$ is also proportional to $1/\mu$. For the vibrational term, which is the solution to the one-dimensional harmonic oscillator, ω_e is proportional to $1/\sqrt{\mu}$, and therefore, so is the vibrational level splitting $\Delta\mathrm{E}_v$. Finally, the electronic energy level separation $\Delta\mathrm{E}_{el}$ is independent of μ. Recalling that the nuclei are much more massive than the electrons, which means $\mu \gg \mathrm{m}_{el}$, where m_{el} is the electron mass, we find

$$\Delta E_{el} \gg \Delta E_v \gg \Delta E_{rot}. \tag{3.12}$$

This shows that the vibrational motion creates closely spaced energy levels in each electron term, while the rotational motion causes the vibrational levels to exhibit splitting.

I now consider diatomic molecules with non-zero spin S. These types of molecules are classified by a system known as Hund's cases. This system classifies the molecules

by the strength of the coupling of certain angular momenta of the molecule. However, molecules do not often fall into one case because different electronic terms fall into different Hund's cases. Furthermore, some molecules have electronic terms that fall into an intermediate case.

Hund's case (a)

In a Hund's case (a) molecule, the strongest couplings occur between the internuclear axis and the total spin, as well as the axis and the electronic orbital angular momentum. Recall, that the latter results in the projection of the electronic orbital angular momentum, denoted Λ, being a good quantum number. Similarly, for molecules in this case, the projection of S onto the axis, denoted Σ, is also a good quantum number. Σ takes the values $S, S-1, \ldots, -S$ and is considered positive if it points in the same direction as Λ. The sum of the two projections gives the total angular momentum of the electrons. This momenta is denoted by Ω and takes the values

$$\Omega = \Lambda + \Sigma, \Lambda + \Sigma - 1, \ldots, \Lambda - \Sigma. \tag{3.13}$$

Introducing Ω leads to a fine structure splitting of the electronic terms. This occurs because the electronic terms are already $2S+1$ degenerate, but now the $2S+1$ levels can have different values of Ω. Note that Ω is often written as a subscript to the symbol for the electron term. For example, for $\Lambda = 1$ and $S = \frac{1}{2}$, the possible terms are ${}^2\Pi_{1/2}$ and ${}^2\Pi_{3/2}$.

The rotational structure of the molecule is also affected by the coupling of S to the molecular axis. The rotational structure is characterized by the total angular momentum excluding nuclear spin $\vec{J}$ of the molecule. Thus,

$$\vec{J} = \vec{L} + \vec{S} + \vec{R}, \tag{3.14}$$

and takes the values

$$J \geq \mid \Omega \mid . \tag{3.15}$$

Knowing this, one can calculate the energy levels for the electronic terms associated with this case. This is done similarly to the previous derivation for terms with $S = 0$. However, in this case, the fine structure of the electronic terms must be taken into account. A detailed explanation of this is found in reference [44].

Hund's case (b)

Many of the electronic terms with Hund's case (b) classification have $\Lambda = 0$, which means they are Σ terms. In this case, the total spin is more strongly coupled to the rotational angular momentum of the molecule than to the molecular axis. Because of this, J, the total angular momentum excluding nuclear spin, and the total orbital angular momentum N are conserved. Furthermore, the two are related by

$$\vec{J} = \vec{N} + \vec{S}. \tag{3.16}$$

If the interaction between the spin and the axis is taken into account, then the energy levels split into $2S+1$ terms, which differ in their value of J. The range of J is given by

$$\mid N - S \mid < J < N + S. \tag{3.17}$$

It is important to note that this splitting is due to a different interaction for molecules with $S = \frac{1}{2}$. For $S \neq \frac{1}{2}$ molecules the splitting is due to the first order approximation of the spin-spin interaction. However, molecules with $S = \frac{1}{2}$ are not split by either the spin-orbit or spin-spin interaction, but by the interaction of the spin with the rotation of the molecule. The energy levels due to this interaction for a $^2\Sigma$ term are given by [44]

$$\begin{aligned} E &= U_e + B_e N(N+1) + \hbar\omega_e(v + \frac{1}{2}) \\ &\quad + \frac{1}{2}\gamma[J(J+1) - N(N+1) - S(S+1)], \end{aligned} \tag{3.18}$$

where γ is called the spin-rotation constant and is determined by the geometry of the molecule. Further discussion on how to calculate this energy and the energy level expressions for $\Lambda = 0$, $S = \frac{1}{2}$ molecules is found in references [44, 49].

Intermediate Hund's cases

The Hund's cases are ideal classifications in which many molecules can be approximately placed. However, there are molecules that fall in between two cases. These

molecules are said to have intermediate coupling. The most common intermediate coupling is between cases (a) and (b). An electronic term with this coupling has the characteristic that the interval between adjacent rotational levels increases with increasing rotational quantum number R. This means that for low rotational levels, the term is considered case (a), but when this interval becomes larger than the energy associated with interaction between the total spin and the internuclear axis, the electron term is then considered to be case (b).

Λ-doubling

As explained above, electron terms with $\Lambda \neq 0$ are doubly degenerate when the effects of the rotating molecule are ignored. However, when these effects are taken into account, there is an interaction between the electron state and the rotation. This interaction causes the doubly degenerate states to split into two closely spaced levels. These levels are often labeled e and f[50], and the effect is called Λ-doubling because it only occurs for electron terms with $\Lambda \neq 0$.

The change in energy caused by Λ-doublet splitting is calculated in references [44, 46, 47]. For electron terms with Λ=1, $S = \frac{1}{2}$, i.e. $^2\Pi$ states, and Hund's case (a) classification, the splitting is given by[46]

$$a(J + \frac{1}{2}), \quad \text{for} \quad \Omega = \frac{1}{2}, \tag{3.19}$$

$$b(J^2 + \frac{1}{4})(J + \frac{3}{2}), \quad \text{for} \quad \Omega = \frac{3}{2}, \tag{3.20}$$

where a and b are the Λ-doubling constants. The equations needed to determine these constants are also found in reference [46]. For Λ=1 terms with case (b) classification, the energy is given by[46]

$$cN(N+1), \tag{3.21}$$

where c is also a Λ-doubling constant. The numerical values of these Λ-doublet splittings are often on the order of a fraction of a cm^{-1}.

3.2 The Stark Effect

In the previous section, I described the structure of all molecules in the presence of no external fields. Now I will consider the effect of an external electric field on this structure. Specifically, I will examine the effects on a Hund's case (a) molecule. This type of molecule is discussed because the low-lying rotational levels of the ground state of nitric oxide (NO) fall into this classification.

Consider a static, homogeneous electric field of strength $\mathcal{E}$ that points along the z-axis in the lab frame. When this field interacts with the permanent electric dipole moment $\vec{\mu}$ of the molecule, the molecular Hamiltonian is perturbed by

$$-\vec{\mu} \cdot \vec{\mathcal{E}} = -\mu \mathcal{E} \cos\theta, \tag{3.22}$$

where θ is the angle between the dipole direction and the direction of $\vec{\mathcal{E}}$. From the symmetry properties of this perturbation, one finds that states with different values

of Ω cannot couple. However, the symmetry properties do allow the e and f states to couple.

In past literature[51, 52], the Stark effect in NO was calculated using either first-order or second-order perturbation theory. First-order theory, or the linear Stark effect, is valid when the Stark interaction energy is large compared to the Λ-doublet splitting. The quadratic Stark effect, which results from second-order perturbation theory, can be applied when the Stark energy is small compared to the Λ-doublet splitting. In this case, the linear Stark shift is zero because in this approximation the states are non-degenerate.

A third method of calculating the Stark effect in NO is introduced in reference [53]. This method models each Λ-doublet in NO as a two-state system and will henceforth be referred to as the two-state model. To determine the Stark shift, the two-state model diagonalizes the Stark Hamiltonian, Eq. 3.22, assuming only that the Λ-doublet splitting and the Stark energies are small compared to the interval between ro-vibronic levels. The resulting Stark shift of the energy levels of the e/f states due to this model is given by[53]

$$\Delta E^{\mathcal{E}}_{v,J,M_J,\Omega} = \frac{1}{2}\sqrt{4|H^{\mathcal{E}}_{v,J,M_J,\Omega}|^2 + (\Delta\epsilon^{fe}_{v,J,\Omega})^2}, \tag{3.23}$$

where $H^{\mathcal{E}}_{v,J,M_J,\Omega}$ is the Stark matrix element, which is given by

$$H^{\mathcal{E}}_{v,J,M_J,\Omega} = \langle e| - \mu\mathcal{E}\cos\theta\,|f\rangle \tag{3.24}$$

and $\Delta\epsilon^{fe}_{v,J,\Omega}$ is the Λ-doublet splitting. Therefore, the Stark energy is given by[53]

$$E^{e/f}_{v,J,M_J,\Omega} = E_{v,J,\Omega} \pm \Delta E^{\mathcal{E}}_{v,J,M_J,\Omega}, \tag{3.25}$$

where $E_{v,J,\Omega}$ is the zero-field energy of the ro-vibronic state, and the + sign corresponds to the f state and the - sign to the e state. These equations show that the Stark effect increases the energies of the upper (f) states and decreases the energies of the lower (e) states.

In the experiments described in Chapter 6, only the two-state model is accurate over the entire range of field strengths used. Although the quadratic Stark effect in NO is applicable at field strengths less than a few kV/cm, it breaks down above this limit. On the other hand, the linear Stark effect is valid only for high field strengths since it requires that the Stark shifts be greater than the Λ-doublet splitting. These points, as well as a thorough derivation of the Stark shifts that correspond to the these models, are found in reference [53] and Appendix C.

3.3 Nitric Oxide

The nitric oxide (NO) molecule was chosen for the experiments in Chapter 6 for several reasons. First, NO is one of the most thoroughly studied molecules and has a well characterized spectroscopy[54]. Second, it has a well established, sensitive detection scheme. In addition, NO is a polar molecule with a large enough dipole moment that it can be manipulated by electric fields. (In NO, the dipole moment of the

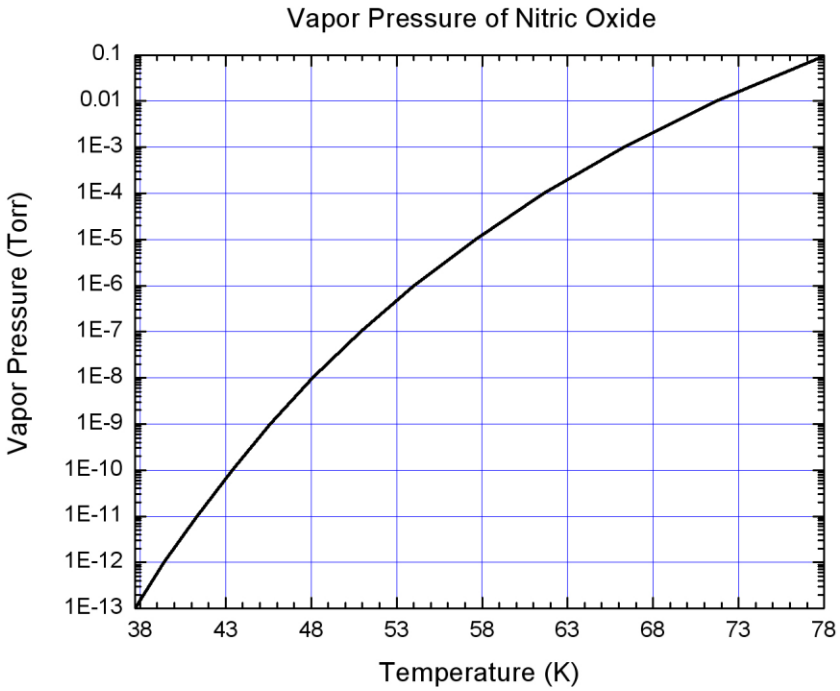

Figure 3.1: Vapor pressure curve of nitric oxide (NO)[58].

ground vibrational state has been determined experimentally to be approximately 0.15 Debye [55, 56, 57]). Another property that makes NO a desirable candidate is that it also has a magnetic dipole moment. This characteristic is not necessary for the experiments described here; however, any future work involving magnetic traps will make use of this quality. Finally, Figure 3.1 shows that NO has a high-vapor pressure at low temperatures. For example at 54K the vapor pressure of NO is 10^{-6} Torr. This allows NO to be cooled, via the process explained in Section 4.1.2, to well below 100 K and still be a viable source for the experiments.

Nitric oxide is a stable, open-shell molecule with an odd number of electrons and has a $^2\Pi$ ground state. In terms of the quantum numbers discussed earlier in this

chapter, this means that the ground state has $\Lambda = 1$ and $S = \frac{1}{2}$. The electronic spin-orbit interaction causes the state to have multiplet splitting, with $\Omega = \frac{1}{2}, \frac{3}{2}$. For NO, the $^2\Pi_{1/2}$ state is the lower state, and its lowest vibrational level is separated from the lowest vibrational state of the $^2\Pi_{3/2}$ state by approximately 123 cm^{-1}[47].

In the ground state of NO, the coupling between the internuclear axis and the total spin is strong enough that the state is classified, at least for low-lying rotational states, as Hund's case (a). In fact, the $^2\Pi_{3/2}$ state can be accurately described as Hund's case (a) for all rotational states. On the other hand, the $^2\Pi_{1/2}$ state is better classified by the intermediate (a)-(b) case. Recall, that in an electronic state with $\Lambda \neq 0$, the rotational levels are split into two nearly degenerate levels due to Λ-doublet splitting, which was first observed in NO in 1953[56]. These levels have opposite total parity, where the total parity operator inverts all spatial coordinates of all particles in a space fixed reference frame[49]. This splitting increases with increasing J and leads to the intermediate classification. However, low-lying rotational levels can be approximated as purely case (a). Finally, to describe the levels in the $^2\Pi_{1/2}$ ground state of NO, one only needs to know the vibrational (v), total angular momentum excluding nuclear spin (J), and Λ-doubling (e/f) quantum numbers, with the kets for this state given by $|v, J, e/f\rangle$. Using Eq. 3.25, the energy levels of these states as a function of field strength can be calculated. Figure 3.2 shows the results of this calculation for both the J = 1/2 and J = 3/2 rotational levels of the $^2\Pi_{1/2}$ state as well as the J = 3/2 and J = 5/2 levels of the $^2\Pi_{3/2}$ state. In both cases the ground vibrational level ($v = 0$) is considered.

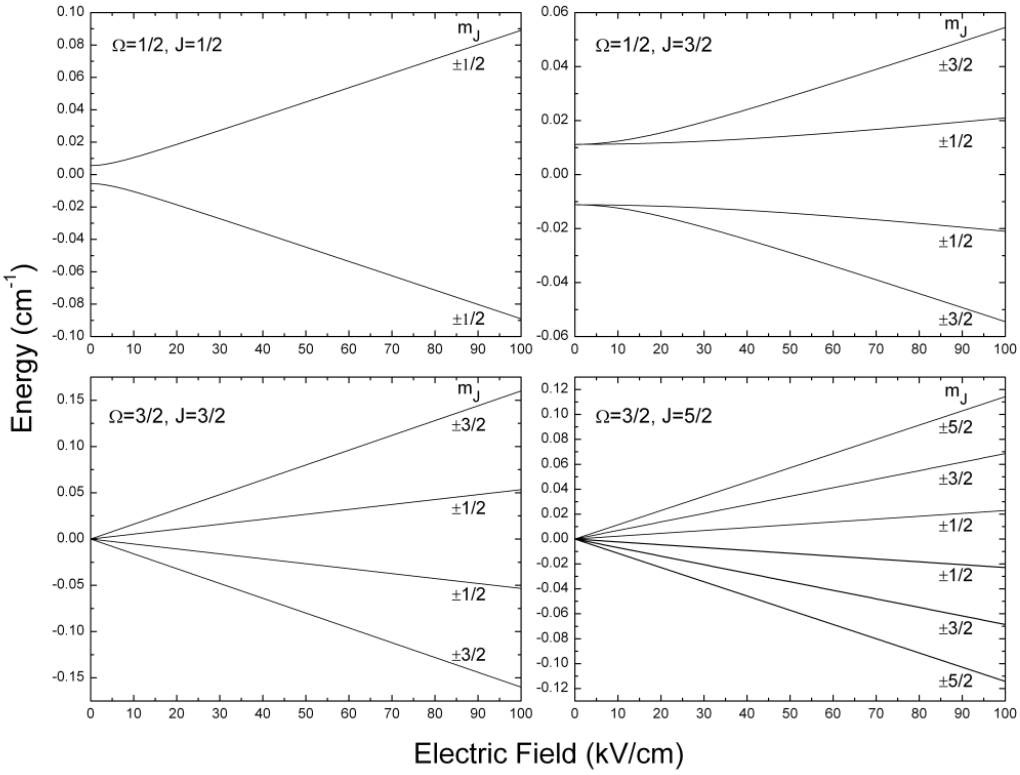

Figure 3.2: The dc Stark shift for the two lowest ro-vibronic levels of the $^2\Pi_{1/2}$ and $^2\Pi_{3/2}$ states of NO as a function of applied electric field strength. The states whose energy increase with increasing field strength correspond to the f state of the Λ-doublet and are said to be low-field seeking. Those whose energy decrease with increasing field strength correspond to the e state of the Λ-doublet and are said to be high-field seeking.[53].

In the experiments described in Chapter 6, the transition observed is from the $^2\Pi_{1/2}$ ground state, often called the X state, to the first electronically excited state, or A state, of NO. In the first electronically excited state, the projection of the electronic orbital angular momentum is $\Lambda = 0$ and the total spin is $S = \frac{1}{2}$, thus making it a $^2\Sigma$ state. This state can be accurately described as Hund's case (b) and, as mentioned above, exhibits a splitting due to the spin-rotation interaction. Recall that for a $^2\Sigma$ state N is a good quantum number. Therefore, as described previously, for each $N > 0$, there are two sublevels with different values of J but same total parity, given by

$$J = N - \frac{1}{2} \quad \text{and} \quad J = N + \frac{1}{2}. \tag{3.26}$$

The energy of the levels is determined using Eq. 3.18, and levels are described by the ket $|v, J, N\rangle$[39].

There are two dipole selection rules that govern transitions between ro-vibronic states in NO. One rule places a requirement on the change in the total angular momentum quantum number. It says that[50]

$$\Delta J = 0, \pm 1, \tag{3.27}$$

where the three values of $\Delta J = -1, 0, 1$ correspond to the P, Q, and R branches, respectively. This means that allowed transitions occur only between energy levels where this is the case. The second rule requires that the total parity of the final

state be the opposite of the total parity of the initial state. In the ground state, the total parity of the ro-vibronic states is determined by the parity of the Λ-doublet splitting, which alternate with increasing J. The total parity of the ro-vibrational levels of the first excited state is determined by $(-1)^N$.

Chapter 4

Apparatus

This section describes the apparatus used for the experiments outlined above. A considerable amount of time was devoted to the design and construction of the apparatus, optimizing functionality and changeability. The current apparatus consists of three regions: the source chamber, the guide, and the detection region. Figure 4.1 shows the entire schematic of this apparatus. The parts that make up each region as well as any operating techniques that are used for all experiments are described in detail.

4.1 Source Chamber

The source chamber is a 13 inch tee and contains the cryogenic refrigerator and the copper can assembly. A 250 l/s turbo pump pumps this tee, which is backed by a mechanical pump and, in conjunction with the refrigerator, is able to achieve pressures around 3×10^{-9} Torr. Another necessary part of the source chamber is the manifold, which controls the flow and pressure of incoming room temperature

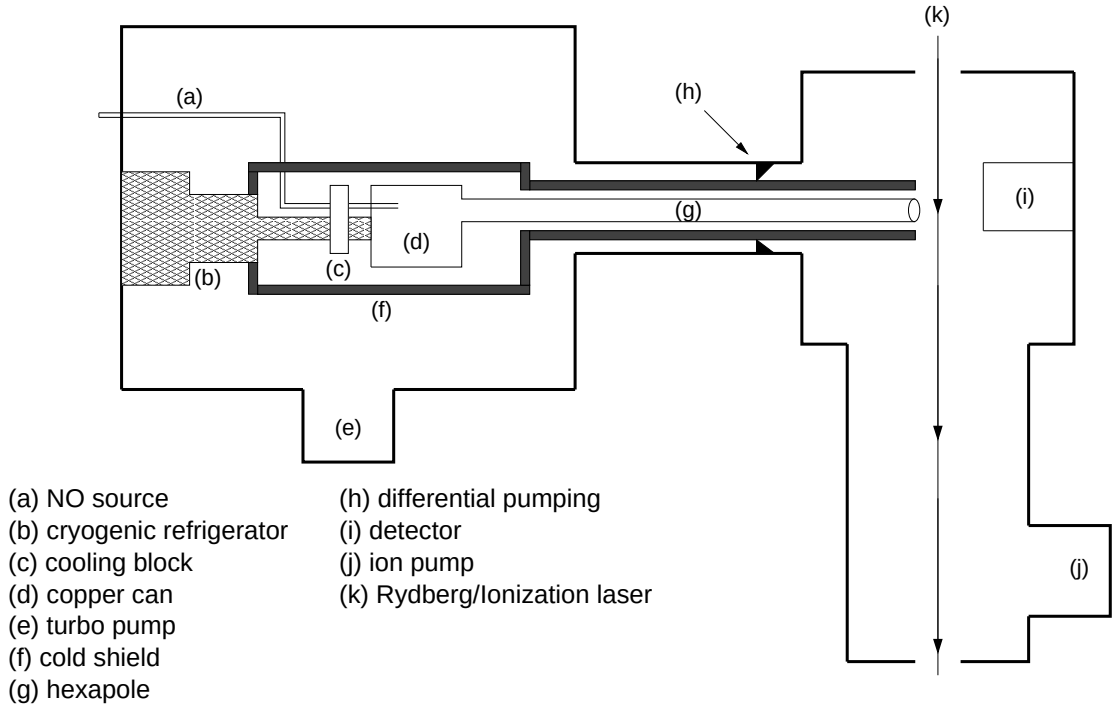

Figure 4.1: A schematic of the apparatus.

gas. A pair of resistive temperature sensors, a resistive heater, and a controller manufactured by LakeShore cryogenics monitors and controls the temperature of the internal system. By working simultaneously, these three apparatus and the control mechanism make it possible to control the temperature of the incoming molecule source.

4.1.1 Cryogenic refrigerator

The main cooling device in the source chamber is a cryogenic refrigerator (cryo pump) manufactured by Helix Technologies. The cryo pump has two stages. The first stage of the pump is capable of reaching temperatures near 4 K, while the second stage achieves temperatures near 77 K. This refrigerator works by compressing

helium gas using a piston mechanism located inside the refrigerator. Note that the temperatures mentioned above are only achieved when there is no load (other instrumentation) attached to the cryo pump. In order to reach similar temperatures with a load present, there are many factors that must be considered. First, the mass of the load must be minimized. Second, the surface area of the load that is in contact with the cryo pump must be maximized. Finally, expansion and contraction of the materials must be taken into account to ensure that the load stays in constant contact with the cryo pump. In order to ensure that this occurs, a thin layer of Indium foil is placed between the load and the stage of the cryo pump where the load is attached. A load with these specifications is cooled much more efficiently by the cryo pump, which leads to better cooling and temperature stabilization. The current apparatus also uses a radiation shield. The radiation shield is constructed from two copper cylinders and is attached to the second stage of the refrigerator. This "cold shield" reduces the amount of room temperature radiation that reaches the load, improving cooling.

In the apparatus, the cryo pump has three main purposes. First, it cools the incoming nitric oxide, which is explained in Section 4.1.2. Second, it cools the copper can assembly and guide, allowing for further thermal cooling of the incoming nitric oxide. Finally, it acts as a pump inside the source chamber, decreasing the pressure as particles out gassed from other parts of the apparatus stick to its surface. Overall, the cryo pump plays an important role in the cooling and creating of ultracold molecules.

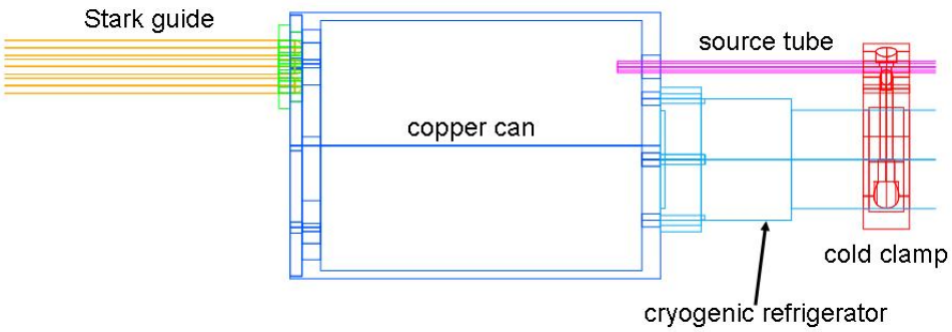

Figure 4.2: A design view of the copper can assembly.

4.1.2 Copper can assembly

Figure 4.2 shows the copper can assembly. This assembly consists of three parts: the source tube, the cold clamp, and the copper can. The source tube is a 1/8 inch outer diameter stainless steel tube that transports the NO from the manifold to the copper can. This tube has an inner diameter of 1/16 inch to reduce "freeze out" of the NO when the tube is cooled. "Freeze out" occurs when enough NO gas condenses on the walls of the tube and causes the output to be clogged or blocked, restricting flow. The tube is connected to the manifold using Teflon tubing to reduce heat transfer between the room and the source tube.

The source tube is cooled by clamping it to the cryo pump with a circular double clamp constructed from aluminum. The clamp is located between the two stages of the cryo pump, and a resistive temperature sensor connected to a resistive heater through a feedback loop controls its temperature. To maintain temperatures around 77 K, it is necessary to minimize the contact points between the clamp and the cryo pump. To do this, the inner surface of the clamp is grooved, leaving a 1/16 inch

ridge on either side for contact with the cryo pump. In addition to this detail, the resistive heater is attached using indium foil between its casing and the clamp. As the NO passes through the region where the clamp is attached, it thermalizes with the walls of the tube and is cooled to the desired temperature. With this design, I was able to set and maintain temperatures between 65 K and 90 K with 0.1 K precision.

The copper can consists of a 3 inch diameter copper cylinder that is 5 inches in length. The cylinder has a wall thickness of 1/16 inch and is closed at both ends. One end of the cylinder is removable and has a 1 inch bore that allows the guide to be attached (see Section 4.2). The other end of the can attaches to the cryo pump and has a 0.25 inch bore that allows for the insertion of the NO source tube. During normal operation, the can reaches a temperature of 16 K as measured on the removable face. The can's main purpose is to hold the guide and contain the incoming nitric oxide so that it cannot flow directly into the entire chamber.

4.1.3 Manifold

The manifold is an external system to the vacuum chamber that controls the flow and the input pressure of the nitric oxide. It is constructed from stainless steel VCR fittings and includes several bellows valves and a single needle valve (all manufactured by Swagelok). A Baratron gauge manufactured by MKS measures the pressure of the gas in the manifold. Under normal experimental operating conditions, the gas pressure begins at approximately 50 mTorr. However, this pressure may be increased

after long periods of operation to reciprocate for any "freeze out" that might occur. During operation, the needle valve is opened approximately one turn to allow for a minimum flow of NO to enter through the source tube. In the case of NO, a low flow rate is crucial to slow "freeze out" and to keep large numbers of $(NO)_2$ molecules from forming (dimerization). A more detailed schematic of the manifold as well as its operation procedure are found in Appendix A.

4.2 Guide

The guide region of the apparatus contains the most vital piece of equipment to the outcome of the experiments outlined above. The electric hexapole guide is located in this region. It is here that the Stark effect is used to skim the low-field seeking molecules. The hexapole guide consists of six straight, copper rods that are 0.48 m long and have a diameter of 3 mm. The end of each rod is hemispherically shaped, and the length of each has been polished. This construction is necessary to limit the amount of sparking between rods. The wires are held in a hexapole configuration, where the spacing between each wire center is 0.627 cm and the internal guide region has a diameter of 0.820 cm. Ceramic and Teflon spacers with the hexapole pattern cut into them hold the rods in this configuration. These spacers also provide electrical isolation for the rods from each other as well as from the walls of the cold shield. One of these spacers is constructed with a lip and is glued to one end of the guide. This spacer is then attached to the removable end of the copper can via the

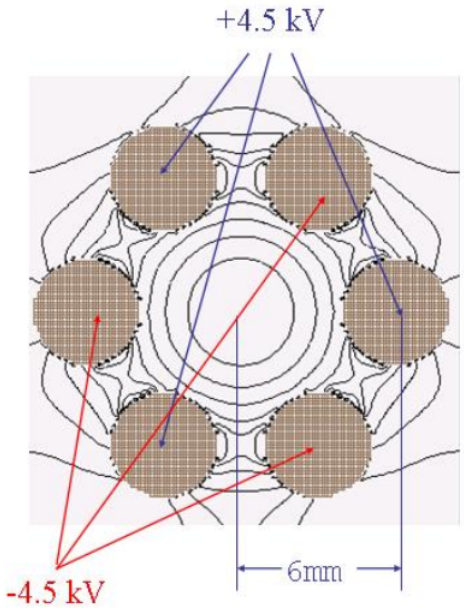

Figure 4.3: The electric field due to the hexapole guide with voltages of ± 4.5 kV.

1 inch bore using low-temperature epoxy. The design of the hexapole guide is based on previous work done by Stolte *et al.*[59, 60].

Figure 4.3 shows the electric field created by the hexapole. This field is created by placing a negative voltage on three rods and a similar positive voltage on three rods. The voltages are applied such that adjacent rods carry opposite voltages. This orientation leads to zero field at the center of the guide and high field barriers at the edges. The voltages are controlled externally and can range between ground and ±4.5 kV. In addition, under current pumping conditions, the guide can be switched between two different voltage sets without sparking. This voltage range creates a maximum field of 65 kV/cm.

The experiments described below used two different versions of the guide. For the experiments outlined in Sections 6.1 and 6.2, the guide was used in the configuration described above. In this configuration, there is nothing to block line of sight trajectories from the input to the output of the guide. As a result, this configuration yields more background NO in the detection chamber, which leads to a stronger overall signal. However, the increased background also makes it more difficult to identify features in the spectroscopy. To reduce the background molecules, differential pumping is used between the detection chamber and the guide region. This is done by placing an aluminum washer between the cold shield and the vacuum flange, leaving only the region in between the rods for pumping between the two regions.

For the creation of cold molecules using the hexapole guide, it is necessary to eliminate line of sight between the source and the guide exit. To do this, two modifications are made to the above configuration. First, a ceramic cap is placed over the guide exit. This cap has a 3 mm bore located on center and has the hexapole configuration cut into it. The cap is used to block any excess or stray molecules that do not exit from the center of the guide. The second modification is to add a copper sphere into the inner guide region. This sphere is 3 mm in diameter and is centered in the inner guide region at the middle of the guide. The sphere also has a 2 mm bore directly through its center, allowing molecules to pass through it when it is oriented such that the bore is in the direction of the rods. Figure 4.4 shows a photograph of the sphere. Furthermore, the sphere can be rotated using a magnetically coupled rotational stage that connects to a 1/32 inch rod off the top of the sphere. This rod,

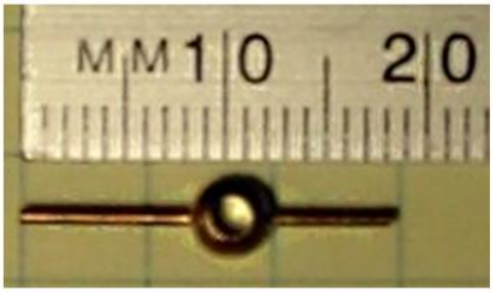

Figure 4.4: A photograph of the copper sphere used to block line of sight in the guide.

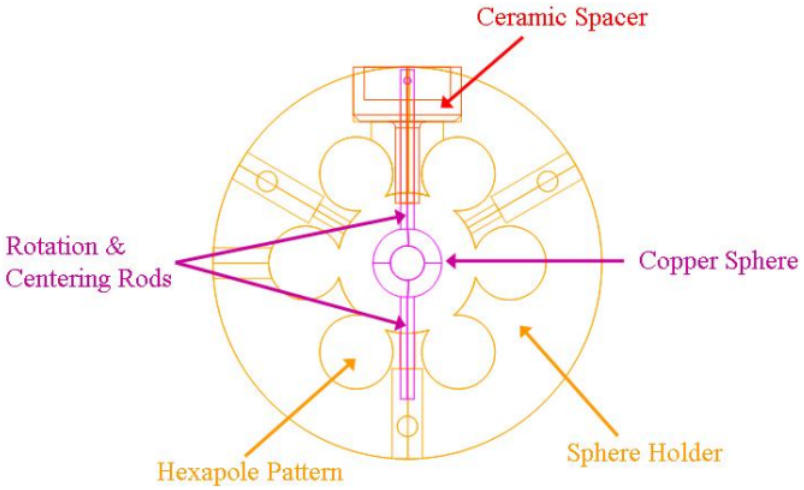

Figure 4.5: A front view of the sphere assembly. The yellow and red pieces are made of ceramic. The hexapole configuration is also shown.

along with a similar rod on the bottom of the sphere, is used to center the sphere in the guide region. To keep the sphere electrically isolated from the guide, it is located inside a ceramic spacer similar to those that hold the rods in the hexapole configuration (see Figure 4.5).

4.3 Detection Region

The detection region consists of two parts. The first is the vacuum chamber, which is constructed from an 8 inch cube and an 8 inch tee. A 270 l/s ion pump pumps this chamber. The ultimate pressure achieved in this part of the chamber is 5×10^{-9} Torr and varies only slightly while experiments are performed. Furthermore, this chamber houses the time of flight detector used to collect the experimental data. The second part of the detection region is the laser system used to create the appropriate wavelength light to perform the experiments.

4.3.1 Detector

As mentioned above, the type of detector used in the apparatus is a time of flight detector. Time of flight detectors work by using an electric field to accelerate ions towards a detector. This means that the signal collected from the anode of the detector can be plotted as a function of time. The detector consists of several different parts as seen in Figure 4.6. The design of this detector is similar in construction to the mass spectrometer built by Wiley *et al.* and only slightly different than the design by Xu *et al.*. The first section of the detector consists of two 3 inch diameter stainless steel plates, each with a 0.5 inch bore in its center. These plates are approximately 1/16 inch thick and are separated by 0.5 inch ceramic spacers that electrically isolate them from each other. A fine mesh screen covers the center bores to prevent field penetration from the guide. These plates are used to create pulsed fields ranging from 100 mV to 500 V that create and push ions as well as create

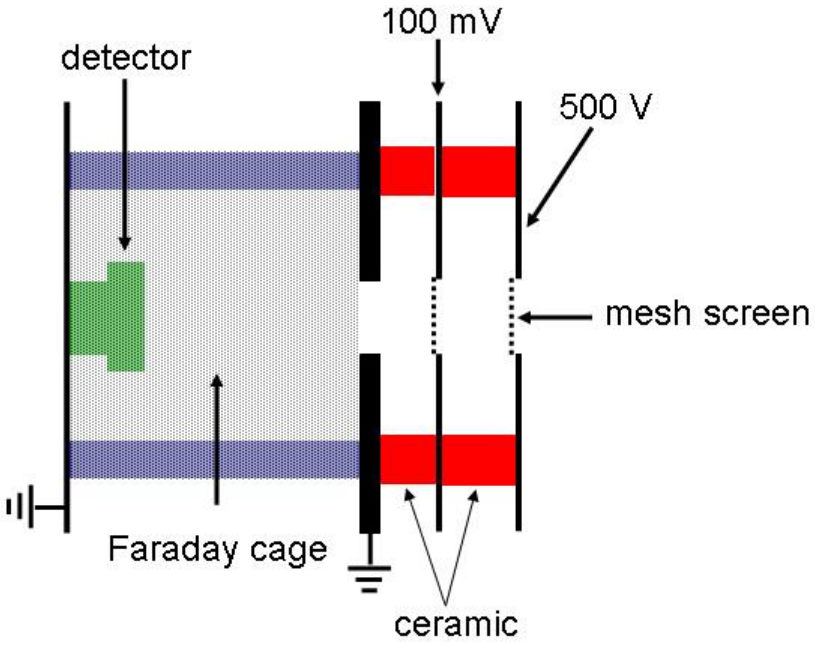

Figure 4.6: A side view of the detector.

long-lived Rydberg states. A third plate with similar dimensions is grounded and creates a field-free region where ions can drift. This field-free region is enclosed in a Faraday cage made from a cylinder of fine mesh screen. This cage prevents stray fields and stray particles from entering this region. The field free region ends at the collector, which was manufactured by Burle and can be heated to 300 °C. The collector contains a set of micro-channel plates (MCP) that operate at -2 kV. As positive ions hit the plate, a signal is created, which is viewed by attaching an oscilloscope to the anode of the detector.

4.3.2 Laser system

The second component of the detection region is the laser system. A schematic of the laser system, including the optical path, is shown in Figure 4.7. The setup includes

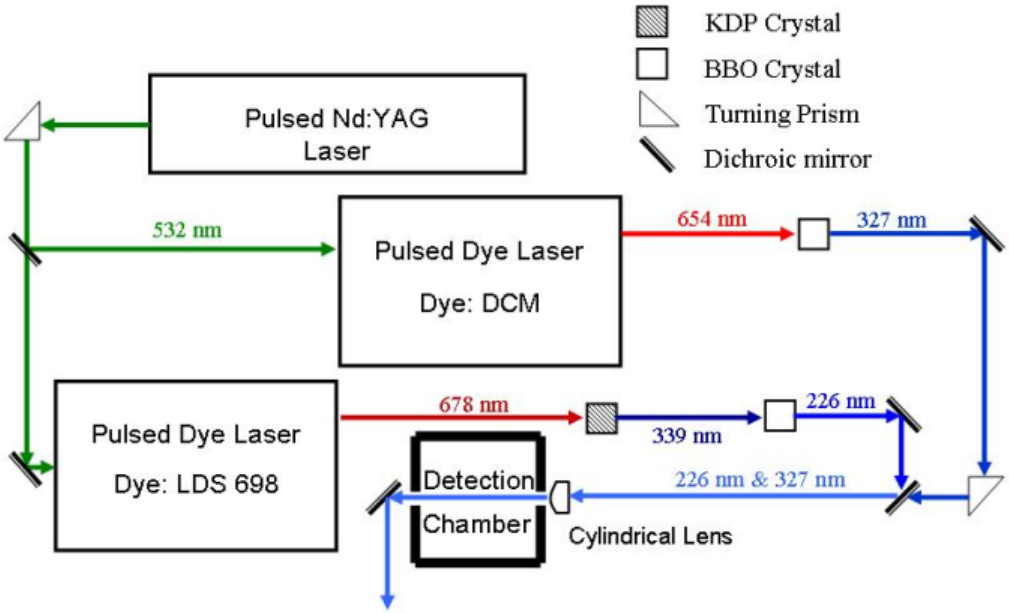

Figure 4.7: A schematic of the laser setup, including all optical components and lasers.

an Nd:YAG laser, two pulsed dye lasers (PDL), three crystals, and a variety of optics to shape and direct the beam. The Nd:YAG laser, manufactured by Continuum, fires with a frequency of 10 Hz and creates 10 ns pulses. The laser outputs both 1064 nm and 532 nm light; however, for the experiments performed here, only the latter is needed. A dichroic beam splitter splits the output of the Nd:YAG laser creating two beams with similar intensity. These two beams are then directed into the PDLs (one beam per PDL) where they pump a laser dye. The laser dyes used in the setup shown are DCM and LDS 698. Each PDL uses only one dye type. Two different dyes are chosen because two different wavelengths are needed for the performed experiments. These particular dyes are used because the center of their gain curves are near the needed wavelengths. Appendix B contains a detailed explanation on how dye lasers work, the internal optical setups that were used, and the gain curve of each dye.

Once lasing has been achieved in the PDLs, the output is directed along separate optical paths. For the PDL with LDS 698 dye (PDL-1), the output of the laser is tuned to 678 nm, which has a peak power of 5 mJ. However, light with a wavelength of 226 nm is needed for the experiments performed. To achieve this wavelength, a KDP crystal first doubles the output of PDL-1 to 339 nm. This doubled beam, along with the original, is then tripled to 226 nm using a BBO crystal. The efficency of this process is dependent on the intesity of the original laser beam and the angle the incident face of the crystal makes with the beam. Furthermore, a quarter waveplate must be placed between the two crystals to polarize the doubled light. Since the three beams are collinear, a system of dichroic mirrors is used to filter away most of the 678 nm and 339 nm light. Similarly, the output of the PDL with DCM dye (PDL-2) is tuned to 654 nm. At this wavelength, the peak power is 3 mJ. For the experiments described in Chapter 6, this output is doubled to approximately 327 nm using a BBO crystal. Again, a system of dichroic mirrors, as shown in Figure 4.7, is used to filter away most of the 654 nm light.

After each beam passes through separate dichroic mirror paths, the beams are overlapped using a turning prism and dichroic mirror. Then the beams are sent through a cylindrical lens system that vertically stretches the beam so it intersects the entire output of the guide. Furthermore, the lenses control the size of the beam at the center of the cube. For the 226 nm beam, the beam width is 150 μm and the height is 3 mm at the cube center, while the 327 nm beam has dimensions of 200 μm and 5 mm, respectively. These beams pass into and out of the cube through sapphire view ports that have 75% transmission for UV light. Finally, the

overlapped, cylindrically focused beams are centered between the two pulsed field plates with the focus at the center of the output of the guide.

Chapter 5

Data Collection and Analysis

In this chapter, I will discuss our techniques for data collection and analysis, concentrating on field stabilized molecular Rydberg time of flight, which is similar to the Rydberg time of flight techniques found in references [61, 62, 63, 64]. I will also discuss the development of the Monte Carlo code that is used for analyzing the data. Finally, the technique used when a measurement of the ion signal is needed is also discussed.

5.1 Field Stabilized Molecular Rydberg Time of Flight

In the experiments described in Sections 6.2 and 6.3, the speed distribution is measured using ion detection. Two challenges associated with measuring the speed distribution of the output of the Stark guide are (1), the density of the output is small and (2), the molecules exit the guide with low velocity. Therefore, to make this measurement, extremely sensitive detection is needed. Two common methods

for measuring the speed distributions are absorption and laser induced fluorescence (LIF) spectroscopy. However, absorption spectroscopy would require a continuous wave laser operating in the UV regime, which is extremely expensive and difficult to construct. Furthermore, LIF spectroscopy would require significant design changes of the apparatus as well as it is less sensitive than ion detection. Instead, the speed distribution is measured using ion detection. However, since the molecules that exit the guide are at low velocities, the ions are sensitive to stray fields within the detector. To overcome this, Rydberg time of flight spectroscopy[61, 62, 63, 64] is used. Unfortunately, the lifetime of molecular Rydberg states is not long enough to allow for the molecules to move significantly before they are ionized. To increase this lifetime, field stabilized Rydberg states are created by applying a small pulsed electric field, which causes mixing of the ℓ-levels of the Rydberg state. In this section, I will discuss the properties of Rydberg states that make this detection technique possible. In addition, I will explain Rydberg time of flight spectroscopy and how it is used with field stabilized Rydberg states of NO.

5.1.1 Rydberg States

A Rydberg state is a state of an atom or molecule where one of the electrons has been excited to an orbital, with large principle quantum number n, about the nucleus or nuclei that has a large mean radius. Classically, this new state is very similar to hydrogen because it appears to have one electron orbiting an ionic core. The quantum numbers used to describe Rydberg states are the principal quantum number

n, the orbital angular momentum quantum number ℓ, and the magnetic quantum number m. These three quantum numbers describe the orbital to which the electron has been excited. The principle quantum number denumerates the orbital and is very large for Rydberg states. On the other hand, the orbital angular momentum and the magnetic quantum numbers describe the shape of the orbit.

Spectroscopically, Rydberg states are often classified into sets of bound states. This set of states corresponds to a particular set of quantum numbers for the electron and the ionic core. This set of bound states is called a Rydberg series. When these states result from transitions to orbitals of a given type with successive values of n, the energies of the states are found by[65]

$$E_n = E_\infty - \frac{R}{(n-\delta)^2}, \tag{5.1}$$

where E_∞ is the ionization limit, R is the Rydberg constant for the system, and δ is called the quantum defect. The quantum defect describes how much the series deviates from the behavior of the Rydberg states of atomic hydrogen and is directly related to the interaction of the electron with the ionic core. Furthermore, the value of δ is dependent on the value of ℓ.

As stated, it is possible to create Rydberg states in both atoms and molecules. Both types of Rydberg states have many unusual properties compared to ground state atoms and molecules that make them valuable experimentally. These include that the excited electron is easily effected by external fields and collisions, the very

high degeneracy of the quantum states, and their extreme reactivity. Another invaluable property is that some Rydberg states can be (or made to be) long-lived. This property is much more common for Rydberg states of atoms. The reason for this is that the energy separation between the ground state and a high n Rydberg state of an atom is large compared to the frequency at which the electron orbits the ion core. Thus, it is difficult for this electron to decay to a non-Rydberg state.

In Rydberg states of molecules, the frequency of the electron's orbit is comparable to the interval between rotational levels. Therefore, unlike atoms, high n Rydberg states of molecules are not naturally long-lived. However, in 1988, Reiser *et al.*[66] unexpectedly observed molecular Rydberg states with long lifetimes. These results were explained by Chupka[67] in 1993, who suggested that the long-lived states occurred due to a mixing of the ℓ-states. This mixing is produced when a small dc electric field is applied to the system causing the Stark manifolds of a number of the n states to overlap. By doing this, it is possible to transform Rydberg states with low-ℓ into states with high-ℓ. The high-ℓ states have circular orbits, so are less likely to interact with the ion core.

In NO, the Rydberg state lifetime is limited by predissociation[68]. This means that the nitrogen molecule and oxygen molecule split before the dissociation limit, which is the energy where this normally occurs. This process is highly dependent on the orbital angular momentum ℓ of the electron of the Rydberg state. For low-ℓ states, i.e. ℓ=1, the predissociation rate is very fast. However, this rate is almost non-existent for high-ℓ, $\ell > 3$, states. Thus, to obtain long-lived Rydberg states of NO, it is necessary to transform the states as described above.

In 1998, A. Held *et al.*[69] developed a technique that would make this transformation in NO. The main mechanism of this technique is the use of fast switching electric fields to control the stabilization of the Rydberg states. This is done by turning on the electric field shortly before the Rydberg states are made and leaving it on for several nanoseconds after excitation. By doing this, the Rydberg states are left in a state with high-ℓ, thus increasing the state's lifetime. In the technique presented in reference [69], another electric field, which is perpendicular to the first, is also used to increase the lifetime of the states. This field mixes the m-states and when it is turned off, leaves the Rydberg states in stable high-m states. Finally, the technique was originally developed for ZEKE (Zero Electron Kinetic Energy) spectroscopy, but because the switching is fast, it is easily implemented into other photoelectron spectroscopy techniques like time of flight (TOF) spectroscopy.

5.1.2 Rydberg Time of Flight

Time of flight, or TOF spectroscopy[70] is a technique used to take measurements of distributions of particles by looking at the time it takes the particles to move a known distance. The mapping of these particles to a detector yields a spatial distribution of the particles. From this distribution, a speed distribution for the particles is determined, and the energy of the distribution can be determined. For sensitivity, the particles are ionized before they are detected. However, ions are effected by stray fields which can lead to errors in the measurement of the speed distribution.

In experiments involving atoms, the effect due to the stray fields is minimized by using Rydberg states[61, 62, 19]. The atoms are first excited to a Rydberg state where they are still neutral particles and are relatively unaffected by the stray fields. Then the Rydberg states expand spatially during a time delay due to their initial velocities. Finally, a pulsed electric field ionizes the Rydberg states and pushes them towards the detector where the spatial distribution is mapped. Thus, ions are still being detected, but now the atoms have time to expand without being significantly effected by the stray fields.

A similar technique for molecules[63, 64] has also been developed. However, the lifetime of the Rydberg states used was on the order of hundreds of nanoseconds, which is not long enough when detecting slow-moving molecules. Therefore, using a scheme similar to the one described in Section 5.1.1, we developed a technique that allowed us to measure the speed distribution of molecules. A schematic of the timing used to do this is shown in Figure 5.1, and Table 5.1 shows the time relationship between the different elements. Similar to the atomic case, the NO molecules are excited to a Rydberg state via the A state. As this occurs, a pulsed electric field of 100 mV is applied. Thus, the Rydberg states created are long-lived due to the mixing of the ℓ-states. The Rydberg states are then given time to expand spatially during a time delay (T_{delay}), which ends when the Rydberg states are field ionized by another pulsed electric field. This field also pushes the ions towards the detector where they are detected. Using the signal from the detector, a speed distribution for the particles is determined.

Time	*Events*
0	Stabilization pulse of 100 mV turns on
80 ns	Laser pulse excites molecules to Rydberg states
100 ns	Stabilization pulse turns off
T_{delay}+ 100 ns	Field ionization pulse turns on

Table 5.1: Time relationship between different elements of field stabilized molecular Rydberg time of flight spectroscopy.

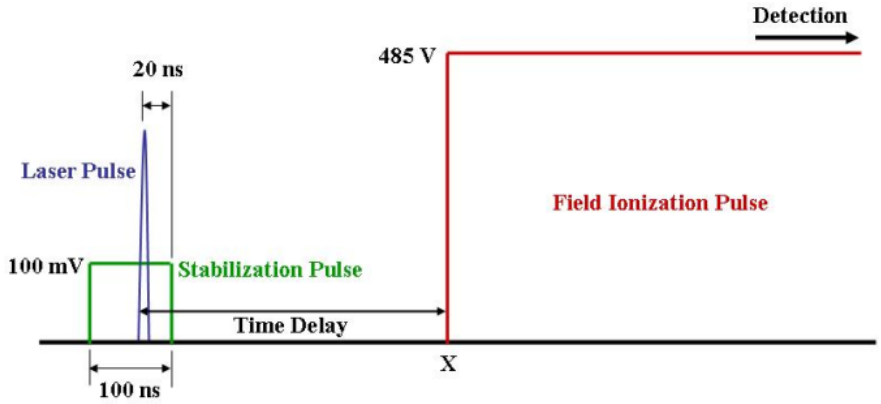

Figure 5.1: A schematic of field stabilized molecular Rydberg time of flight spectroscopy as used in the experiments described in Chapter 6. The 'X' represents location where time of flight measurement begins.

5.2 Modeling the Speed Distribution

Mapping the distribution of NO molecules out of the guide as a function of time of flight enables one to determine the speed distribution of the molecules. In turn, this speed distribution leads to a determination of the temperature distribution of the particles. To do this, a Monte Carlo model is used to create a theoretical spatial distribution based on a given speed distribution. A Monte Carlo model is used because it can model thousands, or sometimes millions, of data points at random.

The Monte Carlo simulation used to model the experimental data is based on three main functions. First, the simulation creates a speed distribution for a given temperature. This speed distribution has the form

$$f(v) = (\frac{m}{2\pi k_B T})^{3/2} v^2 e^{-\frac{mv^2}{2k_B T}}, \tag{5.2}$$

where m is the mass of the molecule, k_B is the Boltzmann constant, and T is the temperature of the distribution. Although we have an effusive source, this distribution is used because we measure a density of particles out of the guide, not a flux[71]. When the laser fires it only excites molecules within the volume of the laser beam, and thus only molecules in this volume are detected. This means that a density of particles is measured, and therefore, Eq. 5.2 is the appropriate speed distribution. The second element of the code is the time of flight function. This function is based on simple kinematics and involves the initial velocity and position of the molecules, as well as the accelerations due to stray fields and the field ionization pulse. This

function also determines whether or not the molecule becomes a Rydberg state or remains in a Rydberg state until the field ionization pulse. These first two functions are then combined with a third function, the Monte Carlo function. Here a molecule is given a randomly selected speed from the distribution based on the probability that that speed occurs. Then a random process determines if the molecule starts as a Rydberg state or an ion. This information is then passed to the TOF function where a TOF is determined and recorded for that particular molecule. This is repeated for 500,000 molecules. When the simulation is finished, the result is a theoretical spatial distribution for a particular temperature.

In this simulation, several parameters must be taken into account. These include the strengths of the stray field and the field ionization pulse, the location and size of the laser beam, the time delay between the laser firing and the field ionization pulse, and the fraction of ions that are present after the laser fires. Several of these parameters are measured within the experiment and are used directly in the simulation. The size of the laser beam is measured outside the chamber by recreating the beam path using the same optics used in the experiment and measuring its beam waist. This is done translating a knife-edge through the beam and measuring the beam intensity as a function of knife-edge position. This data can then be plotted and fit to an error function from which the beam waist can be calculated. The time delay is a set parameter that is determined (and manually set) by a digital timing box that controls the laser and pulse field timing. The fraction of ions that are a result of the laser firing is determined by counting the number of ions when only PDL-1 (the excitation laser) is firing. This number is then compared to the number

of counts with both lasers firing to determine the fraction. However, the position of the laser and the magnitudes and properties of the field ionization pulse cannot be measured while the experiment is running because the plates responsible for these fields reside in vacuum. These two parameters are determined by experimentally measuring the TOF for different spatial positions between the first two plates in the detection region. Using this measurement, a function of the time of flight as a function of position between the first two plates is determined. By numerically matching this "mapping" function to the previously discussed TOF function, these two parameters are found. Furthermore, the calibration is done using the shortest possible time delay because the molecules do not have time to expand spatially and the initial velocity is assumed to be zero.

Once these parameters are known, the simulation is then run given a range of temperatures and stray fields. The range of temperatures is determined based on the value of the source temperature used when the data is collected. For example, for source temperature of 77 K the temperature range that is used is 50-90 K. The initial range for the stray fields is $(-400mV) - 400$ mV. These values were determined by assuming that the stray field would be a fraction of the measured field ionization pulse. The first thing that the simulation does is pick a temperature from the range provided. Then for this temperature, the simulation steps through the range of stray field values, creating a spatial distribution for the longest time delay for each value. This is then repeated for a given number of temperatures in the range of values. Next, the spatial distributions are compared to the experimental data at the longest time delay. Using a χ^2 analysis between the two data sets, the value of the stray

field that has the smallest χ^2 value is recorded for each temperature. Then, for each value of the temperature and its corresponding stray field, spatial distributions for all of the time delays are created. These distributions are then compared to the experimental distributions, and another χ^2 analysis is performed. The value of each χ^2 fit for each time delay is plotted as a function of the temperature that corresponds to that fit. By examining these plots, the temperature of the distribution is determined. Note that unrealistic values of the temperature or stray field result in poor simulations. By using this characteristic of the simulation, the range of values for these two parameters can quickly be reduced.

5.3 Another Collection Technique

A time of flight detector is also used in the experiments where the speed distribution is not measured. In these experiments, the time of flight of the particles is not important when collecting the data. Instead, the detector is used to measure the number of ions that are a result of a given set of conditions. This type of collection is used in two different ways. In the first, the collection method is used to measure the spectroscopy of NO. To do this, the detector measures the strength of the signal as a function of laser wavelength. The second method measures the strength of the signal as a function of guide voltage. In both of these cases, the measurement is a result of averaging the signal from the detector. This averaging is done using the oscilloscope and is determined based on the strength of the signal and sensitivity required.

Chapter 6

Experiments: Producing Cold Molecular NO

As stated before, one way to produce cold atoms and molecules is to extract the slow-moving atoms or molecules from the Maxwell-Boltzmann speed distribution of a thermal source. As described in Section 2.1.1, this effect is achieved by directing an atomic or molecular beam into a bent, two-dimensional electric or magnetic guide. The only particles that can pass through the guide are moving slowly enough that they are repelled by the magnetic or electric fields that make up the walls of the guide. Particles that do not satisfy this condition leave the guide before reaching the output.

In this chapter, I discuss the use of this technique to produce cold NO. First, I will describe the initial experiments, which examined the relationship between the output of the Stark guide (with no sphere) and the guide voltage. In addition, I will discuss the results of similar experiments for the Stark guide containing the sphere. Next, determining the temperature of the source is discussed. Finally, I will discuss the production of cold NO molecules using the Stark guide with the sphere in place. Parts of this section appear in reference [39].

6.1 Output of a Hexapole Guide

Unlike the experiments discussed in Chapter 2 that use the technique described above (see references [18, 19, 26, 38]), we direct NO molecules into a straight hexapole Stark guide. As described in Section 4.2, this guide has a line-of-sight between the input and output, i.e. no sphere. However, particles not along this line-of-sight are guided if their kinetic energy is small compared to the Stark interaction energy. Because of this guiding, there is an increase in the number of low-field seeking molecules at the output of the guide. Furthermore, since the average thermal energy of the effusive source is large compared to the Stark interaction, only the cold fraction is guided.

The Stark guide is designed so that it has zero electric field at the center and a high electric field barrier at the edges (see Figure 4.3). Because of this, only the low-field seeking, or f states, of the $^2\Pi_{1/2}$ ground state of NO are guided, while the high-field seeking e states are not guided. However, both Λ-doublet states will reach the detector because the line-of-sight of the guide allows for non-guided molecules to traverse the length of the guide. The overall effect is an increase in the number of low-field seeking molecules and a decrease in the number of high-field seeking molecules that reach the detector. This effect is seen in Figure 6.1, which shows the molecular spectroscopy of NO for guide voltages of ± 4.5 kV and 0 kV. The two spectra are obtained by scanning PDL-1 over the shown frequency range, exciting transitions in the $\left|X^2\Pi_{1/2}, v'' = 0\right\rangle \rightarrow |A^2\Sigma, v' = 0\rangle$ band. The second laser is tuned to a frequency of 30581.04 cm^{-1} and ionizes the NO molecules from the A state. The theoretical values of allowed transitions from the ground state to the first electronically excited

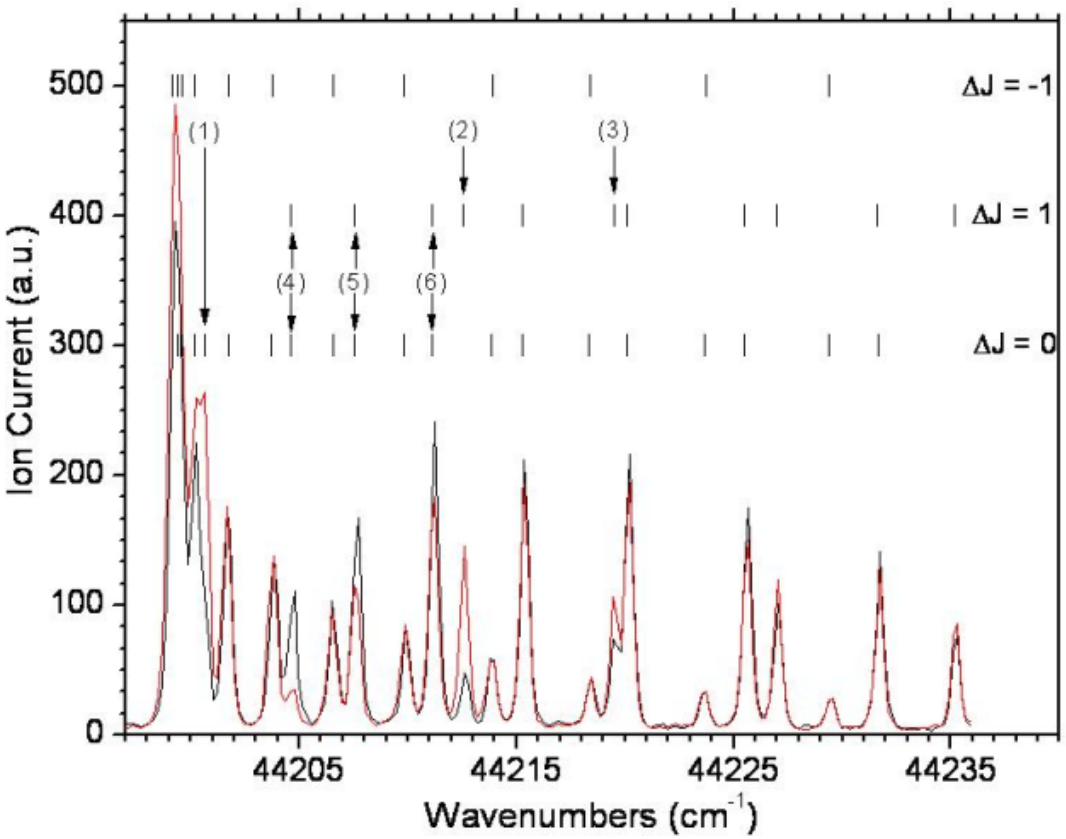

Figure 6.1: Ion count as a function of excitation laser frequency. Comparison of spectroscopy when guide is on (red line) and when guide is off (black line). Transitions (1)-(3) are stronger with the guide voltage on, while transitions (4)-(6) are suppressed. The lines represent allowed transitions calculated using the molecular constants found in Appendix C.

Feature	*Ground State*	*Excited State*
(1)	$\|J = 1/2, f\rangle$	$\|J = 1/2, N = 0\rangle$
(2)	$\|J = 1/2, f\rangle$	$\|J = 3/2, N = 2\rangle$
(3)	$\|J = 3/2, f\rangle$	$\|J = 5/2, N = 3\rangle$
(4)	$\|J = 1/2, e\rangle$	$\|J = 1/2, N = 1\rangle$
	$\|J = 1/2, e\rangle$	$\|J = 3/2, N = 1\rangle$
(5)	$\|J = 3/2, e\rangle$	$\|J = 3/2, N = 2\rangle$
	$\|J = 3/2, e\rangle$	$\|J = 5/2, N = 2\rangle$
(6)	$\|J = 5/2, e\rangle$	$\|J = 5/2, N = 3\rangle$
	$\|J = 5/2, e\rangle$	$\|J = 7/2, N = 3\rangle$

Table 6.1: Tabulation of transitions identified in Figure 6.1. For features (4), (5), and (6), there are two corresponding transitions. Although the transitions are separated by a few hundredths of a wave number, they are not distinguishable in our detection scheme due to the bandwidth of the laser.

state in NO are also shown in Figure 6.1 as lines. These transitions are calculated using the equations and molecular constants found in Appendix C.

There are three features, (1), (2), and (3), where there is more signal when the guide is operating at ± 4.5 kV. These features correspond to transitions from the f-state of the two lowest rotational levels of the ground state. The exact transitions are shown in Table 6.1. This increase in ion signal, or enhancement, is the result of a greater number of low-field seeking molecules that reach the detection region due to guiding. Features (4), (5), and (6) correspond to transitions that originate in the e-state of the three lowest rotational levels of the ground state (Table 6.1). The observed suppression is due to high-field seeking molecules being removed from the molecular beam by the presence of the guide field.

In addition to examining the spectra of NO when the guide is turned on and off, the number of molecules out of the guide as a function of the guide voltage

was also measured. This measurement was taken for transitions corresponding to features (2), (3), and (4). In each measurement, the number of ions collected during approximately 320 laser shots are counted, and ten consecutive measurements are taken for each guide voltage to determine statistical error. The number of ions collected for each guide voltage is also normalized to the number collected at 4.5 kV. This is done because fluctuations in the count rate were small at high voltages since more molecules are guided. Furthermore, repeat measurements are taken on several different days after the laser alignment and input pressure of NO is adjusted. This is done to evaluate the systematic error in the measurement. Figures 6.2 and 6.3 show the number of counts observed as a function of guide voltage for features (2) and (3). Since the initial state of the transition is a low-field seeking state, the measured number out of the guide increases for increasing voltage, consistent with Monte Carlo modeling of the trajectories in the guide. This model is done using the numerical software program SimION[72]. Using this program, the electric field is modeled, and the conducting surfaces of the copper can, the source tube, the guide, and the detection plates are modeled as well. Using the potential energy of the system, which is calculated from the Stark shift (Eq. 3.23), an equivalent electric field for ion propagation is determined. Using SimION with this electric field, Monte Carlo trajectories of ions in this field are calculated. These ion-trajectories then represent neutral particle trajectories. Further details of this model and a detailed analysis of this measurement for feature (2) can be found in reference [53].

The results of the measurement using the transition represented by feature (4) were quite different. Since the initial state of this transition is high-field seeking,

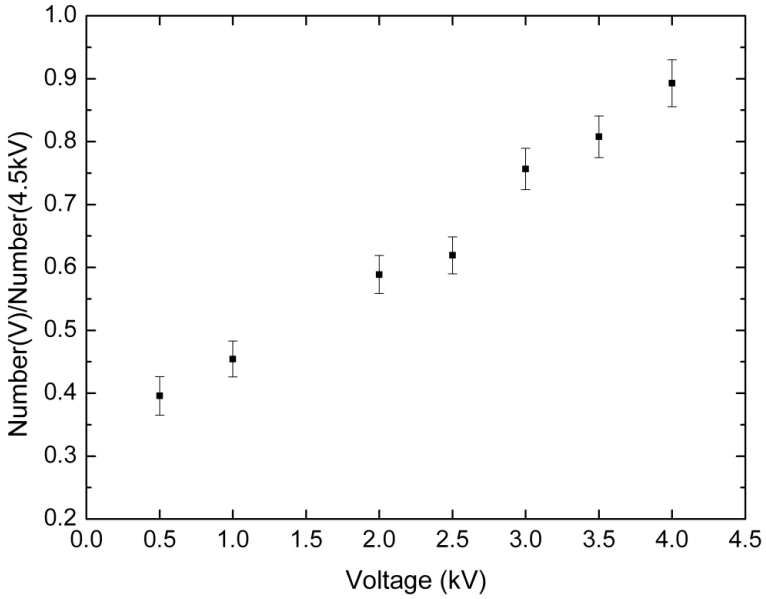

Figure 6.2: Number of molecules out of the guide as a function of guide voltage for $|J = 1/2, f\rangle \rightarrow |J = 3/2, N = 2\rangle$ transition.

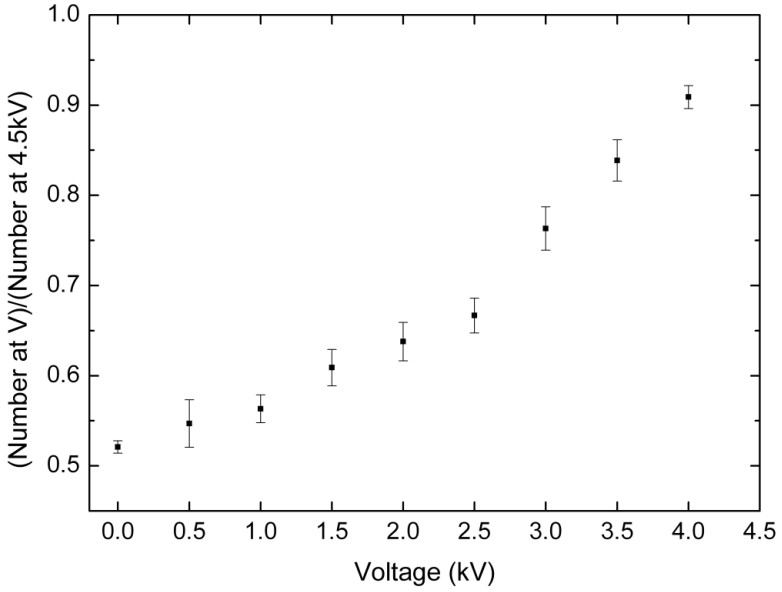

Figure 6.3: Number of molecules out of the guide as a function of guide voltage for $|J = 3/2, f\rangle \rightarrow |J = 5/2, N = 3\rangle$ transition.

we expect a decrease in the output as the guide voltage is increased. At low guide voltages (0-2 kV), the measured flux behaved as expected. For guide voltages greater than 2.0 kV, the measured flux does not follow this trend. One explanation for this effect is that in the presence of an electromagnetic field the Λ-doublet states can couple to one another. Since the output of the guide contains both Λ-doublet states, the laser field from the ionization laser will cause some of the high-field seeking (e-state) molecules to couple to the f-state and some of the low-field seeking (f-state) molecules to couple to the e-state. When the guide voltage is high, there are significantly more low-field seeking states in the output than high-field seeking. Thus, when the laser radiation mixes the states the suppression effect is lost. In this measurement, the effect is seen when there is little time separation between the excitation and ionization laser pulses. Furthermore, since the bandwidth of the laser is large, the Λ-doublet states cannot be resolved. This theory can be tested by increasing the time separation of the laser pulses.

These same measurements were also conducted with the sphere present in the guide. As mentioned in Section 4.2, the purpose of the sphere is to block line-of-sight in the guide. This means that a large majority of the molecules that reach the output of the guide are reflected by the electric field and, are the cold fraction. Figure 6.4 shows the spectroscopy of the output of the guide with the sphere in place. This spectra was taken using the same techniques as described above. From the Figure 6.4, it is apparent that only one transition is enhanced with this guide configuration. The feature corresponds to the transition $|J = 1/2, f\rangle \rightarrow |J = 1/2, N = 0\rangle$. By matching the spectra to known spectroscopy of NO[54], the remainder of the

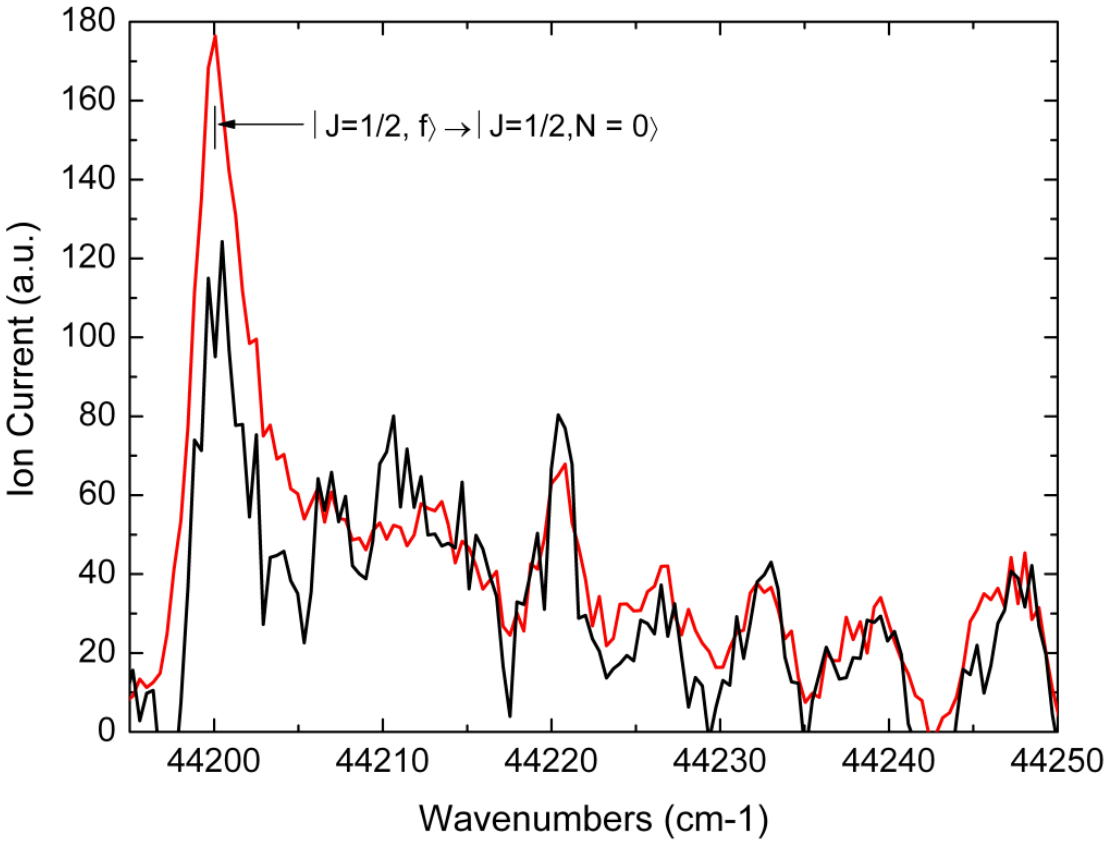

Figure 6.4: Comparison of spectroscopy for the Stark guide with the sphere in place when the guide is on and when the guide is off. The red line represents a guide voltage of ±4.5 kV (on), while the black line represents a guide voltage of 0 kV (off). The two spectra were taken using the same laser and guide schemes as described above. The line represents the calculated value for the allowed transition shown.

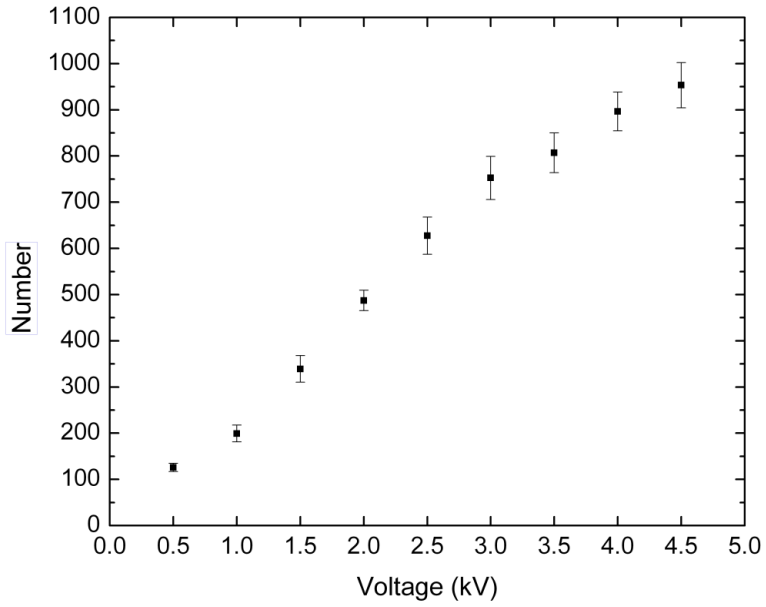

Figure 6.5: Number of molecules out of the guide as a function of guide voltage for $|J = 1/2, f\rangle \rightarrow |J = 1/2, N = 0\rangle$ transition.

transitions were determined to be a result of background NO in the chamber. This is done by comparing the spectroscopy of NO at several different temperatures (10 K, 50 K, 77 K, 150 K, and 300 K) with the experimental spectroscopy.

The strength of the $|J = 1/2, f\rangle \rightarrow |J = 1/2, N = 0\rangle$ transition as a function of guide voltage was also measured. This was done using the same collection technique as before, and the results for this measurement are shown in Figure 6.5. Note that for this measurement, the number of counts for each guide voltage was not normalized to the number of counts at 4.5 kV.

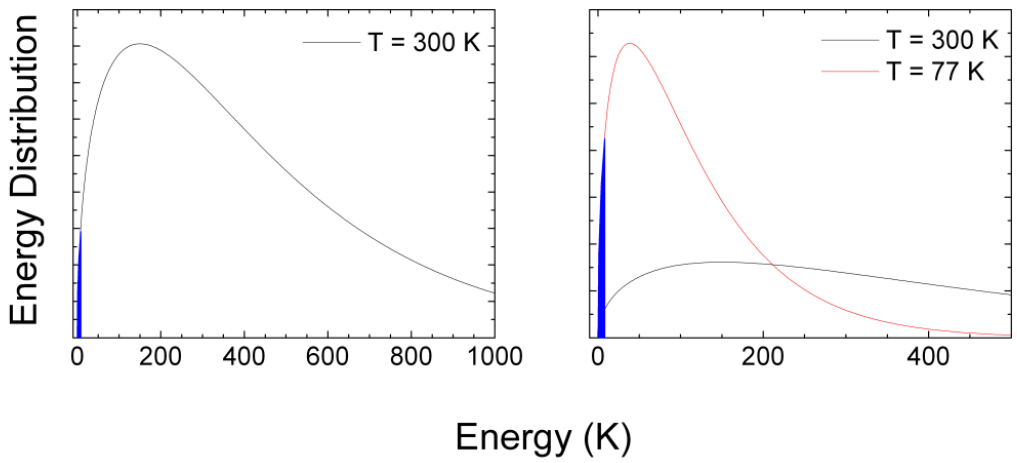

Figure 6.6: (a). A 300 K Maxwell-Boltzmann distribution. The shaded area shows the cold fraction of the distribution. (b). Both a 300 K and 77 K Maxwell-Boltzmann distribution. As the temperature of the distribution is decreased the number of molecules in the cold fraction, at a given temperature, increase.

6.2 Time of Flight Measurements

Many of the methods used to cool molecules start with a hot source ($>$ 100 K) of molecules. The methods then directly cool the molecules. As already discussed, this technique produces cold molecules by extracting the cold fraction from a thermal distribution. This means that even in a room temperature gas, there exist molecules (approximately 10^{15}) that have a temperature of a fraction of a Kelvin. Figure 6.6a. illustrates this for a 300 K distribution. However, if the temperature of the distribution is decreased, then this number will increase. For example, there are seven times more particles with a temperature $<$1K in a 77 K distribution than in a 300 K distribution. This is seen in Figure 6.6b., which shows both a 300 K and a 77 K Maxwell-Boltzmann distribution.

As described in Chapter 4, the apparatus is designed to take advantage of this effect. When the NO passes through the source tube, it is cooled through collisions with the walls of the tube. Recall that the temperature of the tube is controlled by the heater loop connected to the cold clamp, which is attached to the cryo pump. This allows for the temperature of the NO being injected into the guide to be controlled.

To determine the temperature of the source, field stabilized molecular Rydberg time of flight spectroscopy was used to map the spatial distribution of the output. For this measurement, the guide was set to 0 kV due to physical constraints within the system. Before taking the spectroscopy measurements, a Rydberg state transition was identified. This was done by tuning PDL-1 to the $|v'', J = 1/2\rangle \leftarrow |v' = 0, J = 3/2\rangle$ transition and scanning PDL-2 over the wavelength range just below ionization. Once a transition was found, the spatial distributions for several time delays ($\sim 0.3\mu s \leq T_{\text{delay}} \leq \sim 5.0\mu s$) were measured. This is done by counting the number of ions that hit the detector, in a given time range, during 4000 laser shots. Figure 6.7 shows these distributions for an external (temperature controlled) source temperature of 77 K. The progression of the distributions is shown as a function of time delay, T_{delay}. Recall, as shown in Figure 5.1, that T_{delay} corresponds to the amount of time between the laser firing and the field ionizing pulse.

The fit of these distributions to the Monte Carlo simulation is also shown. This fit yields a temperature of 77$\pm$3 K, which is in agreement with the temperature set by the controller. This temperature is determined using the procedure discussed in

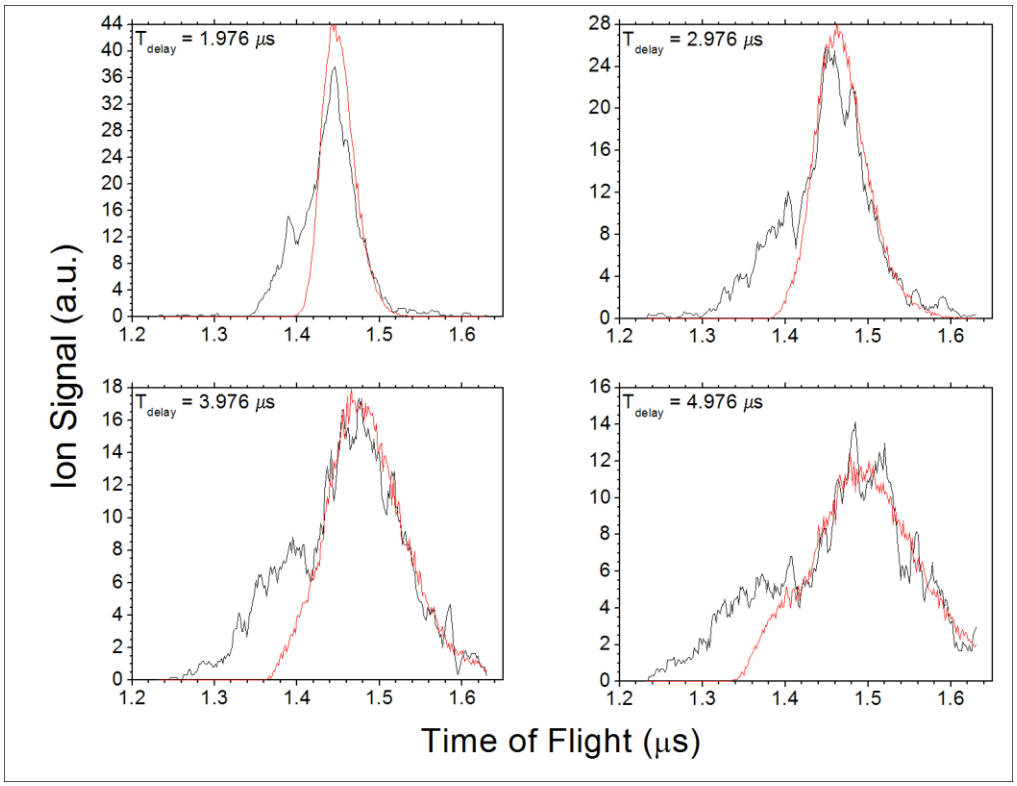

Figure 6.7: Spatial distribution of NO($v = 0, J = 1/2$) as a function of time delay, T_{delay}. The red line shows the Monte Carlo fit, which yields a temperature of 77±3 K. For this experiment T_{delay} ranges from ∼0.3 μs to ∼5.0 μs and the source temperature is 77 K.

Section 5.2. Once the best values for the temperature and stray field are determined, the temperature is decreased and reduced until a noticeable change in the fit occurs. Notice the wing is not included in the fit and is not modeled by the Monte Carlo simulation. This feature is a result of the autoionization of the NO Rydberg states before the field ionization pulse and thus does not contribute to determining the temperature of the source. This was determined by applying a small bias field to the system, which caused the TOF of this feature to change. This response indicates that the molecules represented by this feature are ions before the field ionization pulse. This same measurement was also conducted for a source temperature of 70 K. The resulting fit yielded a temperature of 69.5±3 K, and the plot of this data can be seen in Figure 6.8.

Although repeating these measurements at lower temperatures is desirable, attempts to do so resulted in poor data due to "freeze out" in the source tube. "Freeze out" occurs because the temperatures at which we wish to take measurements are well below the freezing point of NO, so the molecules stick to the tube walls. This will eventually cause the source tube to clog or significantly reduce its output. However, from the measurements above, it is clear that we have created a cold molecular source whose temperature is controllable between 70 K and 80 K. By being able to do this, we increase the number in the cold fraction. Thus, the number of molecules that are guided is also increased, which means a higher number of cold molecules at the output of the guide.

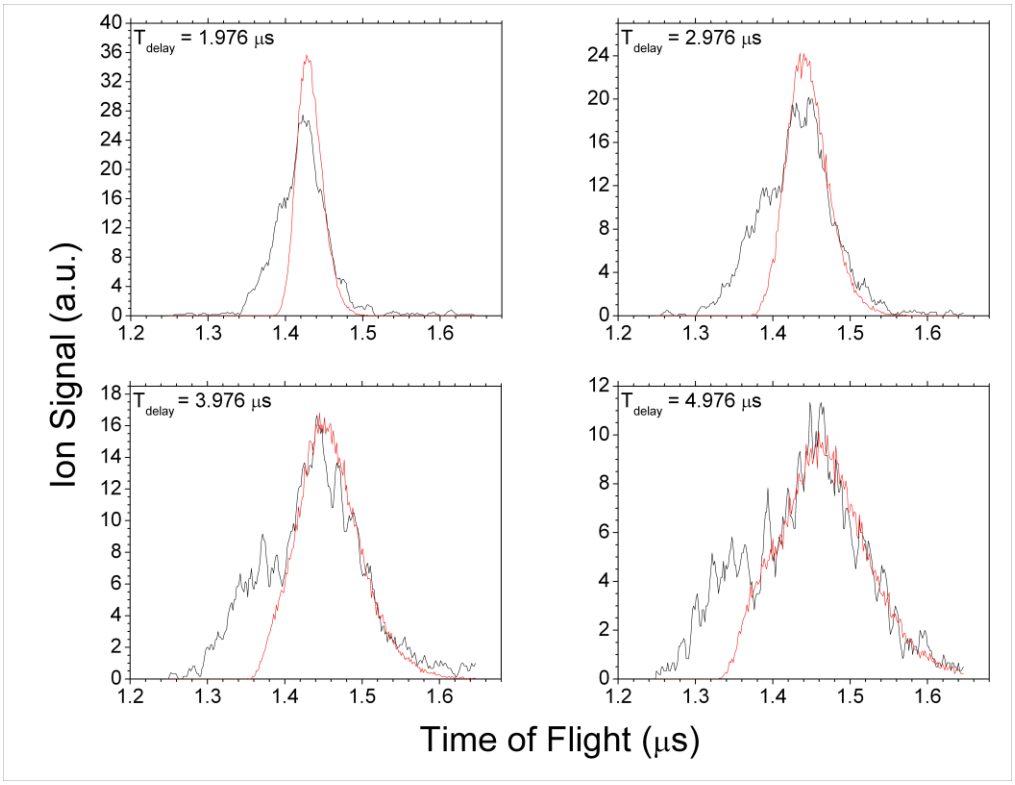

Figure 6.8: Spatial distribution of NO($v = 0, J = 1/2$) as a function of time delay, T_{delay}. The red line shows the Monte Carlo fit, which yields a temperature of 69.5±3 K. The source temperature is 70 K

6.3 Producing Cold NO

The results of these initial experiments show that it is feasible to produce cold NO using a straight Stark guide. However, to isolate these cold molecules from the rest of the distribution, it is necessary to block the line-of-sight in the guide. By doing this, most of the unguided particles that traverse the guide will collide with the sphere and not make it to the output. This is done by placing the sphere in the center of the guide, as described in Section 4.2. By blocking line-of-sight, only the molecules that are moving slow enough to reflect off the electric fields are guided. Thus, a majority of the molecules that reach the output of the guide are slow moving. Furthermore, by decreasing the electric fields, it is possible to control the temperature of the fraction guided.

In this section, I will discuss the results of experiments that illustrate these effects. The experiments are conducted using the transition identified in Section 6.1 $|J = 1/2, f\rangle \rightarrow |J = 1/2, N = 0\rangle$, using the spectra from the guide with the sphere in place. Furthermore, the measurements are taken using the field stabilized molecular Rydberg time of flight technique.

Figure 6.9 shows the spatial distributions out of the guide for several time delays ($\sim 0.7\mu s \leq T_{\text{delay}} \leq \sim 5.5\mu s$). These spatial distributions were collected in the same manner as described in Section 6.2. However, for this specific measurement, the guide voltage is set to 4.5 kV, and the source temperature is set to 77 K. The distributions are smoothed using a 10-point sliding average to reduce noise.

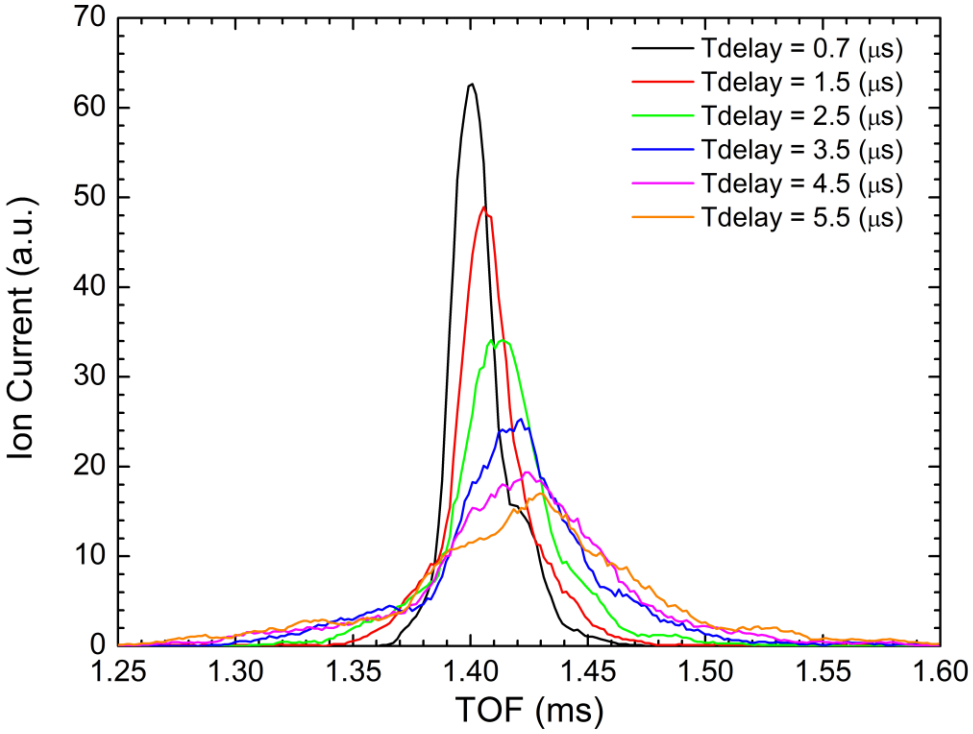

Figure 6.9: Field stabilized molecular Rydberg time of flight data corresponding to several time delays ($\sim 0.7\mu s \leq T_{\text{delay}} \leq \sim 5.5\mu s$). The measurement is conducted using a guide voltage of $\pm$4.5 kV and a source temperature of 77 K. Using the mapping function for this source temperature (see Figure 6.10) and the described analysis, the velocity of the peak (v_{peak}) of the distribution is found to be 105$\pm$2 m/s.

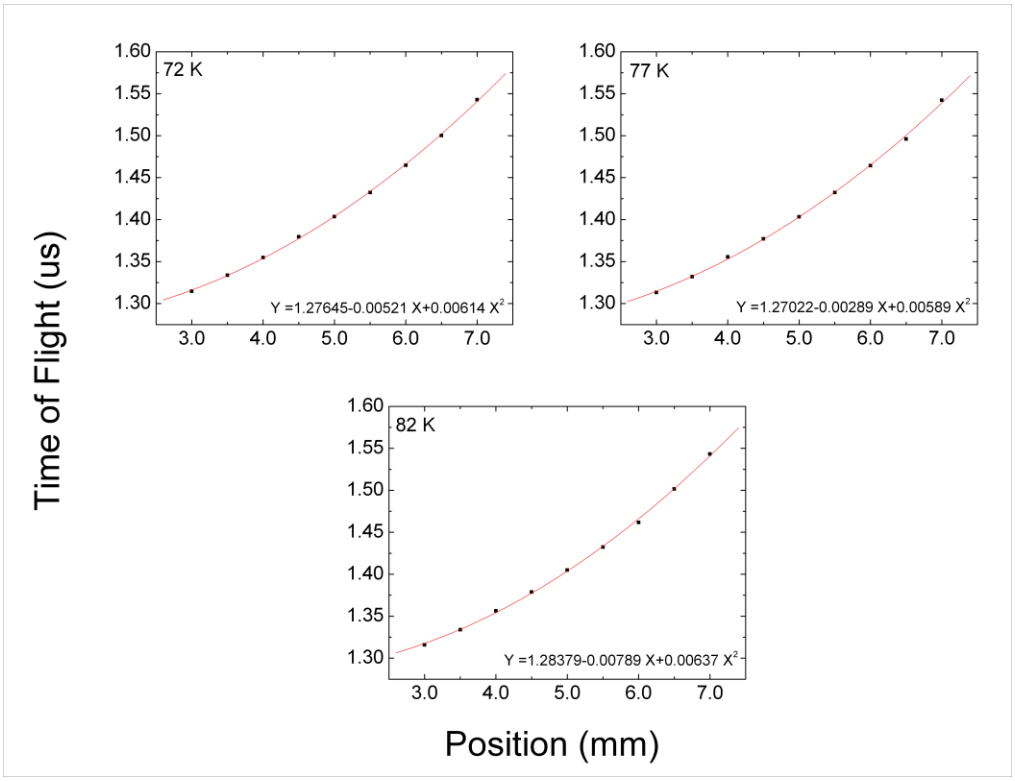

Figure 6.10: Mapping functions for three different source temperatures. The red line is the numerical fit of the mapping data to a quadratic function. The equation, i.e. mapping function, corresponding to the fit is listed. Here x represents the position (in mm) of the laser between the first two plates of the detector and y is the time of flight (in μs).

To determine the velocity of the peak (v_{peak}) of the distribution, we look at the change in the time of flight of the peak of the distribution for different time delays. This is done by measuring the change in time of flight between the peak of the longest time delay and the peak of the other time delays. Using the mapping function described in Section 5.2 and is found in Figure 6.10 the distance the peak moved Δx for a particular time delay difference ΔT_{delay}, is determined from the measured time of flight difference between peaks. The velocity v of the peaks is then found by

$$v = \frac{\Delta x}{\Delta T_{\text{delay}}}. \tag{6.1}$$

Once a velocity is calculated for each ΔT_{delay}, the velocities are averaged and the standard deviation of the mean is determined. Errors quoted are strictly statistical, but there is systematic error on the order of 20%.

Using this technique, v_{peak} of the distribution shown in Figure 6.9 is determined to be 105±2 m/s. Furthermore, similar measurements are conducted for guide voltages of ±4.0 kV, ±3.5 kV, and ±2.5 kV. The spatial distributions from these measurements, as well as the ±4.5 kV, are shown in Figure 6.11. v_{peak} for these distributions is also determined using the analysis outlined above. These velocities are 54±5 m/s, 53±6 m/s, and 67±3 m/s, respectively. Similar measurements are also conducted for source temperatures of 72 K and 82 K. The field stabilized molecular Rydberg time of flight data and the calculated velocities are found in Figures 6.12 and 6.13.

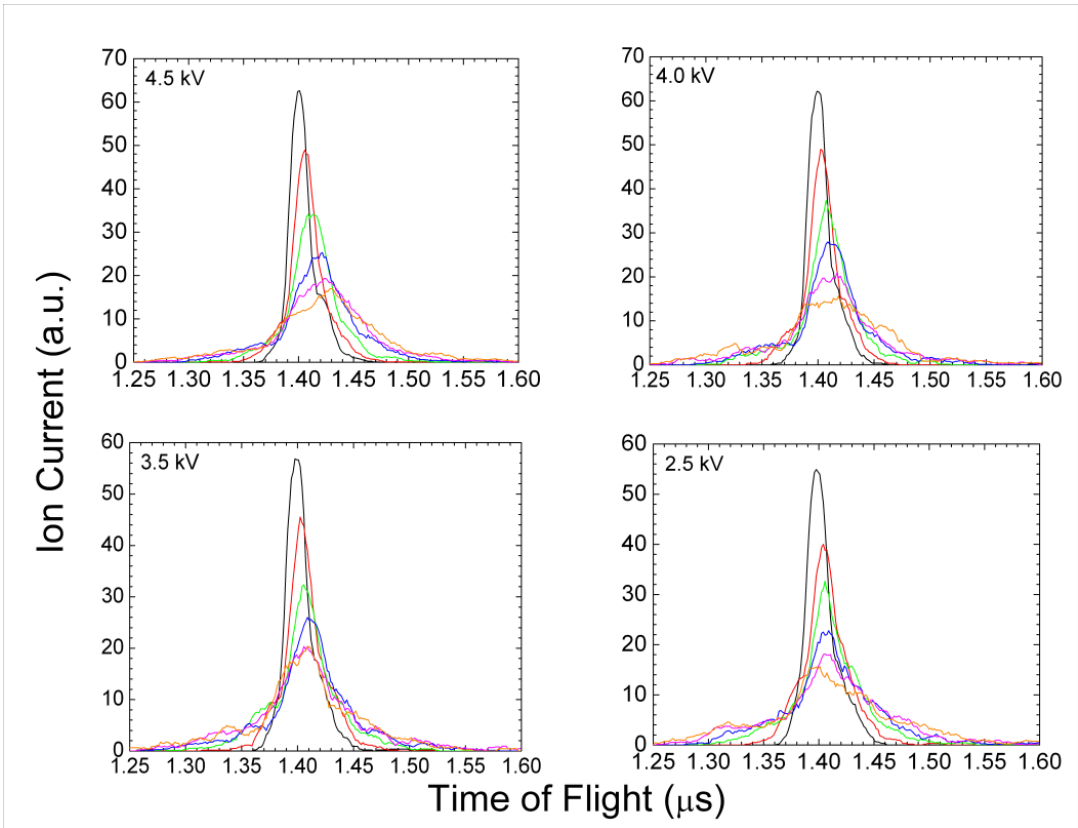

Figure 6.11: Plots of the field stabilized molecular Rydberg time of flight data for guide voltages of ±4.5 kV, ±4.0 kV, ±3.5 kV, and ±2.5 kV and a source temperature of 77 K. The calculated peak velocities (v_{peak}) are 105±2 m/s, 54±5 m/s, 53±6 m/s, and 67±3 m/s, respectively. The time delays used were 0.7μs (black), 1.5μs (red), 2.5μs (green), 3.5μs (blue), 4.5μs (magenta), and 5.5μs (orange).

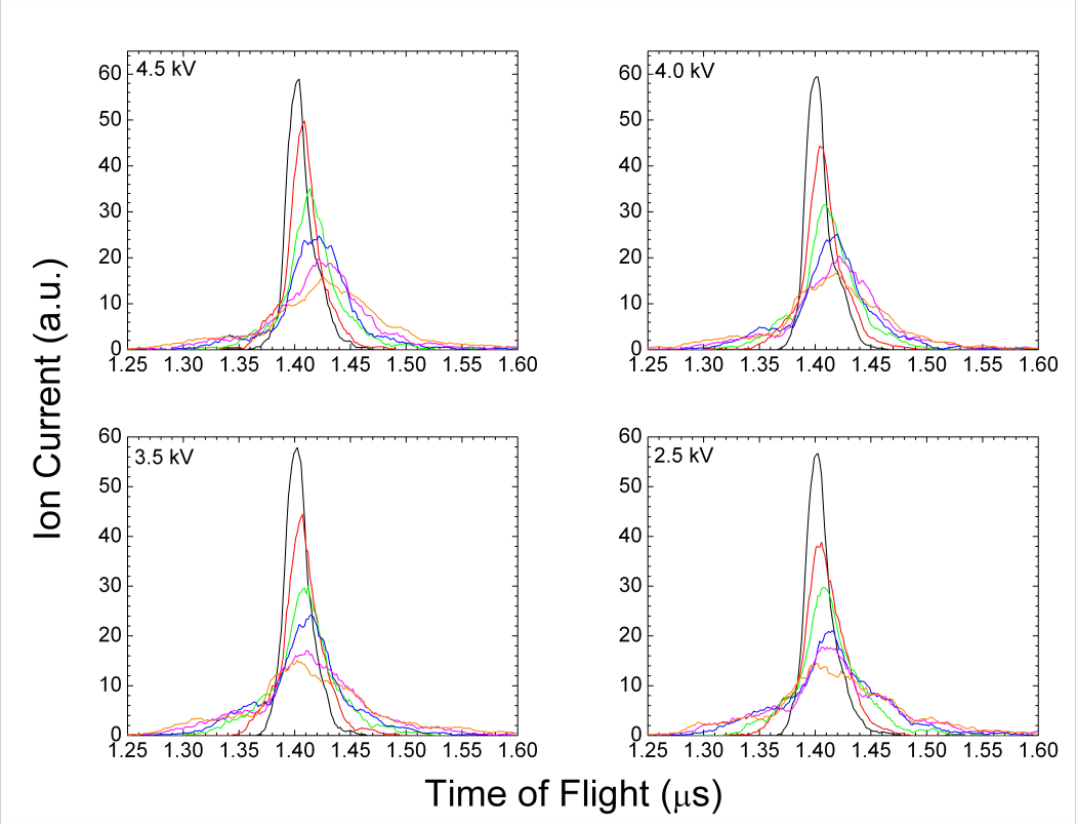

Figure 6.12: Plots of the field stabilized molecular Rydberg time of flight data for guide voltages of ±4.5 kV, ±4.0 kV, ±3.5 kV, and ±2.5 kV for a source temperature of 72 K. The velocities of these distributions are calculated using the 72 K mapping function found in Figure 6.10. The corresponding values of v_{peak} are 105±5 m/s, 59±3 m/s, 46±6 m/s, and 46±2 m/s, respectively. The time delays used were 0.7μs (black), 1.5μs (red), 2.5μs (green), 3.5μs (blue), 4.5μs (magenta), and 5.5μs (orange).

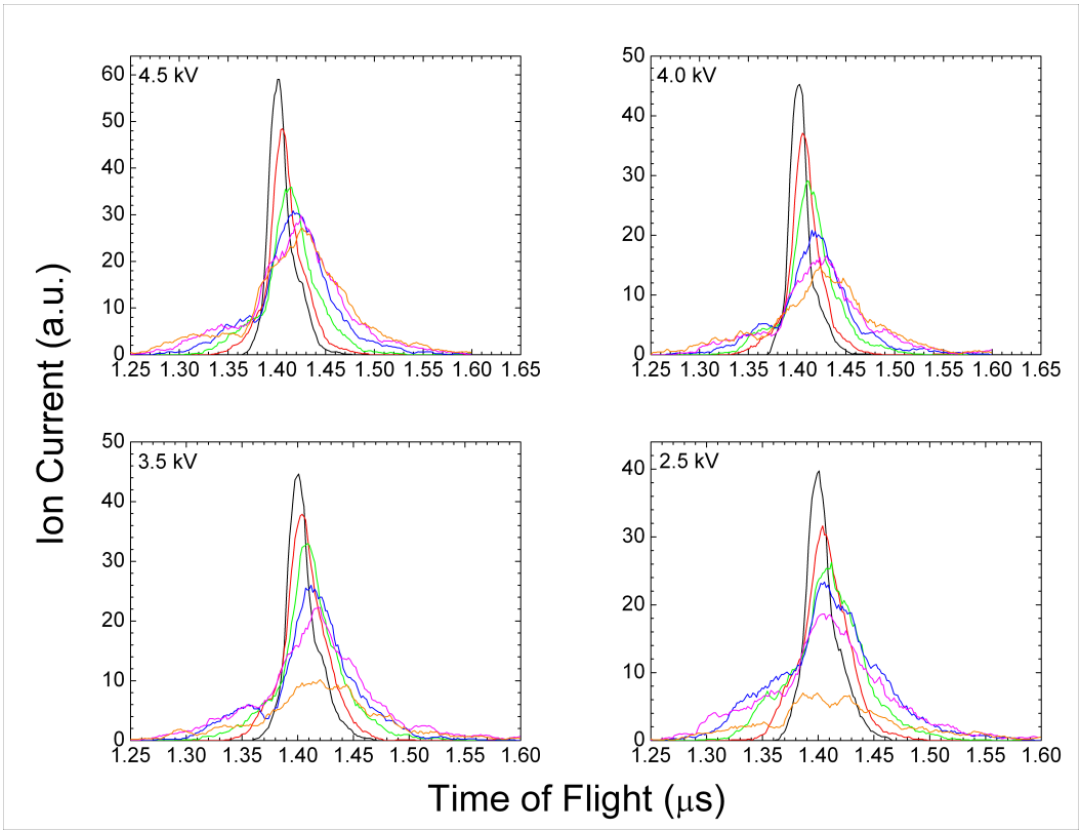

Figure 6.13: Plots of the field stabilized molecular Rydberg time of flight data for guide voltages of ±4.5 kV, ±4.0 kV, ±3.5 kV, and ±2.5 kV for a source temperature of 82 K. The peak velocities for these distributions are calculated using the 82 K mapping function found in Figure 6.10. The velocities are 112±3 m/s, 104±1 m/s, 80±2 m/s, and 66±10 m/s, respectively. The time delays used were 0.7μs (black), 1.5μs (red), 2.5μs (green), 3.5μs (blue), 4.5μs (magenta), and 5.5μs (orange).

In order to determine the temperature of these distributions, the data shown in Figures 6.11, 6.12, and 6.13 was fit using a Monte Carlo simulation similar to the one described in Section 5.2 and used in the previous section. As mentioned before, the output of the hexapole guide can be modeled by a Maxwell-Boltzmann distribution of the form given by Eq. 5.2. In the previous section this is done using a single Maxwell-Boltzmann distribution. However, in order to fit the distributions measured with the sphere in place, two Maxwell-Boltzmann distributions are used. This is necessary since not all of the molecules that reach the output are guided. Meaning that some of the molecules that are detected are not part of the cold fraction and will have a different speed distribution.

To create this simulation the Monte Carlo code discussed in Section 5.2 is modified. This is done by adding a second speed distribution to the existing speed distribution in the code. This new speed distribution has the form

$$f(v) = \alpha v^2((\frac{m}{2\pi k_B T_1})^{3/2} e^{-\frac{mv^2}{2k_B T_1}} + (\frac{m}{2\pi k_B T_2})^{3/2} e^{-\frac{mv^2}{2k_B T_2}}), \tag{6.2}$$

where α is a normalization constant and T_1 and T_2 are the temperatures of the two speed distributions being used. Furthermore, in order to take into account the ions that are present in the measurements, a Gaussian function is fit to the left-hand wing of each time delay. A Gaussian function is chosen because previously measured time of flight data for ions has a Gaussian form.

Using this new Monte Carlo, theoretical spatial distributions are created. This is done by fixing T_2 at the source temperature and using the mapping function

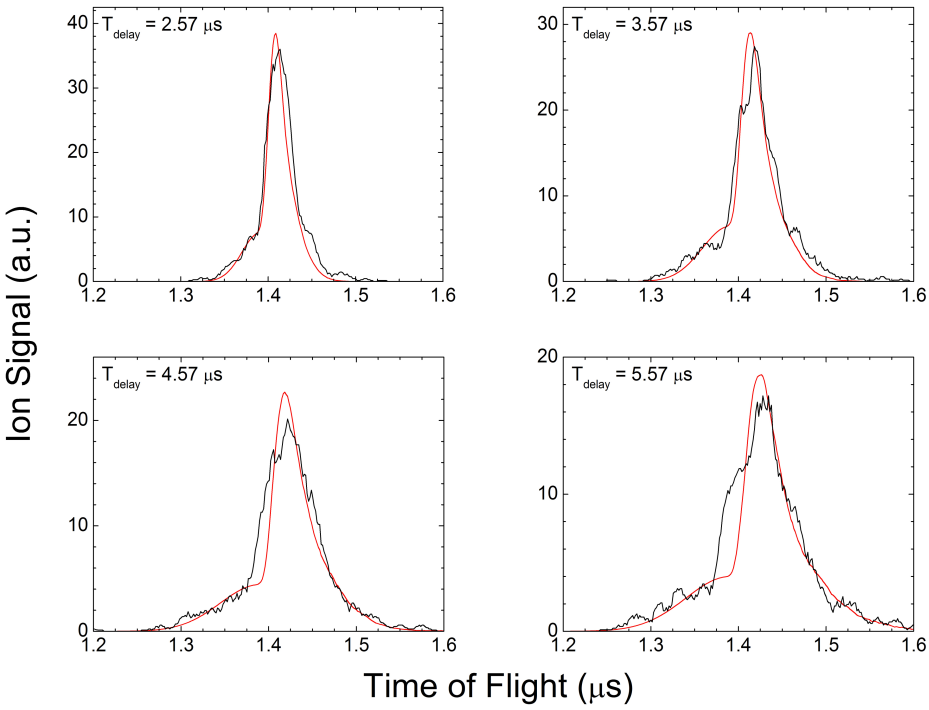

Figure 6.14: Spatial distribution of $|J = 1/2, f\rangle \rightarrow |J = 1/2, N = 0\rangle$ transition as a function of time delay, T_{delay}. The red line shows the Monte Carlo fit, which yields a temperature of 18±2 K. For this experiment T_{delay} ranges from 0.77 μs to 5.57 μs, the source temperature is 77 K, and the guide voltage is ±4.5 kV.

	Guide Voltage			
Source Temp.	*4.5 kV*	*4.0 kV*	*3.5 kV*	*2.5 kV*
72 K	15±2 K	11±2 K	10±2 K	7±2 K
77 K	18±2 K	13±2 K	10±2 K	7±2 K
82 K	20±2 K	17±2 K	14±2 K	11±2 K

Table 6.2: Tabulation of the temperatures of the field stabilized Rydberg time of flight data shown in Figures 6.11, 6.12, and 6.13. These temperatures are calculated for the different guide voltages using the Monte Carlo code described in this section.

corresponding to the source temperature to determine the previously discussed parameters. For example, for the data shown in Figure 6.11, T_2 = 77 K, the field ionization pulse is 495 V, and the position of the laser is 6.65 mm from the front plate. Using these parameters and choosing T_1, theoretical distributions are created. These distributions are then compared by eye to the experimental measurements and T_1 is adjusted until the model and experiment are in agreement. To determine the error in this measurement, T_1 is modified until clearly by eye, the model does not fit the experiment. This fit is illustrated in Figure 6.14 for a source temperature of 77 K and a guide voltage of ±4.5 kV, and for this particular fit yielded a temperature for the distribution of 18±2 K. The simulation is also fit to the spatial distributions of the remaining guide voltages at the 77 K source temperature, as well as the distributions for both the 72 K and 82 K time of flight data. The results of these measurements are found in Table 6.2.

Similar to the experiments in the previous section, conducting these experiments at a lower source temperature is the next logical step. However, due to "freeze out" in the source tube at temperatures lower than 70 K, this is not possible. On the

other hand, the results of the measurements above show that the use of a straight Stark guide with the line-of-sight blocked is an applicable technique for producing cold NO molecules. In addition, the measurements show that the temperature of the cold fraction can be controlled by changing the guide voltage.

Chapter 7

Conclusion

Through careful design and consideration, we have developed and built an apparatus with a temperature controlled source allowing for a greater number of particles in the cold fraction. In addition, we have shown the feasibility of using a straight Stark guide to produce cold NO molecules. Finally, we have shown that by directing this temperature controlled source of NO molecules into the modified Stark guide, a distribution of cold NO molecules is produced with a temperature of 7±2 K. This final result is comparable to the results (see Table 2.1) of the other techniques and thus proves the viability of the technique as a method to produce cold molecules.

Now that I have shown that cold molecules can be produced using this technique, thoughts turn to experiments that can be performed using its output. One future experiment is to further cool the output of the guide. This could be done by combining the technique with Stark slowing (see Section 2.1.2) by adding a Stark decelerator to the end of the guide. This combination could be implemented as the geometry of the Stark guide is very similar to parts of the Stark slowing apparatus[32]. Furthermore,

since the molecules out of the guide are already moving slowly, the Stark decelerator would not need to be of significant length, which greatly reduces its complexity.

Another future experiment involving the use of the output of the Stark guide is the loading of the cold molecules into a trap. An advantage of loading traps using this technique is that the trap could be continuously loaded because there is continuous production of cold molecules by the guide. Possible trap configurations for trapping cold NO are found in reference [73]. These traps, called biased Stark traps, have a non-zero electric field at the center and suppress the non-adiabatic motion of the molecules.

Once cold NO molecules are trapped, numerous experiments could be performed. One experiment is to measure the collisional and inelastic loss rates of NO-NO collisions. These measurements could be used to determine the strength of the dipole-dipole interaction for NO. Another possibility is sympathetically cooling the NO using laser cooled Rb. This would be done by laser cooling Rb directly on top of the trapped NO and would further cool the NO molecules via collisions with the ultracold Rb. This is desirable because colder the molecules mean increased interaction times and better statistics. These molecules could then be used to create molecular BECs or Fermi degenerate gases and improve precision statistics. Sympathetic cooling would also allow for the investigation of Rb-NO collisions. This could be done by measuring the collisional loss rates in the system.

There are also a number of experiments that could be performed with other polar molecules. These include precision spectroscopy, which would allow for molecules to be investigated at greater detail and lead to new insight about their internal

structure. Also, cold polar molecules could be used to improve the measurement of the electric dipole moment (EDM) of the electron.

Currently there are several techniques being used to produce cold molecules, many of which are listed in Table 2.1. These techniques may also be used to perform the experiments outlined in this section. However, some may be preferable to others. However, many of these techniques employ complicated timing, optical, and apparatus setups and they can be quite costly. Here I have demonstrated a new technique that is simple to implement, moderate in cost, and applicable to many different atoms and molecules, such as OH and NH_3. This ability to inexpensively and efficiently produce a continuous source of cold polar atoms and molecules not only opens up the field of cold physics to many more researchers, but it is a step towards introducing a wide group of atoms and molecules to the ultracold regime.

Bibliography

[1] A. Griffin, S. Stringari, and D. W. Snoke. *Bose-Einstein Condensation*. Cambridge University Press, London, 1994.

[2] E. A. Cornell and C. E. Wieman. Nobel Lecture: Bose-Einstein condensation in a dilute gas, the first 70 years and some recent experiments. *Rev. Mod. Phys.*, 74:875, 2002.

[3] W. Ketterle. Nobel Lecture: When atoms behave as waves: Bose-Einstein condensation and the atom laser. *Reviews of Modern Physics*, 74:1131, 2002.

[4] B. D. Marco and D. Jin. Onset of Fermi degeneracy in a trapped atomic gas. *Science*, 285:1703, 1999.

[5] M. O. Mewes, M. R. Andrews, D. M. Kurn, D. S. Durfee, C. G. Townsend, and W. Ketterle. Output coupler for Bose-Einstein condensed atoms. *Phys. Rev. Lett.*, 78:582, 1996.

[6] S. Bize, P. Laurent, M. Abgrall, H. Marion, I. Maksimovic, L. Cacciapuoti, J. Grünert, C. Vian, F. Pereira dos Santos, P. Rosenbusch, P. Lemonde, G. Santarelli, P. Wolf, A. Clairon, A. Luiten, M. Tobar, and C. Salomon. Cold atom clocks and applications. *J. of Phys. B: Atomic, Molecular and Optical Physics*, 38:S449, 2005.

[7] M. Kasevich and S. Chu. Atomic interferometry using stimulated raman transitions. *Phys. Rev. Lett.*, 67:181, 1991.

[8] D. K. Coles, W. E. Good, J. K. Bragg, and A. H. Sharbaugh. The Stark effect of the ammonia inversion spectrum. *Phys. Rev.*, 82:877, 1951.

[9] J. S. Muenter. Electric dipole moment of carbon monoxide. *J. Mol. Spec.*, 54:490, 1975.

[10] W. L. Meerts and A. Dymanus. Electric dipole moment of OH and OD by molecular beam electric resonance. *Chem. Phys. Lett.*, 23:45, 1973.

[11] I. F. Silvera and J. T. M. Walraven. Stabilization of atomic hydrogen at low temperature. *Phys. Rev. Lett.*, 44:164, 1980.

[12] W.D. Phillips. Nobel Lecture: Laser cooling and trapping of neutral atoms. *Rev. Mod. Phys.*, 70:721, 1998.

[13] S. Chu. Nobel Lecture: The manipulation of neutral particles. *Rev. Mod. Phys.*, 70:685, 1998.

[14] C.N. Cohen-Tannoudji. Nobel Lecture: Manipulating atoms with photons. *Rev. Mod. Phys.*, 70:707, 1998.

[15] Alan L. Migdall, John V. Prodan, William D. Phillips, Thomas H. Bergeman, and Harold J. Metcalf. First observation of magnetically trapped neutral atoms. *Phys. Rev. Lett.*, 54(24):2596, Jun 1985.

[16] H.F. Hess. Evaporative cooling of magnetically trapped and compressed spin-polarized hydrogen. *Phys. Rev. B*, 34:3476, 1986.

[17] H.F. Hess, N. Masuhara, G.P. Kochanski, J.M. Doyle, D. Kleppner, and T.J. Greytak. Magnetic trapping of spin-polarized atomic hydrogen. *Phys. Rev. Lett.*, 59:672, 1987.

[18] B. Ghaffari, J. M. Gerton, W. I. McAlexander, K. E. Strecker, D. M. Homan, and R.G. Hulet. Laser-free slow atom source. *Phys. Rev. A*, 60:3878, 1999.

[19] E. Nikitin, E. Dashevskaya, J. Alnis, M. Auzinsh, E. R. I. Abraham, Furneaux, M. Keil, C. Mcraven, N. E. Shafer-Ray, and R. Waskowsky. Prediction and measurement of the speed-dependent throughput of an octupole filter including non-adiabatic effects: Application to Cs, Li, Rb, and S_2. *Phys. Rev. A*, 67:045401, 2003.

[20] R. deCarvalho, J.M. Doyle, B. Friedrich, J. Guillet, J. Kim, D. Patterson, and J.D. Weinstein. Buffer-gas loaded magnetic traps for atoms and molecules: A primer. *Eur. Phys. J. D*, 7:289, 1999.

[21] 2004. See the special issue on cold molecules:.

[22] H.L. Bethlem, F.M.H. Crompvoets, R.T. Jongma, S. Y. T. van de Meerakker, and G. Meijer. Deceleration and trapping of ammonia using time-varying electric fields. *Phys. Rev. A*, 65:053416, 2002.

[23] B. Friedrich, R deCarvalho, T. Guillet, J.D. Weinstein, and J.M. Doyle. Magnetic trapping of calcium monohydride molecules at milliKelvin temperatures. *Nature*, 395:148–150, 1998.

[24] M. Gupta and D. Herschbach. Slowing and speeding molecular beams by a means of a rapidly rotating source. *J. Phys. Chem.*, 105:1626, 2001.

[25] M.S. Elioff, J.J. Valentini, and D.W. Chandler. Formation of NO($j' = 7.5$) molecules with sub-Kelvin translational energy via molecular beam collisions with argon using the technique of molecular cooling by inelastic collisional energy-transfer. *Eur. Phys. J. D.*, 31:385, 2004.

[26] S. A. Rangwala, T. Junglen, T. Rieger, P. W. H. Pinkse, and G. Rempe. A continuous source of translationally cold dipolar molecules. *Phys. Rev. A*, 67:043406, 2003.

[27] B. Bichsel, J. Alexander, N. Shafer-Ray, M. Morrison, and E. Abraham. Cold molecular NO from a Stark guide. *Bul. Am. Phys. Soc.*, 50:98, 2005.

[28] A. Kerman, J. Sage, S. Sainis, T. Bergeman, and D. DeMille. Production and state-selective detection of ultracold, ground state RbCs molecules. *Phys. Rev. Lett.*, 92:153001, 2004.

[29] C. Stan, M. Zwierlein, C. Schnuck, S. Raupach, and W. Ketterle. Observation of heteronuclear Feshbach resonances in a Bose-Fermi mixture. *Phys. Rev. Lett.*, 93:183201, 2004.

[30] D. Egorov, T. Lahaye, W. Schollkopf, B. Friedrich, and J.M. Doyle. Buffer-gas cooling of atomic and molecular beams. *Phys. Rev. A*, 66:043401, 2002.

[31] M. Humon, S.C. Doret, C. Hancox, L. Luo, and J. Doyle. Magnetic trapping of rare earths at milliKelvin temperatures: Pr, Nd, Tb, Dy, Ho, Er, and Tm. *Bul. Am. Phys. Soc.*, 50:112, 2005.

[32] H.L. Bethlem, G. Berden, and G. Meijer. Decelerating neutral dipolar molecules. *Phys. Rev. Lett.*, 83:1558–1561, 1999.

[33] J.R. Bochinski, E.R. Hudson, H.J. Lewandowski, G. Meijer, and J. Ye. Phase space manipulation of cold free radical OH molecules. *Phys. Rev. Lett.*, 91:243001, 2003.

[34] M.R. Tarbutt, H.L. Bethlem, J.J. Hudson, V.L. Ryabov, V.A. Ryzhov, B.E. Sauer, G. Meijer, and E.A. Hinds. Slowing heavy, ground-state molecules using an alternating gradient decelerator. *Phys. Rev. Lett.*, 92:173002, 2004.

[35] D. Egorov, B. Friedrich, D. Patterson, J.D. Weinstein, and J.M. Doyle. Spectroscopy of laser-ablated buffer-gas-cooled PbO at 4 K and the prospects for measuring the electric dipole moment of the electron. *Phys. Rev. A*, 63:030501, 2001.

[36] R.V. Krems, D. Egorov, J.S. Helton, K. Maussang, S.V. Nguyen, and J.M. Doyle. Zeeman effect in CaF. *J. Chem. Phys.*, 121:11639, 2004.

[37] M. Gupta and D. Herschbach. A mechanical means to produce intense beams of slow molecules. *J. Phys. Chem.*, 103:10670, 1999.

[38] E. Abraham, B. Bichsel, and N. Shafer-Ray. Sources and studies of cold molecular NO. *Bul. Am. Phys. Soc.*, 48:128, 2003.

[39] B. J. Bichsel, M. A. Morrison, N. Shafer-Ray, and E. R. I. Abraham. A cold source of nitric oxide. In preparation, 2005.

[40] D. DeMille, F. Bay, S. Bickman, D. Kawall, D. Krause, S. E. Maxwell, and L. R. Hunter. Investigation of PbO as a system for measuring the electric dipole moment of the electron. *Phys. Rev. A*, 61:052507, 2000.

[41] B.E. Sauer, P.C. Condylis, J.J. Hudson, M.R. Tarbutt, and E.A. Hinds. Improved measurement of the electron electric dipole moment using YbF. *Bul. Am. Phys. Soc.*, 50:60, 2005.

[42] E. Commins, S. B. Ross, and D. DeMille. Improved experimental limit on the electric dipole moment of the electron. *Phys. Rev. A*, 50:2960, 1994.

[43] E.M. Henley and J.P. Schiffer. *More Things in Heaven and Earth.* Springer, New York, 1999.

[44] Landau and Lifshitz. *Quantum Mechanics Non-Relativistic Theory: Volume 3.* Elsevier Science & Technology Book, New York, 1997.

[45] B. H. Bransden and C. J. Joachain. *Physics of Atoms and Molecules.* Addison Wesley, England, 1996.

[46] C. H. Townes and A. L. Schawlow. *Microwave Spectroscopy.* McGraw-Hill Book Company, Inc., New York, 1955.

[47] G. Herzberg. *Molecular Spectra and Molecular Structure I: Spectra of Diatomic Molecules.* Van Nostrand, New York, 2nd edition, 1950.

[48] This is the reduced mass of the two nuclei.

[49] M. A. Morrison. Data for NO spectroscopy studies. Collaboration notes dealing with NO experiments., May 2005.

[50] J. D. Graybeal. *Molecular Spectroscopy.* McGraw-Hill Book Company, Inc., New York, 1988.

[51] C. A. Burrus and J. D. Graybeal. Stark effect at 2.0 and 1.2 millimeters wavelength: Nitric oxide. *Phys. Rev.*, 109:1553, 1958.

[52] A. R. Hoy, J. W. C. Johns, and A. R. W. McKeller. *Can. J. Phys.*, 53:2029, 1975.

[53] B. J. Bichsel, M. A. Morrison, N. Shafer-Ray, and E. R. I. Abraham. Experimental and theoretical investigation of the Stark effect for trapping cold molecules: application to nitric oxide. In preparation, 2005.

[54] J. Luque and D. R. Crosley. LIFBASE: Database and Spectral Simulation Program (Version 2.0). SRI International Report MP 99-009, 1999.

[55] Y. Liu, Y. Guo, Lin. J., G. Huang, C. Duan, and F. Li. Measurement of the electric dipole moment of NO ($X^2\Pi$ v=0,1) by mid-infrared laser magnetic resonance spectroscopy. *Mol. Phys.*, 99:1457, 2001.

[56] C. A. Burrus and C. M. Graybeal. One-to-two millimeter wave spectroscopy.III. NO and DI. *Phys. Rev.*, 109:1553, 1958.

[57] R. M. Neumann. High-precision radiofrequency spectrum of $^{14}N^{16}O$. *Astrophy J.*, 161:779, 1970.

[58] http://www.aip.org/avsguide/refguide/vapor.html.

[59] S. Stolte, J. Reuss, and H. L. Schwartz. Orientation anisotropy in the total collision cross section of state-selected NO on CCl_4 using crossed molecular beams. *Physica*, 57:254, 1971.

[60] S. Stolte and D. van den Ende. The influence of the orientaion of the NO molecule upon the chemiluminescent reaction $NO + O_3 \rightarrow NO_2 + O_2{}^*$. *Chem. Phys.*, 89:121, 1984.

[61] L. Schneider, W. Meier, K. H. Welge, M. N. R. Ashfold, and C. M. Western. Photodissociation dynamics of H_2S at 121.6 nm and a determination of the potential energy function of $SH(A^2\Sigma^+)$. *J. Chem. Phys.*, 92:7027, 1990.

[62] M. N. R. Ashfold, I. R. Lambert, D. H. Mordaunt, G. P. Morley, and C. M. Wester. Photofragment translational spectroscopy. *J. Phys. Chem.*, 96:2938, 1992.

[63] S. R. Procter, Y. Yamakita, F. Merkt, and T. P. Softley. Controlling the motion of hydrogen molecules. *Chem. Phys. Lett.*, 374:667, 2003.

[64] H. Xu, N.E. Shafer-Ray, F. Merkt, D.J. Hughes, M. Springer, R. Tuckett, and R.N. Zare. Measurements of the state-specific differential cross section for the $H+D_2 \leftarrow HD(v' = 4, J' = 3)+D$ reaction at a collision energy of 2.2 eV. *J. Chem. Phys.*, 103:5157, 1995.

[65] M. Karplus and R. N. Porter. *Atoms & Molecules.* Benjamin/Cummings Publishing Co., California, 1970.

[66] G. Reiser, W. Habernicht, K. Müller-Dethlefs, and E. W. Schlag. The ionization energy of nitric oxide. *Chem. Phys. Lett.*, 152:119, 1988.

[67] W. A. Chupka. Factors affecting lifetimes and resolution of Rydberg states observed in zero-electron-kinetic-energy spectroscopy. *J. Chem. Phys.*, 98:4520, 1993.

[68] E. Miescher. High resolution absorbtion spectrum of nitric oxide (NO) in the region of the first ionization limit. *Can. J. Phys.*, 54:2074, 1976.

[69] A. Held, L. Y. Baranov, H. L. Selze, and E. W. Schlag. Lifetime control in Rydberg states using fast switching DC electric fields. ii. enhancement for nitric oxide. *Chem. Phys. Lett.*, 291:318, 1998.

[70] W. C. Wiley and I. H. McLaren. Time-of-flight mass spectrometer with improved resolution. *Rev. Sci. Inst.*, 26:1150, 1955.

[71] N. F. Ramsey. *Molecular Beams*. Oxford at the Clarendon Press, Great Britain, 1956.

[72] SimION 3D$^{\mathrm{TM}}$ Ion and Electron Optics Simulator (Version 7.0). Numerical computer software package.

[73] N.E. Shafer-Ray, K.A. Milton, B.R. Furneaux, E.R.I. Abraham, and G.R. Kalbfleisch. Design of a biased stark trap of molecules that move adiabatically in an electric field. *Phys. Rev. A*, 67:045401, 2003.

[74] S. Svanberg. *Atomic and Molecular Spectroscopy: Basic Aspects and Practical Applications*. Springer, Berlin, 3rd edition, 2001.

[75] Quanta-Ray PDL literature.

Appendix A

Supplying NO to the Experiment

As mentioned in Chapter 4, a manifold is used to supply the experiment with NO. The main purpose of the manifold is to control the flow of NO into the source tube. The manifold is also used to put nitrogen gas into the system when breaking vacuum. This is done to quicken the vacuum breaking process and to maintain an over-pressure in the chamber. In this appendix, I will discuss the elements of the manifold and its construction. The procedure to introduce NO into the manifold, and the chamber, is also discussed.

A.1 Construction

Figure A.1 illustrates the construction of the manifold used to introduce NO gas into the experiment. Most of the manifold is located in a fume hood because of the toxicity of nitric oxide. The only elements that are outside of the fume hood are the components connected between valve 8 and the source chamber. The mechanical

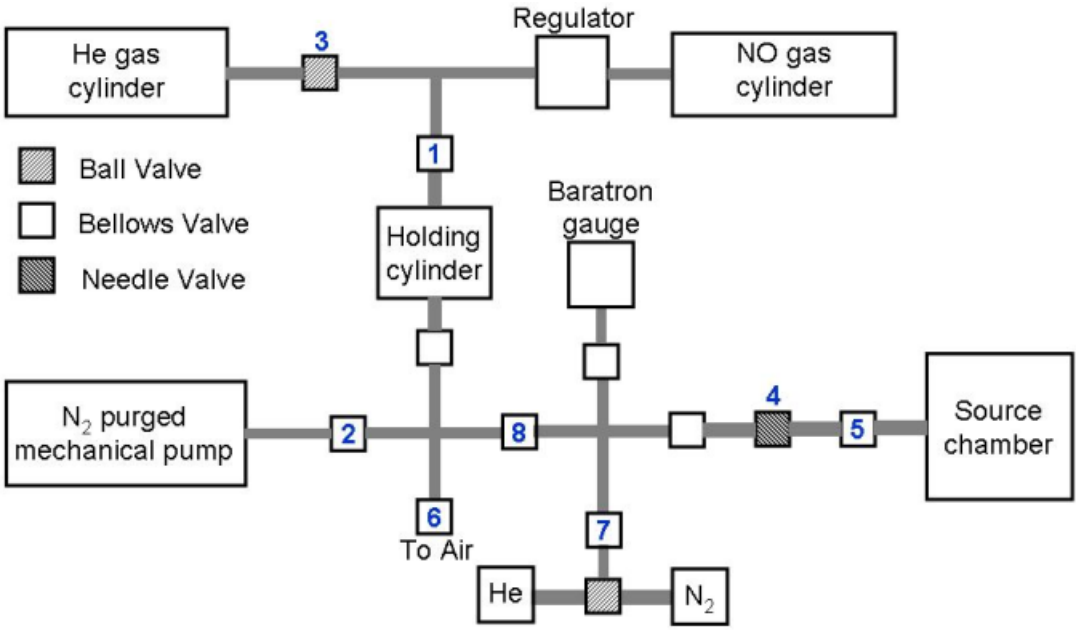

Figure A.1: The manifold used to introduce NO into the experiment. The needle and bellows valves in the current design are constructed from stainless steel and use VCR fittings. The ball valves are brass and use Swage fittings. The tubing used in the manifold is 1/4 inch PTFE, semi-opaque Teflon tubing.

pump is located next to the fume hood so that its exhaust can be directed into the fume hood.

The manifold is constructed from several different components. The NO cylinder and regulator provide a controlled means of allowing NO into the manifold. This regulator is stainless steel and is rated for toxic, corrosive gasses such as NO. The helium cylinder is used for cleaning the NO out of the manifold. This is done to prevent corroding of the other elements by the nitric oxide if it is left in the manifold too long. The procedure to remove the NO is outlined in the section below.

There are three valves used in the design of the manifold shown in Figure A.1. These are ball valves, bellows valves, and a needle valve. The ball valves are used to control the flow of helium or nitrogen gas into the manifold. These valves are made from brass and are connected to the manifold using Swage fittings and 1/4" PTFE tubing. The needle valve and bellows valves are constructed from stainless steel and connect to the manifold using VCR fittings. The bellows valves are used to control which areas of the manifold are accessible by the NO. The needle valve is used to control the flow of NO into the source chamber.

The final component of the manifold is the Baratron gauge. This gauge measures the pressure of NO gas in the manifold. When NO is being let into the source chamber, the gauge is used to monitor the amount of NO entering the chamber.

A.2 Operation

The following procedures outline the necessary steps to let in and remove NO from the manifold. Refer to Figure A.1 for valve numbering.

Letting NO into the source chamber

1. Check to make sure only valves **3**, **5**, **6**, and **7** are closed.
2. Check that reading on Baratron gauge is at minimum.
3. Close valves **2** and **4**.
4. Let small amount of NO into the regulator. Make sure NO cylinder is closed afterwards.
5. Slowly open regulator until pressure on Baratron gauge reads between 50 and 60 units. Close regulator.
6. Close valve **1**.

NO is now ready to be let into the source chamber. After turning on appropriate electronic systems, follow these steps to put NO into the source tube.

1. Open valve **5** and wait for ion gauge pressure on source chamber to stabilize.
2. Open valve **4** one full turn.

Removing NO from the manifold

1. Close valve **5**, and open valves **1** and **4** completely.
2. Open valve **3** until Baratron gauge reads over 800 units; then close valve **3**.

3. Open valve **2** until gauge reads below 10 units.

4. Repeat steps 2 and 3 two to three more times.

5. Leave all valves completely open except valves **3**, **5**, **6**, and **7**, which should be closed.

Appendix B

Dye Lasers

As in many atomic and molecular experiments, lasers play an important role in the experiments described in this work. Here they are used for excitation and ionization of NO molecules so that the molecules can be detected. As described in Chapter 4, the laser system used in these experiments involves two dye lasers that are pumped by a 10 Hz Nd:YAG laser at 532 nm. Thus, the output of the dye lasers is also pulsed. In this appendix, I will discuss the laser action that occurs in dye lasers, as well as the general operation. The optical setup of the dye lasers and the dyes used for these experiments are also discussed.

B.1 Operation

Laser action in organic dyes was discovered in 1966. Since then, laser action has been shown to occur, in some fashion, in several hundred dyes. In order to create laser action, the dye is first dissolved into a liquid, often methanol or ethylene glycol. The dye is then pumped continuously through a region where another light source

has access to the dye. The most common ways of doing this are using cuvettes to contain the dye or using dye jets which produce a high pressure, narrow stream of dye. In both cases a second laser, or pumping laser, is used to excite transitions in the dye.

Figure B.1 shows the general energy-level structure of an organic dye. The transitions that are necessary for laser action occur between two lower electronic singlet states. Both states are split into a continuous structure of energy levels. This is due to the interaction of the dye with the solvent. By applying light to the dye via the pumping laser, molecules are excited from the sublevels of the ground state to the sublevels of the excited state. The molecules then relax very quickly ($\sim 10^{-12}$s) to the lowest level of the excited state. These transitions are radiationless, meaning no photons are emitted. The molecules then return to the sublevels of the ground state with a lifetime of $\sim 10^{-9}$s, emitting fluorescent light (photons) in the process.

As shown in Figure B.1, there is another intermediate step in the laser process. Before the molecules reach the ground state, they first move to a triplet state through another radiationless process. The molecules then decay to the sublevels of the ground state through spontaneous emission. The photons given off in this process make up the laser action in dye lasers.

In order to achieve laser action, the dye must be pumped sufficiently enough that a population inversion occurs between the lowest sublevel of the excited singlet state and the sublevels of the ground state. Once this is accomplished, then amplification of stimulated emission can be achieved. This is done by placing the dye cell in a laser

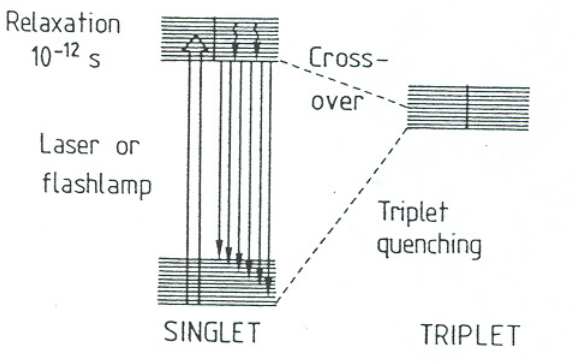

Figure B.1: General energy-level structure of an organic dye molecule[74].

cavity with sufficient pumping power. The laser cavity length is often controlled by an adjustable mirror or diffraction grating. This cavity length determines both the wavelength and bandwidth of the light. Once a significant amount of spontaneous emission is present in the cavity, it will cause stimulated emission within the dye increasing the output at that particular wavelength. The output of this cavity is then directed through beam shaping optics and then into another dye cell called the amplifier. In this cell, the dye is again pumped by the same laser that pumps first cell, or oscillator. Similarly, the molecules are excited to the upper state and then decay to the triplet state. The incoming laser from the oscillator then causes stimulated emission in the dye, amplifying the output. This amplified beam can then be used for a variety of scientific and medical applications.

B.2 Optical setup and laser dye

The two dye lasers used in the laser system described in Chapter 4 have different internal optical configurations. PDL-1 uses a longitudinal pumping scheme, which

means that the Nd:YAG pumping laser passes through the amplifier anti-parallel to the laser beam from the oscillator. This configuration is used with many dyes, including both LDS 698 and DCM dyes used here. However, PDL-2 is configured for side-pumping. In this setup, the pumping laser pumps the amplifier perpendicular to the laser beam from the oscillator. The reason that this configuration is used is to maximize power and to avoid burns on the faces of the cuvette.

The dye curves for LDS 698 and DCM can be found in Figures B.2 and B.3, respectively. These dyes are chosen because the centers of the curves are near wavelengths that can be used to perform the described experiments. The wavelengths are 678 nm and 650 nm. The LDS 698 dye is mixed with methanol at the concentrations suggested in Figure B.2. With DCM, this is not the case. The oscillator concentration is 175 mg/l mixed with 60% methanol and 40% propylene carbonate. The amplifier concentration is 60 mg/l and is mixed with 100% methanol. The adjustments to the concentration are made to increase the output power of the dye as well as increase its lifetime.

Good alignment of the PDL is critical to achieve high output power and good beam quality. The alignment should be constantly monitored and adjusted when necessary. A procedure for doing this can be found the instruction manual for the PDL.

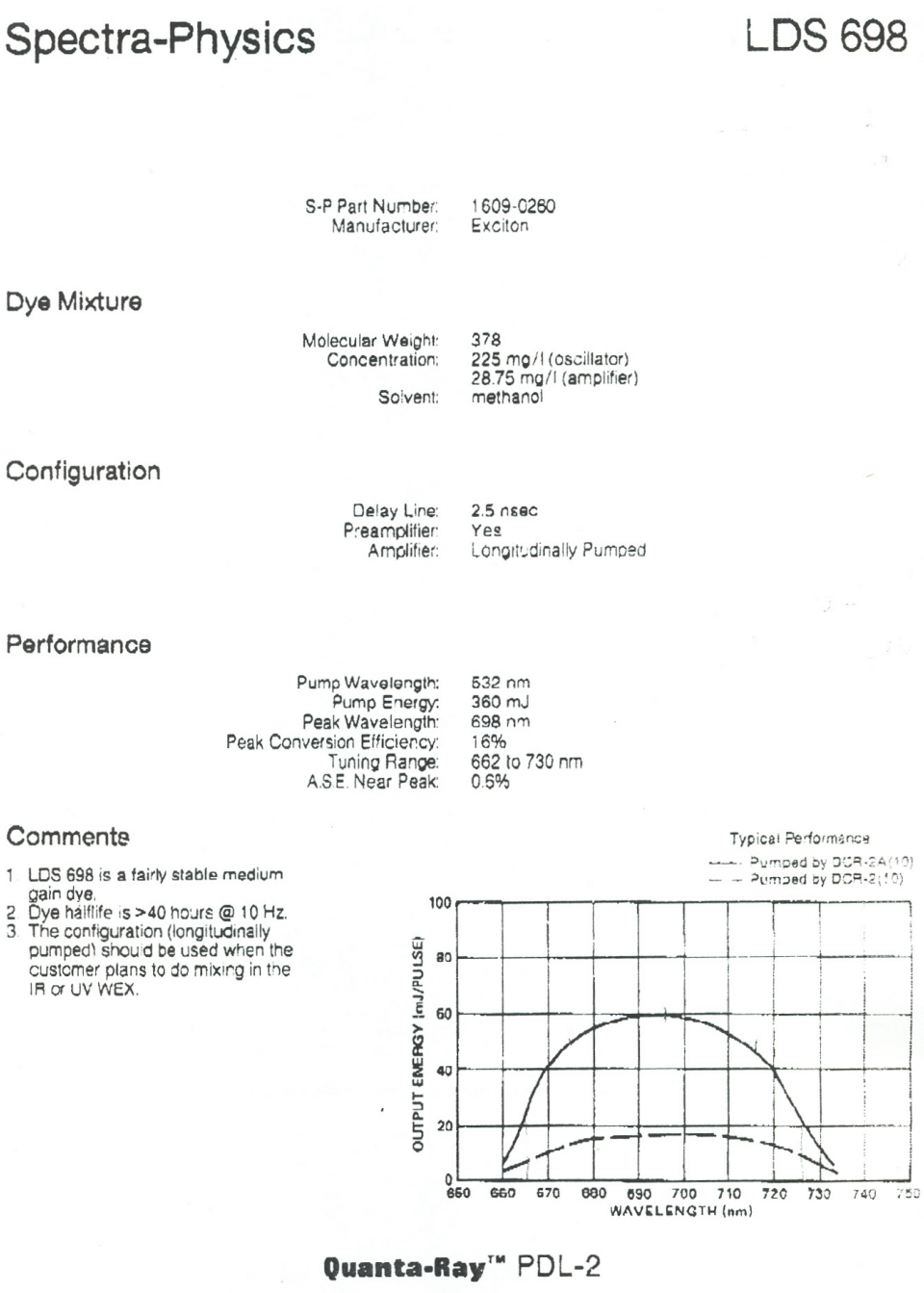

Figure B.2: Data sheet for LDS 698 laser Dye[75].

Spectra-Physics DCM

S-P Part Number: 1609/0220
Manufacturer: Exciton

Dye Mixture

Molecular Weight: 303
Concentration: 175 mg/l (oscillator)
24 mg/l (amplifier)
Solvent: methanol

Configuration

Delay Line: 2.5 nsec
Preamplifier: Yes
Amplifier: Longitudinally Pumped

Performance

Pump Wavelength: 532 nm
Pump Energy: 360 mJ
Peak Wavelength: 640 nm
Peak Conversion Efficiency: 21%
Tuning Range: 607 to 670 nm
A.S.E. Near Peak: 0.7%

Comments

1. DCM is a stable, medium-gain dye.
2. Dye halflife >300 hours @ 10 Hz.
3. Configuration given yields maximum output energy.
4. Where minimum A.S.E. is necessary, use longitudinally pumped amplifier with no preamp; this yields conversion efficiency of approximately 12% (peak).

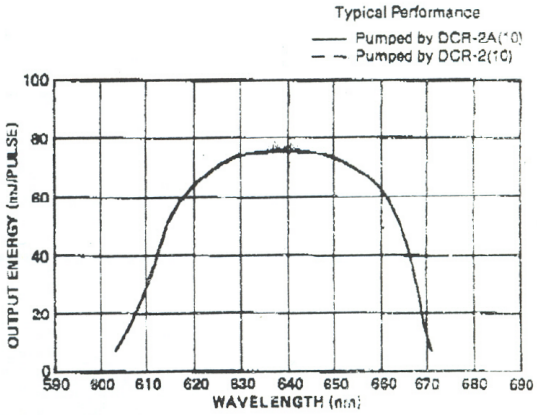

Quanta-Ray™ PDL-2

Figure B.3: Data sheet for DCM laser dye[75].

Appendix C

Published work

This appendix contains reference [53] to which I was a contributing author. The reason it is being included in the appendix is three-fold. First, it discusses in greater depth the molecular structure of NO and lists the molecular constants that determine the energy levels. Second, the paper contains a more detailed theory of the Stark effect in NO. Finally, a detailed derivation of the two state model of the Stark effect in NO as well as its properties and advantages over other existing models is discussed.

Experimental and theoretical investigation of the Stark effect for trapping cold molecules: application to nitric oxide

Bryan J. Bichsel, Michael A. Morrison,* Neil Shafer-Ray, and E. R. I. Abraham

Department of Physics and Astronomy, The University of Oklahoma,

440 West Brooks Street, Norman, Oklahoma 73019-0225

(Dated: August 8, 2005)

Abstract

Current interest in cold and ultracold molecules has brought renewed attention to the Stark effect in weakly polar diatomic molecules. At cold temperatures, molecules move adiabatically with respect to the strength of the trapping field. Thus the theory of the Stark effect involves homogeneous, static fields. For a class of weakly polar diatomic radicals with an odd number of electrons and a $^2\Pi$ ground electronic state, we critically examine, both experimentally and theoretically, widely used first- and second-order perturbation-theory approximations to the Stark shifts. Using nitric oxide as a test case, we experimentally assess these approximations at field strengths typical of current studies of cold molecules. We also experimentally and theoretically assess Stark shifts calculated using a very simple nonperturbative two-state model. These tests demonstrate that at such field strengths low-order perturbation-theory approximates to the Stark shifts are significantly in error, while the two-state model yields Stark shifts that conform to the measured data. We give expressions for the Stark energies in a generic form that can trivially be applied to any molecules in the class under consideration.

PACS numbers: 33.55.Be,33.80.Ps

*Electronic address: morrison@nhn.ou.edu

I. INTRODUCTION

Laser cooling and trapping of atoms has produced a wealth of fundamental and applied physics because these techniques allow unprecedented control of the external degrees of freedom of the trapped particles [see, for example, Refs. 1–3]. The high point of this research was the production of Bose-Einstein condensation of dilute gases in traps formed by electromagnetic fields [see, for example, Ref. 4, 5]. Because laser cooling lends itself most easily to the alkali metals, these experiments used conservative confining potentials using either magnetic fields (the Zeeman effect) or laser fields (the ac Stark effect).

Currently researchers are developing new techniques for producing cold ($T \lesssim 1\,\mathrm{K}$) and ultracold ($T \lesssim 1\,\mathrm{mK}$) molecules [74]. The idea is to trap samples of cold paramagnetic or polar molecules using techniques similar to those that have successfully trapped alkali metal atoms [6, 7]. The intense current interest in trapped cold molecules stems from several features of these systems. First, cold molecules exhibit intriguing cold-collision characteristics [8]. Second, cold molecules may serve as quantum computers [9]. Third, traps with non-zero field minima [10] may have sufficiently long trap lifetimes to enable measurement of the electric dipole moment of the electron using molecules [11, 12].

Many molecules have permanent electric dipole moments, so their quantum states exhibit large dc Stark shifts. This property can be exploited to construct deep electrostatic confining potentials [7]. The present paper concerns the dc Stark shift under experimental conditions appropriate to electrostatic trapping of a promising class of polar molecules: diatomic radicals with $^2\Pi$ ground states. As an exemplar we have chosen nitric oxide (NO) [13]. Although NO serves as our test system, we present equations for the Stark shifts to the ground electronic state energy of other polar radicals such as LiO, OH, ClO, BeH, SH, PbF, and CH.

Prior theoretical [14, 15] and experimental [16–21] research on the Stark effect in NO focused on microwave spectroscopy, a type of measurement in which the applied electric field is quite weak. This feature has two consequences that do not necessarily pertain to the much stronger fields in current Stark-effect-based techniques for cooling and trapping molecules. First, for the weak fields used in microwave spec-

troscopy, hyperfine effects must be incorporated into the theoretical analysis [18, 22–27]. Second, for such fields second-order perturbation theory—the quadratic Stark effect—accurately approximates the Stark shifts.

In Sec. IV we demonstrate that for the much stronger external fields being used in contemporary cold-molecule experiments, the quadratic Stark effect can be severely inaccurate. As an alternative, we present in Sec. III a two-state model that yields extremely simple nonperturbative equations for the Stark shifts. We investigate the comparative accuracy of these perturbative and nonperturbative theories via measurements in an apparatus (described in Sec. IV), that produces cold NO molecules [13]. In Sec. IV we show data that quantifies the severity of the error in the equations of the quadratic Stark effect and the greater accuracy that results from the equations of our two-state model.

To facilitate using these equations for other radicals we present "generic forms" of these equations that can be applied trivially to any diatomic with a $^2\Pi$ ground electronic state [for detailed information about these molecules, see the compilation in Ref. 28]. In Sec. IV we use these generic equations to explore the ranges of electric-field strengths for which perturbation theory breaks down.

The physics of radicals with a $^2\Pi$ ground state is complicated by Λ-doubling, a result of the breakdown of the Born-Oppenheimer approximation. To define a physical context for discussion of our results and to establish notation for the derivations in Sec. III, we begin in Sec. II by summarizing the relevant physics of zero-field states of molecules of this class. We also present contemporary values of spectroscopic and other data needed to calculate zero-field energies and Stark shifts for NO.

II. RADICALS WITH $^2\Pi$ GROUND STATES.

Molecules such as nitric oxide (NO) stand out among stable diatomic radicals in that they have an odd number of electrons and a $^2\Pi$ ground-state term. The latter corresponds to quantum numbers $S = 1/2$ for the total electronic spin $\mathbf{S}$ and $\Lambda = \pm 1$ for the projection of the total electronic orbital angular momentum on the internuclear axis $\mathbf{R}$. In its ground electronic state, NO is an open-shell, weakly polar radical whose dominant orbital configuration is $1\sigma^2\,2\sigma^2\,3\sigma^2\,4\sigma^2\,5\sigma^2\,1\pi^4\,2\pi$. In this state, spin-orbit

interactions yield a multiplet with $\Omega \equiv \Lambda + \Sigma = \pm 1/2, \pm 3/2$, where the quantum number Σ corresponds to the projection of $\mathbf{S}$ on $\mathbf{R}$. The spin-orbit multiplet is regular, the $^2\Pi_{3/2}$ level lying above the $^2\Pi_{1/2}$ level [29, 30]. The quantitative effects of the spin-orbit interaction on the Born-Oppenheimer energies in the ground electronic state of NO are shown (to scale) in Fig. 1(a).

In NO, coupling of the electron spin to the internuclear axis is sufficiently strong that for low-lying rotational states, this molecule is accurately described by Hund's case (a) [17, 23, 31, 32]. Strictly, this case is appropriate for values of the quantum number J, which corresponds to the total angular momentum excluding nuclear spin, such that $|\Lambda\, A_{v,\Omega}| \gg 2JB_v$, where $A_{v,\Omega}$ is the spin-orbit coupling constant [see Eq. (1b)], and B_v is the rotational constant for the v^{th} vibrational state [33, 34]; for NO, Gallagher et al. [17] give $A_{0,1/2}/B_0 \approx 75$.

For any molecule in a rovibronic state with $|\Lambda| > 0$, the molecular energies (for fixed Λ, Σ, Ω, v, J, and laboratory-frame projection quantum number M_J) are two-fold degenerate, because the electronic Hamiltonian is invariant under reflection in a plane that contains the internuclear axis. The *rotational* Hamiltonian, however, perturbs these electronic states, shifting their energies and lifting this degeneracy. In NO, for example, the rotational Hamiltonian couples the $^2\Pi_{1/2}$, $^2\Pi_{3/2}$, and $^2\Sigma_{1/2}$ rovibronic states so that the actual ground state is a superposition of these states [26, 35–37]. This coupling results in a splitting of each rotational level (of a particular vibrational manifold) into two nearly degenerate levels with opposite total parity. It also causes a breakdown of the Hund's case (a) description [16, 32, 34–36]. The rotational $^2\Pi_{1/2}$ states of NO are more accurately described by case a_β, "an intermediate case, slightly removed from Hund's case (a)" [18]. The pure Hund's case (a) description, however, is accurate for the $^2\Pi_{3/2}$ state, because of the comparatively small [20] influence of the rotational Hamiltonian [see §8 of Ref. 38].

Due to mixture of $\pm\Lambda$ states, each $2(2J+1)$-fold degenerate rovibronic energy level splits into two closely spaced $(2J+1)$-fold degenerate sublevels. This so-called Λ-*doublet splitting* was first observed in NO in microwave measurements of pure rotational spectra by Burrus and Gordy [16]. The resulting sublevels of the Λ doublet are most often labeled e and f [39, 40]. The splitting between these sublevels due to the rotational Hamiltonian increases with increasing J, accelerating the transition

from Hund's case (a) to (b) as J increases. The Λ doublet splitting for the lowest rovibronic level of the $^2\Pi_{1/2}$ state is shown (on an expanded scale) in Fig. 1(b).

In analyses of pure rotational spectra [16–18, 20] or of weak-field Stark-effect measurements of the dipole moment of NO [19, 21], one must take into account magnetic hyperfine effects. Typical zero-field hyperfine splittings for NO [21] range from 0.0013–0.0027 cm^{-1}. But this energy range corresponds to trap depths of a few μK, which is much lower than the depth of current Stark traps for molecules [7]. Hence we shall neglect nuclear spin and hyperfine coupling.

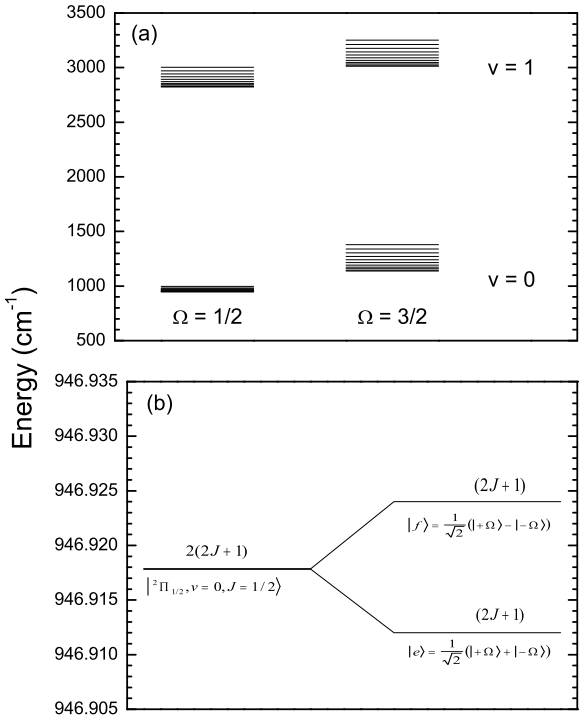

FIG. 1: Zero-field rovibronic energies of $N^{14}O^{16}$ relative to a zero of energy at the lowest spin-orbit level of the ground electronic term at the equilibrium internuclear separation R_e. (a) The 11 lowest rotational energies for the $v = 0$ and $v = 1$ vibrational manifolds of the $^2\Pi_{1/2}$ and $^2\Pi_{3/2}$ fine-structure levels. (b) The energies of the Λ-doublet levels for the $J = 1/2$ states of the $v = 0$ manifold of the $^2\Pi_{1/2}$ electronic state (on an expanded energy scale). Each level is labeled by its degree of degeneracy (above the line) and by the appropriate state designations (below the line); for the e and f states, see Eq. (6b).

A. The zero-field molecular states and energies

We denote eigenvectors of the Born-Oppenheimer *electronic* Hamiltonian $\hat{\mathcal{H}}^{\mathrm{e}}$ by $|\alpha, S, \Lambda, \Sigma, \Omega, J\rangle$, where the (signed) quantum numbers Λ, Σ, and Ω refer to projections along the internuclear axis, the z axis of the molecular (body-fixed) coordinate system. The quantum number S, correspond to total electronic spin, and α denotes the electronic energy (e.g., X, A, a, etc.). For NO, which essentially belongs to Hund's case (a), the quantum number $\Omega \equiv \Lambda + \Sigma$ is redundant. It's useful, though, to include Ω as a state label because Ω identifies the sub-levels that result from the spin-orbit interaction.

Absent spin-orbit interactions, the Born-Oppenheimer electronic energy $E^{(\mathrm{BO})}_{\Lambda,\Sigma}(R)$, the eigenvalue of $\hat{\mathcal{H}}^{\mathrm{e}}$ for electronic state $|\alpha, S, \Lambda, \Sigma, \Omega, J\rangle$, depends on the spin multiplicity $2S+1$ and on the magnitude—but not the sign—of Λ. For an arbitrary angular momentum coupling scheme, adding the spin-orbit Hamiltonian to $\hat{\mathcal{H}}^{\mathrm{e}}$ results in states in which neither Λ nor Σ are rigorously good quantum numbers. Since the sum $\mathbf{\Lambda} + \mathbf{\Sigma}$ is a constant of the motion, spin-orbit states are labeled by Ω. In the Hund's case (a) idealization, however, Σ and Λ remain good quantum numbers and are used as state labels [32, 34, 39]. For a $^2\Pi$ state, the allowed values of Ω are $\pm 1/2$ and $\pm 3/2$, but the spin-orbit energies depend only on the magnitude of Ω.

Neglecting second-order corrections [see §2.4.1 of Ref. 41], the spin-orbit shifts to $E^{(\mathrm{BO})}_{\Lambda,\Sigma}(R)$ are the diagonal matrix elements of the spin-orbit Hamiltonian in the basis of Born-Oppenheimer electronic states. The first-order shift, written in terms of the spin-orbit coupling constant $A_\Omega(R)$, is

$$A_\Omega(R)\,\Lambda\,\Sigma = \langle \alpha, S, \Lambda, \Sigma, \Omega, J \mid \hat{\mathcal{H}}^{SO} \mid \alpha, S, \Lambda, \Sigma, \Omega, J\rangle\,. \tag{1a}$$

The resulting fine-structure levels are equally spaced about the Born-Oppenheimer electronic energy. Following Huber and Herzberg [42], we choose the zero of energy at the lowest spin-orbit level of the ground electronic term at equilibrium internuclear separation R_e. Thus $A_{1/2}(R_e) = 0$, and the energy of the upper spin-orbit level is $A_{3/2}(R_e) > 0$. When we include rovibrational motion, we measure spin-orbit level energies from the ground rovibrational state, so $A_{0,1/2} = 0$.

Since the molecule vibrates, the actual spin-orbit constant is the average of $A_\Omega(R)$

over a vibrational state of the molecule,

$$A_{v,\Omega} = \langle v \mid A_\Omega(R) \mid v \rangle_R = A_\Omega(R_e) - \chi_e(v + \tfrac{1}{2}), \tag{1b}$$

where the spectroscopic constant χ_e corrects the equilibrium spin-orbit coupling constant $A_\Omega(R_e)$ to allow for vibrational motion, and the subscript R signifies integration over the internuclear separation.

For a Hund's case (a) molecule the Born-Oppenheimer rovibronic states are represented by the direct products [43]

$$|\alpha, v, S, \Lambda, \Sigma, \Omega, J, M_J\rangle = |\alpha, S, \Lambda, \Sigma, \Omega, J\rangle \otimes |v\, J\rangle \otimes |J, M_J, \Omega\rangle\,. \tag{2}$$

Here the vibrational state is denoted $|v, J\rangle$. The quantum number J corresponds to the angular momentum operator (sans nuclear spin), i.e., the sum of the total electronic angular momentum and the rotational angular momentum of the molecule $\mathbf{N}$ [75]:

$$\hat{\boldsymbol{J}} \equiv \hat{\mathbf{L}} + \hat{\mathbf{S}} + \hat{\mathbf{N}}. \tag{3}$$

The (symmetric top) rotational state $|J, M_J, \Omega\rangle$ is an eigenvector of $\hat{J}^2$, $\hat{J}_Z$, and $\hat{J}_z$ [see §1.3.3 of Ref. 41], where the subscripts Z and z refer to the polar axis of the (space-fixed) laboratory frame and the (body-fixed) molecular frame, respectively. Since rotation takes place in the plane of the internuclear axis, $\mathbf{N}$ is perpendicular to this axis. Hence the projection of $\mathbf{N}$ along the internuclear axis is zero, and the quantum number that corresponds to J_z is $\Omega = \Lambda + \Sigma$. The ket $|\alpha, S, \Lambda, \Sigma, \Omega, J\rangle$ is an eigenvector of the Born-Oppenheimer electronic Hamiltonian and that part of the rotational Hamiltonian [Eq. (7b) below] whose matrix elements are diagonal [41],

$$\widehat{\mathcal{H}}^{\text{rot}}_{\text{diag}}(R) \equiv \frac{1}{2\mu R^2}\left[\left(\hat{J}^2 - \hat{J}_z^2\right) + \left(\hat{L}^2 - \hat{L}_z^2\right) - \left(\hat{S}^2 - \hat{S}_z^2\right)\right]. \tag{4}$$

Because of the isotropy of free space, properly symmetrized eigenfunctions of the molecular Hamiltonian have well-defined total parity. In Born-Oppenheimer theory, these parity eigenfunctions are linear combinations of degenerate rovibronic stationary-state wave functions that have positive and negative projection quantum numbers Ω (for fixed $\Omega \neq 0$).

These linear combinations are eigenfunctions of the vertical reflection operator $\hat{\sigma}_v(xz)$, where xz signifies a plane containing the internuclear axis (the z axis

of the molecular reference frame) [see Chap. 9 of Ref. 40]. The operator $\hat{\sigma}_v(xz)$ inverts *all* coordinates, electronic and nuclear, through the origin [31]. When $\hat{\sigma}_v(xz)$ acts on a *rovibronic state* $|\alpha, v, S, \Lambda, \Sigma, \Omega, J, M_J\rangle$, the resulting eigenvalues $\pi = \pm 1$ define the total parity of the state [76]. At first glance, it would seem easy to construct properly symmetrized rovibrational states by simply adding or subtracting states $|\alpha, v, S, \Lambda, \Sigma, \Omega, J, M_J\rangle$ with positive and negative values of the angular-momentum projection quantum numbers:

$$|v, |\Lambda|, |\Sigma|, J, M_J, |\Omega|, \pi\rangle = \frac{1}{\sqrt{2}}\Big(|\alpha, v, S, \Lambda, \Sigma, \Omega, J, M_J\rangle \pm |\alpha, v, S, -\Lambda, -\Sigma, -\Omega, J, M_J\rangle \Big) \tag{5}$$

The problem is that it's not necessarily the case that the + sign on the right-hand side of this linear combination corresponds to even parity ($\pi = +1$) and the − sign corresponds to odd parity. Rather, *the total parity of a group of energy levels, such as the upper and lower states of the* Λ *doublet, alternate with increasing* J. In this alternation lies the usefulness of the e/f symmetry classification scheme: in this scheme the signifiers, such as $\pi(-1)^{J-1/2}$ for a molecule with an odd number of electrons, factor out this J-dependence and so are *independent of the rotational state of the molecule* [34]. The values of these signifiers are therefore referred to as the rotationless parity of the rovibronic state [77]. The e/f classification scheme of a rovibronic state gives no more information than the total-parity (π) scheme, but because the e/f scheme is "rotationless," it's much more convenient [78].

Except for molecules with an even number of electrons in an electronic state in which $\Lambda = \Omega = 0$, construction of the e/f rovibronic eigenvectors proceeds in a straightforward manner depending on whether the molecule has an even or odd number of electrons. For a molecule such as NO that has an odd number of electrons in an electronic state with $|\Lambda| > 0$, the properly symmetrized *rovibronic* states wave functions have the form [43–46]

$$|\alpha, v, S, \Lambda, \Sigma, \Omega, J, M_J, e/f\rangle = \frac{1}{\sqrt{2}}\Big(|\alpha, v, S, \Lambda, \Sigma, \Omega, J, M_J\rangle \pm (-1)^{S+1} |\alpha, v, S, -\Lambda, -\Sigma, -\Omega, J, M_J\rangle \Big), \tag{6a}$$

where the + sign yields an e state, and − yields an f state. For NO in a $^2\Pi$ state

$S = 1$, so the e/f rovibronic states are

$$|\alpha, v, S, \Lambda, \Sigma, \Omega, J, M_J, e/f\rangle = \frac{1}{\sqrt{2}}\Big(|\alpha, v, S, \Lambda, \Sigma, \Omega, J, M_J\rangle \pm |\alpha, v, S, -\Lambda, -\Sigma, -\Omega, J, M_J\rangle \Big). \tag{6b}$$

The rotational Hamiltonian lifts the degeneracy of the states (6b).

In addition to the spin-orbit operator, electronic and rotational terms in the non-relativistic molecular Hamiltonian can mix the Born-Oppenheimer states of Eq. (2) and change the corresponding energies [39, 41]. For the states and processes of interest here, these corrections are negligible except for those due to terms in the rotational Hamiltonian that induce the Λ-doublet splitting. The rotational Hamiltonian is

$$\hat{\mathcal{H}}^{\rm rot} = \frac{1}{2\mu R^2}\,\hat{\mathbf{N}}^2, \tag{7a}$$

where μ is the reduced mass of the molecule. With the definition (3) this Hamiltonian assumes the form [41]

$$\hat{\mathcal{H}}^{\rm rot} = \widehat{\mathcal{H}}^{\rm rot}_{\rm diag} + + \hat{\mathcal{H}}^{\rm SE} + \hat{\mathcal{H}}^{\rm Sun} + \hat{\mathcal{H}}^{\rm Lun}, \tag{7b}$$

where the part of $\hat{\mathcal{H}}^{\rm rot}$ that is diagonal in the Hund's (a) basis is given by Eq. (4). The operator $\widehat{\mathcal{H}}^{\rm rot}_{\rm diag}$ does not couple different electronic states; its expectation value is just the rotational contribution to the energy of the state $|\alpha, v, S, \Lambda, \Sigma, \Omega, J, M_J\rangle$. Of the other terms, $\hat{\mathcal{H}}^{\rm SE}$ is the spin-electronic term, which mixes states of the same Ω and S but different Λ and Σ, and $\hat{\mathcal{H}}^{\rm Sun}$ is the spin-uncoupling term, which mixes states with different $|\Omega|$ that have the same Λ and S but different Σ [see §7 of Ref. 38]; this term contributes to the rotational energy [*vide infra* Eq. (9) below] but does not split the Λ doublet. The third term, the L-uncoupling operator

$$\hat{\mathcal{H}}^{\rm Lun} = -\frac{1}{2\mu R^2}\,(J^+L^- + J^-L^+), \tag{8}$$

mixes different rovibronic states with the same Σ and S but different Λ and hence different Ω. Since $\hat{\mathcal{H}}^{\rm Lun}$ couples states with $\Delta\Lambda = \pm 1$, $\Delta\Sigma = 0$, and $\Delta\Omega = \pm 1$, this operator is responsible for splitting the Λ doublet.

In the Hund's case (a) basis $\{\ |\,\alpha, v, S, \Lambda, \Sigma, \Omega, J, M_J\rangle\ \}$, the Born-Oppenheimer rovibrational energy measured from $E = 0$ at the ground rovibrational state of the

lowest spin-orbit level is [17, 20, 29, 47, 48]

$$\begin{aligned}\epsilon_{v,J,\Omega} = A_{v,\Omega} &+ \omega_e(v+\tfrac{1}{2}) - \omega_e x_e (v+\tfrac{1}{2})^2 \\ &+ B_v\left[(J+\tfrac{1}{2})^2 - \Lambda^2\right] - D_v J^2 (J+1)^2 \\ &\pm \left[B_v^2 (J+\tfrac{1}{2})^2 + \tfrac{1}{4}\Lambda^2 A_{v,\Omega}(A_{v,\Omega} - 4B_v)\right]^{1/2}.\end{aligned} \tag{9}$$

The first line of this equation is the sum of the spin-orbit coupling constant $A_{v,\Omega}$ [*vide infra* Eq. (1a)] and the vibrational energy, which contains the harmonic and anharmonic frequencies ω_e and $\omega_e x_e$, respectively. The second and third lines of (9) give the rotational energy. [Note that the rotational energy includes the displacement due to the spin-uncoupling operator in the rotational Hamiltonian (7b).] For a regular spin-orbit multiplet (e.g., in NO) the + and − signs in the rotational energy correspond to $|\Omega| = 3/2$ and $1/2$, respectively. (Gallagher et al. [17] give a useful form of the rotational energy that is applicable if spin uncoupling is weak.) In the rotational energy, the rotational constants B_v and D_v, corrected to incorporate the rotation-vibration interaction in vibrational state v, are [48]

$$B_v \equiv B_e - \alpha_e(v+\tfrac{1}{2}) \tag{10a}$$

$$D_v \equiv D_e + \beta_e(v+\tfrac{1}{2}), \tag{10b}$$

where B_e and D_e are the equilibrium rotational and centrifugal distortion constants, and α_e and β_e are vibration-rotation interaction constants.

To calculate the Λ-doublet splitting one should use the e/f-symmetrized molecular functions in Eq. (6b) [15, 38, 47]. The L-uncoupling operator of Eq. (8) does not mix e and f states. *In an analysis of the Stark effect, these rotationless parity labels therefore pertain to the zero-field states of the* Λ *doublet* (see Sec. III). In NO the perturbing $^2\Sigma_{1/2}$ state lies *above* the $^2\Pi$ state [37]. Both the e and f levels are *lowered* by the L-uncoupling operator, but not by the same amount; Geuzebroek et al. [49] have unambiguously verified by two experiments that, as illustrated in Fig. 1(b), the e state (which for the lowest rotational state has total parity $\pi = +1$) lies *below* the f state ($\pi = -1$).

The splitting between the energy levels of the Λ doublet,

$$\Delta\epsilon^{fe}_{v,J,\Omega} \equiv \epsilon^{f}_{v,J,\Omega} - \epsilon^{e}_{v,J,\Omega} > 0, \tag{11a}$$

is given to second order in the L-uncoupling operator by [17, 38, 43, 48]

$$\Delta\epsilon^{fe}_{v,J,1/2} = p_v(J+\tfrac{1}{2}), \qquad \text{for } {}^2\Pi_{1/2} \tag{11b}$$

$$\Delta\epsilon^{fe}_{v,J,3/2} = q_v(J^2-\tfrac{1}{4})(J+\tfrac{3}{2}), \qquad \text{for } {}^2\Pi_{3/2}. \tag{11c}$$

The constants p_v and q_v are defined in terms of the spin-orbit constant, the rotational constants, and the separation in energy $\Delta E^{\Sigma,\Pi} \equiv E_\Sigma - E_\Pi > 0$ between the $X^2\Pi$ term and the *higher-lying* perturbing $A^2\Sigma_{1/2}$ term as [35, 36]

$$p_v \equiv \frac{4A_{v,3/2}B_v}{\Delta E^{\Sigma,\Pi}}, \qquad \text{for } {}^2\Pi_{1/2} \tag{12a}$$

$$q_v \equiv \frac{8B_v^2}{A_{v,3/2}\,\Delta E^{\Sigma,\Pi}}, \qquad \text{for } {}^2\Pi_{3/2}. \tag{12b}$$

These expressions assume that the shapes of the $X^2\Pi$ and $A^2\Sigma_{1/2}$ potential energy curves are identical and hence that these states have the same vibrational wave functions, an approximation that is valid for NO [41]. (For details concerning the effect of Λ doubling on rotational states in the $^2\Pi$ states, see Table III of Ref. [18].) Taking into account the Λ-doublet splitting, the zero-field rovibronic energies are [see also Eq. (3.5) of Ref. 17]

$$\epsilon^{e/f}_{v,J,\Omega} = \epsilon_{v,J,\Omega} \pm \tfrac{1}{2}\Delta\epsilon^{fe}_{v,J,\Omega}, \tag{13}$$

where $\epsilon_{v,J,\Omega}$ is the Born-Oppenheimer rovibronic energy (9), $\Delta\epsilon^{fe}_{v,J,\Omega}$ is the Λ-doublet splitting of Eq. (11), and the $+$ and $-$ signs correspond to the f and e states, respectively.

B. Molecular data for NO.

The molecular constants required to evaluate the zero-field energies (9) are identified and their measured values given for NO in Tbl. I. In addition to these constants, one requires values for the spin-orbit constants of Eq. (1a). Hallin et al. [53] experimentally determined the spin-orbit constants for low-lying vibrational states of the $^2\Pi_{3/2}$ level; for the ground and first vibrational states, they obtained $A_{0,3/2} = 123.139\,07(25)\,\mathrm{cm}^{-1}$ and $A_{1,3/2} = 122.894\,90(27)\,\mathrm{cm}^{-1}$ [see Refs. 20, 30, 51, 54]. The corresponding *equilibrium* spin-orbit constant for the ground electronic state is [42] $A_{3/2}(R_e = 1.150\,77\,\text{Å}) = 119.82\,\mathrm{cm}^{-1}$. The separation between the interacting $^2\Pi$ and $^2\Sigma_{1/2}$ Born-Oppenheimer electronic states is [29] $\Delta E^{\Sigma,\Pi} = 43\,966\,\mathrm{cm}^{-1}$.

physical significance	symbol	value (cm^{-1})
rotational constant at equilibrium	$B_e(^2\Pi_{3/2})$	1.72016
	$B_e(^2\Pi_{1/2})$	1.67195
centrifugal distortion constant	$D_e(^2\Pi_{3/2})$	10.2×10^{-6}
	$D_e(^2\Pi_{1/2})$	5.36×10^{-6}
rovibrational interaction constant	$\alpha_e(^2\Pi_{3/2})$	0.0182
	$\alpha_e(^2\Pi_{1/2})$	0.0171
harmonic angular frequency	$\omega_e(^2\Pi_{3/2})$	1904.04
	$\omega_e(^2\Pi_{1/2})$	1904.20
anharmonicity constant	$\omega_e x_e(^2\Pi_{3/2})$	14.100
	$\omega_e x_e(^2\Pi_{1/2})$	14.075

TABLE I: Molecular constants in cm^{-1} for the $^2\Pi$ levels of $N^{14}O^{16}$. Data from Refs. [42, 48, 50, 51]. For variations in measured spectroscopic constants, see [52]. For further references, see footnotes to the table on $N^{14}O^{16}$ in Huber and Herzberg [42].

The constant p_v in the Λ-doublet splitting energy (11) depends on the vibrational state. One can experimentally determine this splitting from the frequency separation of Λ-doublet spectral lines for rotational transitions $J \to J+1$. From analysis of high-resolution Fourier spectra, Amiot et al. [55] [corrected in Tbl. III of Ref. 56] determined the values $p_0 = 0.011\,6893(80)\,\mathrm{cm}^{-1}$ and $p_1 = 0.011\,6878(14)\,\mathrm{cm}^{-1}$ [for related determinations see Refs. 16, 17, 20, 27, 56]. For the Λ-doublet parameters of the $^2\Pi_{3/2}$ level, these authors obtained $q_0 = 9.507(74) \times 10^{-6}\,\mathrm{cm}^{-1}$ and $q_1 = 9.443(68) \times 10^{-6}\,\mathrm{cm}^{-1}$. The resulting Λ-doublet splittings are in good accord with the theoretical calculations of de Vivie and Peyerimhoff [37], who discuss the theoretical underpinnings of this phenomenon and the wide variation in contemporary experimental values of q_v [see also Refs. 21, 35, 36].

C. Dipole moments for NO.

To evaluate the Stark shifts, we require the vibrationally averaged dipole moments for the $v = 0$ and $v = 1$ states of the spin-orbit state of interest. This quantity, the permanent electric dipole moment in the v^{th} vibrational state [40]

$$\mu_{v,\Omega} \equiv \langle \alpha, v, S, \Lambda, \Sigma, \Omega, J, M_J \mid \mu \mid \alpha, v, S, \Lambda, \Sigma, \Omega, J, M_J \rangle \,, \tag{14}$$

depends on the magnitude but not on the sign of Ω. The permanent dipole moment for the $^2\Pi_{1/2}$ state of $N^{14}O^{16}$ has been measured, calculated, and discussed extensively; key results appear in Tbl. II. The experimental results in this table come from microwave spectra except the value of Neumann [57], which was determined using a molecular-beam resonance technique. These measurements cannot determine the *sign* of $\mu_{v,\Omega}$. But the calculations of Billingsley [58], who used the optimized-valence-configuration multiconfiguration self-consistent-field method, show the polarity of the ground state to be N^-O^+, i.e., the dipole moment points from the nitrogen nucleus to the oxygen nucleus and therefore, by definition, is negative. This finding explains the signs in Tbl. II. The more recent calculations of Refs. [59, 60] entail multireference singles-plus-doubles configuration-interaction calculations. The values we use in the calculations of Sec. IV are those of Rawlins et al. [61]. These authors analyzed experimental data for vibrational-transition branching ratios, previous measurements of the static dipole moment, and absorption coefficients for transitions from the ground to the first vibrational state. They then used a nonlinear least-squares fit to determine a dipole moment function $\mu_\Omega(R)$, from which they calculate the vibrationally averaged moments in Tbl. II.

III. THEORY: THE STARK EFFECT.

We consider a static, homogeneous external electric field of strength $\mathcal{E}$ that points along the laboratory-frame Z axis. The operator corresponding to the potential energy of interaction of this field with the permanent dipole moment $\boldsymbol{\mu}$ of the molecule is

$$\hat{\mathcal{H}}^{\mathcal{E}} = -\boldsymbol{\mu} \cdot \boldsymbol{\mathcal{E}} = -\mu \mathcal{E} \cos\theta, \tag{15}$$

where θ is the polar angle of the field axis with respect to the internuclear axis.

source	$\mu_0(D)$	$\mu_1(D)$
[E] Liu et al. [62]	0.1595(15)	0.1425(16)
[E] Burrus and Graybeal [19]	0.158 ± 0.006	
[E] Neumann [57]	0.15782 ± 0.0002	
[E] Hoy et al. [21]	0.1574	0.1416
[T] Billingsley[58]	−0.139	−0.119
[T] Langhoff et al. [60]	−0.169	−0.152
[E] Rawlins et al. [61]	−0.1588	−0.1406

TABLE II: Experimental (E) and theoretical (T) values for vibrationally averaged dipole moments in the ground and first-excited vibrational states in the $^2\Pi$ spin-orbit states of $N^{14}O^{16}$. Values are given in Debye, where $1\,\mathrm{D} = 3.33564 \times 10^{-30}\,\mathrm{cm}^{-1}$. Note that experimental measurements yield only $|\mu_{v,\Omega}|$.

Several symmetry properties of the Stark Hamiltonian $\hat{\mathcal{H}}^{\mathcal{E}}$ facilitate calculating its effect on molecular energies. First, since $\hat{\mathcal{H}}^{\mathcal{E}}$ commutes with $\hat{J}_z$, it doesn't couple states of different $|\Omega|$; nor does it couple a state with $+\Omega$ to the corresponding state with $-\Omega$. Therefore in the rovibronic basis defined by Eq. (2), whose elements we'll here abbreviate as $|\pm\Omega\rangle$, the matrix representation of the Stark Hamiltonian is diagonal:

$$\mathsf{H}^{\mathcal{E}}_{\{\,|\pm\Omega\rangle\,\}} = \begin{pmatrix} \langle\Omega \mid \hat{\mathcal{H}}^{\mathcal{E}} \mid \Omega\rangle & 0 \\ 0 & -\langle\Omega \mid \hat{\mathcal{H}}^{\mathcal{E}} \mid \Omega\rangle \end{pmatrix}, \tag{16a}$$

where we have exploited the symmetry of the molecule to relate the (non-zero) diagonal elements [15].

The Stark Hamiltonian does couple the e and f states defined in Eq. (6b), which we'll here abbreviate by $|e/f\rangle$. In this basis the diagonal matrix elements of $\hat{\mathcal{H}}^{\mathcal{E}}$ are zero, so the matrix representation is

$$\mathsf{H}^{\mathcal{E}}_{\{\,|e/f\rangle\,\}} = \begin{pmatrix} 0 & \langle e \mid \hat{\mathcal{H}}^{\mathcal{E}} \mid f\rangle \\ \langle e \mid \hat{\mathcal{H}}^{\mathcal{E}} \mid f\rangle & 0 \end{pmatrix}, \tag{16b}$$

where we have used the Hermiticity of $\hat{\mathcal{H}}^{\mathcal{E}}$ to equate the (non-zero) off-diagonal elements.

It is straightforward [15] to evaluate the sole matrix element $\langle \Omega \mid \hat{\mathcal{H}}^{\mathcal{E}} \mid \Omega \rangle$ needed to construct the representation (16a) of $\hat{\mathcal{H}}^{\mathcal{E}}$ in the $|\pm\Omega\rangle$ basis:

$$H^{\mathcal{E}}_{v,J,M_J,\Omega} = \langle \alpha, v, S, \Lambda, \Sigma, \Omega, J, M_J \mid \hat{\mathcal{H}}^{\mathcal{E}} \mid \alpha, v, S, \Lambda, \Sigma, \Omega, J, M_J \rangle \tag{17a}$$

$$= -\mathcal{E}\, \mu_{v,\Omega} \langle J, M_J, \Omega \mid \cos\theta \mid J, M_J, \Omega \rangle\,, \tag{17b}$$

where $|J, M_J, \Omega\rangle$ is the rotational eigenstate in Eq. (2) and $\mu_{v,\Omega}$ is the vibrationally averaged dipole moment defined in Eq. (14).

To evaluate the matrix element of $\cos\theta$ in Eq. (17b), we exploit the fact that the laboratory-frame polar angle θ is the direction cosine $\boldsymbol{\alpha}^z_Z$. The diagonal matrix element of this quantity with respect to the rotational state $|J, M_J, \Omega\rangle$ is the expectation value of $\boldsymbol{\alpha}^z_Z$ in this state, the value of which is [see §3.9 and Table 3.2 of Ref. 39]

$$\langle J, M_J, \Omega \mid \boldsymbol{\alpha} \mid J, M_J, \Omega \rangle = \langle \boldsymbol{\alpha}^z_Z \rangle = \frac{\Omega M_J}{J(J+1)}. \tag{18}$$

Hence the Stark matrix element (17b) is

$$H^{\mathcal{E}}_{v,J,M_J,\Omega} = -\mu_{v,\Omega}\mathcal{E}\frac{\Omega M_J}{J(J+1)}, \qquad M_J = -J, \ldots, +J. \tag{19}$$

A. The Stark effect in a two-state model

Although the zero-field states $|\alpha, v, S, \Lambda, \Sigma, \Omega, J, M_J, e/f\rangle$ are not degenerate, the Λ-doublet splitting is so small that these states are well-separated in energy from all other rovibronic states [see Fig. 1(a)]. (This feature has been verified experimentally by Gallagher and Johnson [18] and by Hoy et al. [21] [see also Refs. 14, 15].) Moreover, applied fields in current cold molecular experiments are sufficiently strong that the product $\mu_{v,\Omega}\,\mathcal{E}$ is much larger than the hyperfine splitting [63]. Under these circumstances, we can determine the Stark energies by modeling the molecule as a two-state system [64]. As we shall show in Sec. IV, such a *nonperturbative* approach is required for field strengths larger than a few kV/cm, because second-order perturbation theory, which leads to the familiar "quadratic Stark effect" [14, 21], is highly inaccurate for these field strengths.

We therefore assume that the states $|\alpha, v, S, \Lambda, \Sigma, \Omega, J, M_J, e/f\rangle$ of Eq. (6b) for fixed v, J, Λ, Σ, and Ω constitute a basis of $2(2J+1)$ eigenvectors in which we

can expand the desired eigenvector of the total Hamiltonian $\hat{\mathcal{H}} = \hat{\mathcal{H}}^0 + \hat{\mathcal{H}}^{\mathcal{E}}$. Since $\hat{\mathcal{H}}^{\mathcal{E}}$ commutes with $\hat{J}_Z$, the Hamiltonian matrix in this basis is block diagonal with respect to the magnetic quantum number M_J. Hence we can consider each 2×2 submatrix for fixed M_J separately and obtain the eigenvalues of $\hat{\mathcal{H}}$ by diagonalizing [79]

$$\mathsf{H}_{\{\,|e/f\rangle\,\}} = \begin{pmatrix} H_{ee} & H_{ef} \\ H_{fe} & H_{ff} \end{pmatrix} = \begin{pmatrix} \epsilon^e_{v,J,\Omega} & \langle e \mid \hat{\mathcal{H}}^{\mathcal{E}} \mid f \rangle \\ \langle e \mid \hat{\mathcal{H}}^{\mathcal{E}} \mid f \rangle & \epsilon^f_{v,J,\Omega} \end{pmatrix}, \tag{20}$$

where the second equality follows from the symmetry properties of the e/f basis (Sec. III). The diagonal elements in $\mathsf{H}_{\{\,|e/f\rangle\,\}}$ are just the zero-field energies of the e and f states given in Eq. (13). The Hamiltonian $\hat{\mathcal{H}}$ is Hermitian, so the off-diagonal elements in this matrix are equal: $H_{fe} = H_{ef}$. We simplify the off-diagonal elements by using the orthonormality of the e/f states, viz.,

$$H_{ef} = \langle e \mid \hat{\mathcal{H}}^0 + \hat{\mathcal{H}}^{\mathcal{E}} \mid f \rangle = \langle e \mid \hat{\mathcal{H}}^{\mathcal{E}} \mid f \rangle\,. \tag{21}$$

We can easily evaluate H_{ef} by using Eq. (6b) to express this matrix element in terms of the $\{\,\pm\Omega\,\}$ basis states:

$$\langle e \mid \hat{\mathcal{H}}^{\mathcal{E}} \mid f \rangle = \frac{1}{2}\Big[\Big(\,\langle +\Omega| + \langle -\Omega|\,\Big)\Big|\hat{\mathcal{H}}^{\mathcal{E}}\Big|\Big(\,|+\Omega\rangle - |-\Omega\rangle\,\Big)\Big]. \tag{22}$$

According to Eq. (16a), the matrix $\mathsf{H}^{\mathcal{E}}_{\{\,|\pm\Omega\rangle\,\}}$ is diagonal. So Eq. (22) simplifies to the matrix element already evaluated in Eq. (19):

$$\langle e \mid \hat{\mathcal{H}}^{\mathcal{E}} \mid f \rangle = \langle \Omega \mid \hat{\mathcal{H}}^{\mathcal{E}} \mid \Omega \rangle = H^{\mathcal{E}}_{v,J,M_J,\Omega} = -\mu_{v,\Omega}\mathcal{E}\frac{\Omega M_J}{J(J+1)}. \tag{23}$$

Diagonalizing the matrix (20) yields the Stark energies in the two-state model,

$$\begin{aligned} E^{e/f}_{v,J,M_J,\Omega} = {} & \tfrac{1}{2}(\epsilon^e_{v,J,\Omega} + \epsilon^f_{v,J,\Omega}) \\ & \pm \tfrac{1}{2}\sqrt{4|H^{\mathcal{E}}_{v,J,M_J,\Omega}|^2 + (\Delta\epsilon^{fe}_{v,J,\Omega})^2}, \end{aligned} \tag{24a}$$

where the + sign corresponds to the f state and the − sign to the e state. Noting from Eq. (13) that the average of the e and f zero-field energies is just the rovibronic energy $\epsilon_{v,J,\Omega}$ of Eq. (9), and defining the two-state Stark shift

$$\Delta E^{\mathcal{E}}_{v,J,M_J,\Omega} = \tfrac{1}{2}\sqrt{4|H^{\mathcal{E}}_{v,J,M_J,\Omega}|^2 + (\Delta\epsilon^{fe}_{v,J,\Omega})^2}, \tag{24b}$$

we can write Eq. (24a) as

$$E^{e/f}_{v,J,M_J,\Omega} = \epsilon_{v,J,\Omega} \pm \Delta E^{\mathcal{E}}_{v,J,M_J,\Omega}. \tag{24c}$$

This form emphasizes that Eq. (24b) gives the Stark shifts *to the zero-field Born-Oppenheimer rovibronic energies* $\epsilon_{v,J,\Omega}$ *of Eq. (9), not to the* e/f *energies* $\epsilon^{e/f}_{v,J,\Omega}$ *of Eq. (13).*

Equations (24) show that the Stark effect *increases the energies of the upper* (f) *levels* [see Fig. 1(b)] *and decreases the energies of the lower* (e) *levels* [63]. These shifts depend on the magnitude *but not on the sign* of M_J: that is, the Stark-shifted levels remain two-fold degenerate. To calculate these shifts we require only the field strength and the (averaged) dipole moments in the relevant vibronic states [see Sec. II C].

B. The strong- and weak-field limits.

Burrus and Graybeal [19] used Stark spectroscopy to measure the dipole moment for the $v = 0$ vibrational state of the $^2\Pi_{1/2}$ level of $N^{14}O^{16}$. As befits such experiments, these authors focused on the weak-field limit and included hyperfine splitting. Subsequently, Hoy et al. [21] used laser Stark spectroscopy to measure $\mu_{v,\Omega}$ for the ground and first vibrational states and considered both $^2\Pi$ levels. All these authors used perturbation theory [14, 15] to calculate the quadratic (second-order) and linear (first-order) Stark shifts. Since we want to relate the two-state results of Sec. III A to their perturbation-theory approximates, it is useful to write the Stark energy levels of Eqs. (24) as

$$E^{e/f}_{v,J,M_J,\Omega} = \epsilon^{e/f}_{v,J,\Omega} \pm (\Delta E^{\mathcal{E}}_{v,J,M_J,\Omega} - \tfrac{1}{2}\Delta\epsilon^{fe}_{v,J,\Omega}). \tag{25}$$

Hoy et al. [21], who base their spectroscopic determination of the dipole moment on the theoretical work of Mizushima [14, 15], used second-order perturbation theory to calculate Stark shifts to the e and f rovibronic $\Omega = 1/2$ energies. We can easily relate this approximation to the two-state energies of Eq. (25). Comparing the two, both analytically and numerically, affords insight into the range of field strengths where the second-order perturbative approximation is valid and sets up the comparisons of Sec. IV.

In the presence of Λ doubling, second-order perturbation theory is valid if the external electric field is sufficiently weak. In this weak-field limit the two-state Stark shift reduces to the familiar quadratic shift. To make this reduction, we first write Eq. (25) as

B The strong- and weak-field limits.

$$E^{e/f}_{v,J,M_J,\Omega} = \epsilon^{e/f}_{v,J,\Omega} \pm \frac{1}{2}\Delta\epsilon^{fe}_{v,J,\Omega} \left[\sqrt{1+4\left(\frac{H^{\mathcal{E}}_{v,J,M_J,\Omega}}{\Delta\epsilon^{fe}_{v,J,\Omega}}\right)^2} - 1\right]. \tag{26a}$$

We now expand the square root in the small parameter $|H^{\mathcal{E}}_{v,J,M_J,\Omega}/\Delta\epsilon^{fe}_{v,J,\Omega}|$ and retain only the first term, obtaining

$$E^{e/f}_{v,J,M_J,\Omega} \approx \epsilon^{e/f}_{v,J,\Omega} \pm \Delta\epsilon^{fe}_{v,J,\Omega}\left(\frac{H^{\mathcal{E}}_{v,J,M_J,\Omega}}{\Delta\epsilon^{fe}_{v,J,\Omega}}\right)^2 \tag{26b}$$

$$= \epsilon^{e/f}_{v,J,\Omega} \pm E^{(2)}_{v,J,M_J,\Omega}, \tag{26c}$$

where as usual the + and − signs refer to the f and e states, respectively. In Eq. (26c) we have identified the *second-order* correction term as the quadratic Stark shift to the zero-field e/f energies:

$$E^{(2)}_{v,J,M_J,\Omega} = \frac{[H^{\mathcal{E}}_{v,J,M_J,\Omega}(\mathcal{E})]^2}{\Delta\epsilon^{fe}_{v,J,\Omega}}. \tag{27}$$

For the second-order approximation to the Stark shift to be accurate, the applied field must be weak enough that

$$|H^{\mathcal{E}}_{v,J,M_J,\Omega}(\mathcal{E})| \ll \frac{1}{2}\,\Delta\epsilon^{fe}_{v,J,\Omega}. \tag{28}$$

The other extreme is the strong-field limit, where the field is strong enough to render the Λ-doublet splitting negligible. In this case Eq. (24c) reduces to

$$E^{e/f}_{v,J,M_J,\Omega} = \epsilon^{e/f}_{v,J,\Omega} \pm H^{\mathcal{E}}_{v,J,M_J,\Omega} = \epsilon^{e/f}_{v,J,\Omega} \mp \mu_{v,\Omega}\mathcal{E}\frac{\Omega M_J}{J(J+1)}. \tag{29}$$

The second term in this result agrees with the first-order (linear) Stark shift [14],

$$E^{(1)}_{v,J,M_J,\Omega} = \langle\Omega \mid \hat{\mathcal{H}}^{\mathcal{E}} \mid \Omega\rangle = -\mu_{v,\Omega}\mathcal{E}\frac{\Omega M_J}{J(J+1)}, \tag{30}$$

which one obtains by neglecting the Λ doublet splitting altogether [21]. The linear Stark shift raises states with $M_J < 0$ and lowers states with $M_J > 0$. Each perturbed state remains two-fold degenerate; that is, the first-order Stark shift does not alter the degeneracy of the $\pm\Omega$ states.

To conclude we write our equations for the Stark shifts in a form that is convenient for application to other molecules and for the comparisons of Sec. IV. To this end we introduce the dimensionless variable

$$\eta \equiv \frac{H^{\mathcal{E}}_{v,J,M_J,\Omega}}{\Delta\epsilon^{fe}_{v,J,\Omega}}, \tag{31}$$

which is the Stark matrix element for an arbitrary rovibronic state normalized to the splitting of the Λ doublet. In terms of this variable, Eqs. (24b), (27), and (30) for the Stark shifts become

$$\Delta E^{\mathcal{E}}_{v,J,M_J,\Omega} = \pm\sqrt{\tfrac{1}{4}+\eta^2}, \qquad \text{two-state model} \tag{32a}$$

$$E^{(2)}_{v,J,M_J,\Omega} = \pm\left(\tfrac{1}{2}+\eta^2\right), \qquad \text{second-order perturbation theory} \tag{32b}$$

$$E^{(1)}_{v,J,M_J,\Omega} = \pm\left(\tfrac{1}{2}+\eta\right), \qquad \text{first-order perturbation theory,} \tag{32c}$$

where the + and − signs refer to the f and e states, respectively. Note that because η is defined in terms of the matrix element $H^{\mathcal{E}}_{v,J,M_J,\Omega}$, this variable depends on the field strength and on the rovibronic state under consideration. Equations (32) are "generic" expressions for the Stark shifts, applicable to any molecule with a $^2\Pi$ ground state under conditions where hyperfine effects are negligible.

C. Theoretical treatments of the Stark effect.

In the preceding section, we described three ways to calculate Stark shifts for any molecule with $|\Lambda| > 0$ that is well represented by Hund's case (a) under conditions where hyperfine structure is negligible. The linear Stark shift [Eq. (26c)] results from first-order perturbation theory; this result is valid only when the Stark interaction energy is large compared to the Λ-doublet splitting. The quadratic Stark shift [Eq. (27)] results from second-order perturbation theory and assumes that the Stark energy is small compared to the Λ-doublet splitting. When this approximation holds, the first-order Stark shift is zero. The two-state model diagonalizes the Hamiltonian, assuming only that the Λ-doublet splitting and Stark interaction energies are small compared to the separation of the rovibronic level under consideration from other levels.

Other authors have considered the quadratic Stark effect for NO taking into account hyperfine structure [14, 21]. Current experiments with cold molecules produce trapped samples at temperatures on the order of $0.1 - 1\,\mathrm{K}$ [7, 65]. At these temperatures, the hyperfine splitting in NO is negligible. While introducing hyperfine interactions will be important for experiments that further cool (through evaporative or sympathetic cooling) trapped samples to energies on the size of the hyperfine splittings, this additional complexity is at present unnecessary.

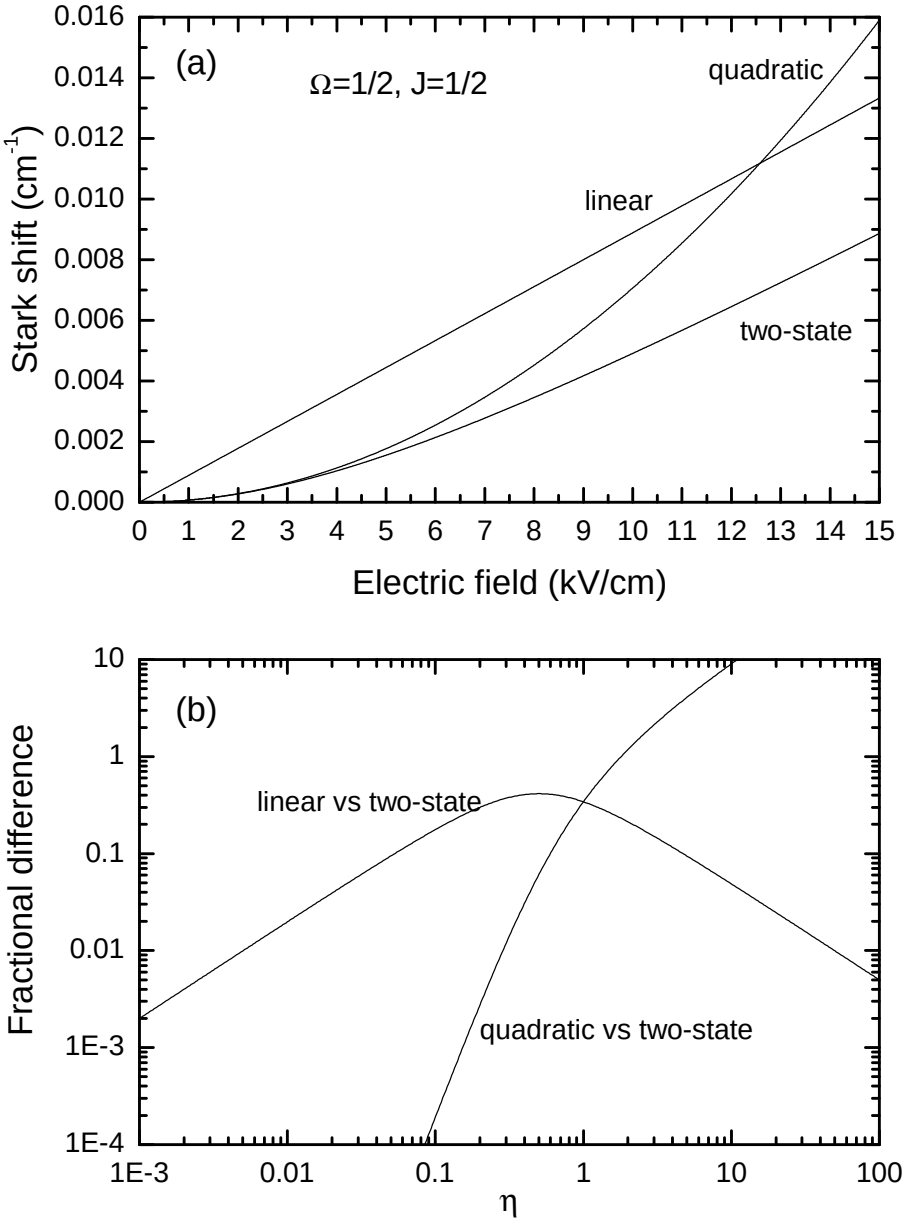

FIG. 2: (a) The dc Stark shifts for the $v = 0$, $J = 1/2$ state of the $^2\Pi_{1/2}$ spin-orbit level as a function of electric field strength. Shifts in the two-state model and in first- and second-order perturbation theory are shown over an experimentally realistic range of field strengths. (b) The fractional difference between Stark shifts, as calculated using perturbation theory and using the two-state model [see Eqs. (32)], for a rovibronic state of a Hund's case (a) molecule. First- and second-order perturbation theory give the linear and quadratic approximations, respectively. The parameter η, the Stark matrix element normalized to the Λ-doublet splitting, is defined in Eq. (31).

In Fig. 2(a), we plot the Stark shifts for the ground rovibronic state ($v = 0, J = 1/2$) of the $^2\Pi_{1/2}$ spin-orbit level as a function of field strength. This figure shows significant differences between the quadratic Stark shift and that of the two-state theory—even for relatively low electric fields. According to perturbation theory, the second-order correction lowers the energies of e states and raises the energies of f states. Qualitatively this behavior is the same as that of the two-state Stark shifts. *Quantitatively, however, the condition (28) breaks down at field strengths above a few kV/cm.* (The linear approximation is not expected to be accurate at low field strengths;,it is valid only for Stark shifts greater than the Λ-doublet splitting.) To quantify the implications of Fig. 2(a), we compare in Tbl. III Stark shifts for the f state from the (very low) field strengths at which the quadratic shift is accurate to the (very high) strength at which the linear approximation holds.

In Fig. 2(b), we compare the fractional difference between the linear and quadratic Stark shifts of Eqs. (32) to those of the two-state model. Since the dimensionless variable η of Eq. (31) depends on the dipole moment, electric field, and quantum state, *these curves show the relative accuracy of perturbation theory for any rovibronic state of any radical that can be treated in Hund's case (a) when hyperfine effects are negligible*. Especially noteworthy is the striking, rapid increase in the error of the quadratic Stark shift around $\eta = 1$.

To illustrate the behavior of Stark shifts over the range of field strength that is experimentally accessible for electrostatic trapping, we show in Fig. 3 results from the two-state model for the $J = 1/2$ and $J = 3/2$ rotational levels of the $^2\Pi_{1/2}$ state and for the $J = 3/2$ and $J = 5/2$ levels of the $^2\Pi_{3/2}$ state. In both cases we consider the ground vibrational manifold ($v = 0$). Since the Stark energies depend on the magnitude but not the sign of M_J, each Stark-shifted level remains two-fold degenerate. Because the Λ-doublet splitting is so small for $^2\Pi_{3/2}$ states, the Stark shift for these states is essentially linear over the entire range of field strengths of interest. For the $J = 3/2$ state of the $^2\Pi_{1/2}$ level, the Stark energy at 40 kV/cm is more than half of the energy of the Λ doublet, and Fig. 2(b) shows that as the field strength increases, second-order perturbation theory rapidly and significantly breaks down. Indeed, for the $J = 1/2$ rotational state of this level, this approximation is invalid for most relevant trapping fields.

$\mathcal{E}$(kV/cm)	two-state	quadratic	linear
0.5	0.00002	0.00002	0.00044
2.0	0.00026	0.00027	0.00178
5.0	0.00150	0.00169	0.00444
10.0	0.00479	0.00676	0.00889
20.0	0.01287	0.02704	0.01778
50.0	0.03898	0.16897	0.04444
100.0	0.08323	0.67589	0.08889
300.0	0.26088	6.08300	0.26666
500.0	0.43862	16.8970	0.44443
1000.0	0.88303	67.5890	0.88886

TABLE III: Comparison of two-state, quadratic, and linear Stark shifts in cm^{-1} for the $v = 0$, $J = 1/2$, $M_J = 1/2$ zero-field energy of the e state of the $^2\Pi_{1/2}$ level in NO as a function of electric field strength $\mathcal{E}$ in kV/cm. The "linear" column gives the Stark shift (30) obtained by neglecting the splitting of the Λ doublet compared to the Stark matrix element (19). Field strengths were chosen to illustrate the breakdown of the linear and quadratic approximations.

IV. EXPERIMENT: PRODUCING COLD NO MOLECULES WITH A STARK GUIDE

One way to produce cold samples of atoms and molecules is to select the cold fraction ($T \lesssim 1\,\mathrm{K}$) of molecules in the Maxwell-Boltzmann speed distribution that emerges from a thermal source. In this approach an atomic or molecular beam is directed into a two-dimensional guide that is bent at an angle such that there is no line-of-sight between the input and output ends of the guide. This guide transmits only particles that move slowly enough to be repelled from the walls by magnetic or electric fields and guided. The feasibility of this method has been demonstrated for Li [66], Rb [67], and H_2CO and ND_3 [68].

In our experimental study of the feasibility of using such a device to produce cold NO we inject NO molecules from an effusive source at 77 K into a *straight*

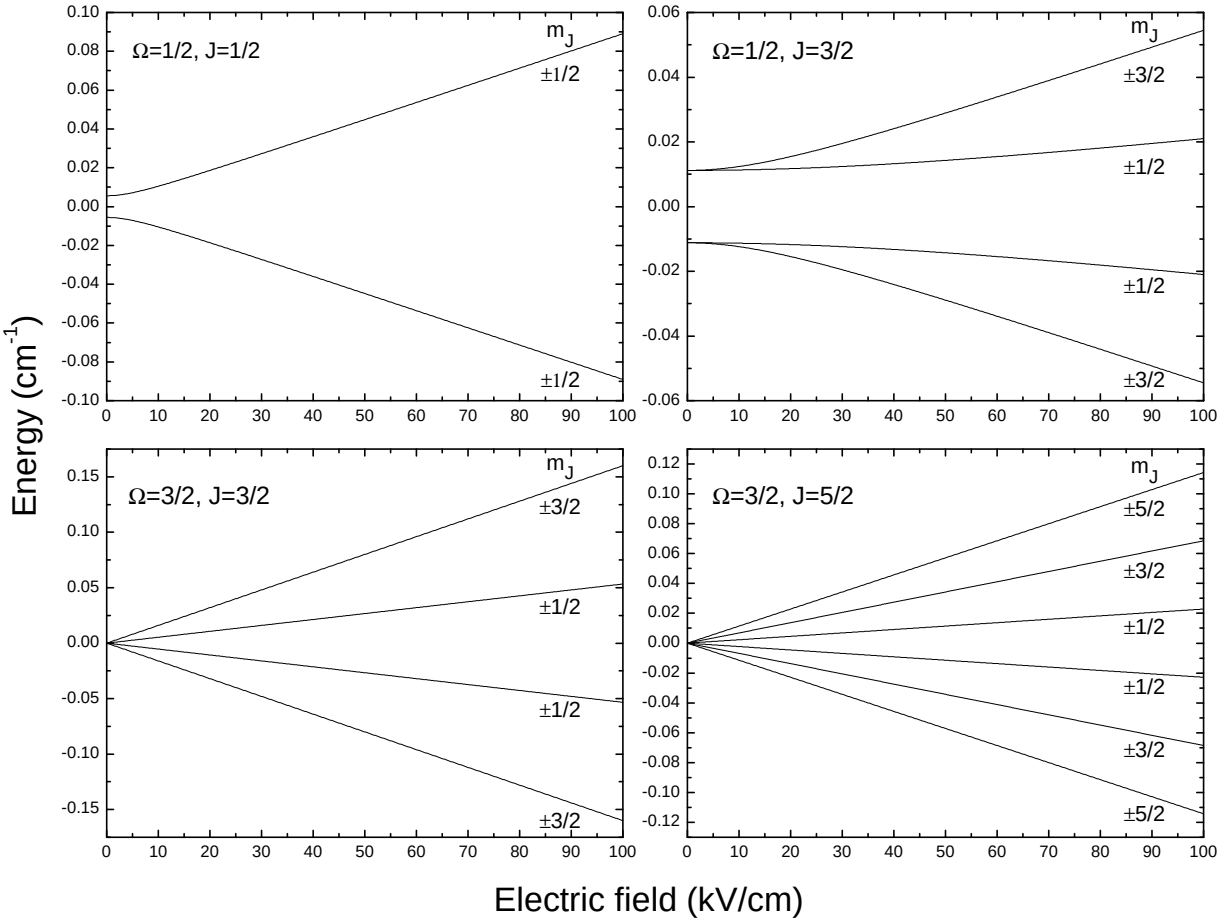

FIG. 3: The dc Stark shifts for the two lowest rotational levels of the ground vibrational manifold of the $\Omega = 1/2$ and $\Omega = 3/2$ states of $N^{14}O^{16}$ as a function of the strength of the applied electric field. In each case, the states whose energies increase with increasing field strength correspond to the zero-field f level of the Λ doublet. Those whose energies decrease with field strength correspond to the zero-field e level. The zero of energy is at the mid-point of the Λ doublet. (The Λ-doublet splitting for the $\Omega = 3/2$ state is not visible on the scale of this figure.)

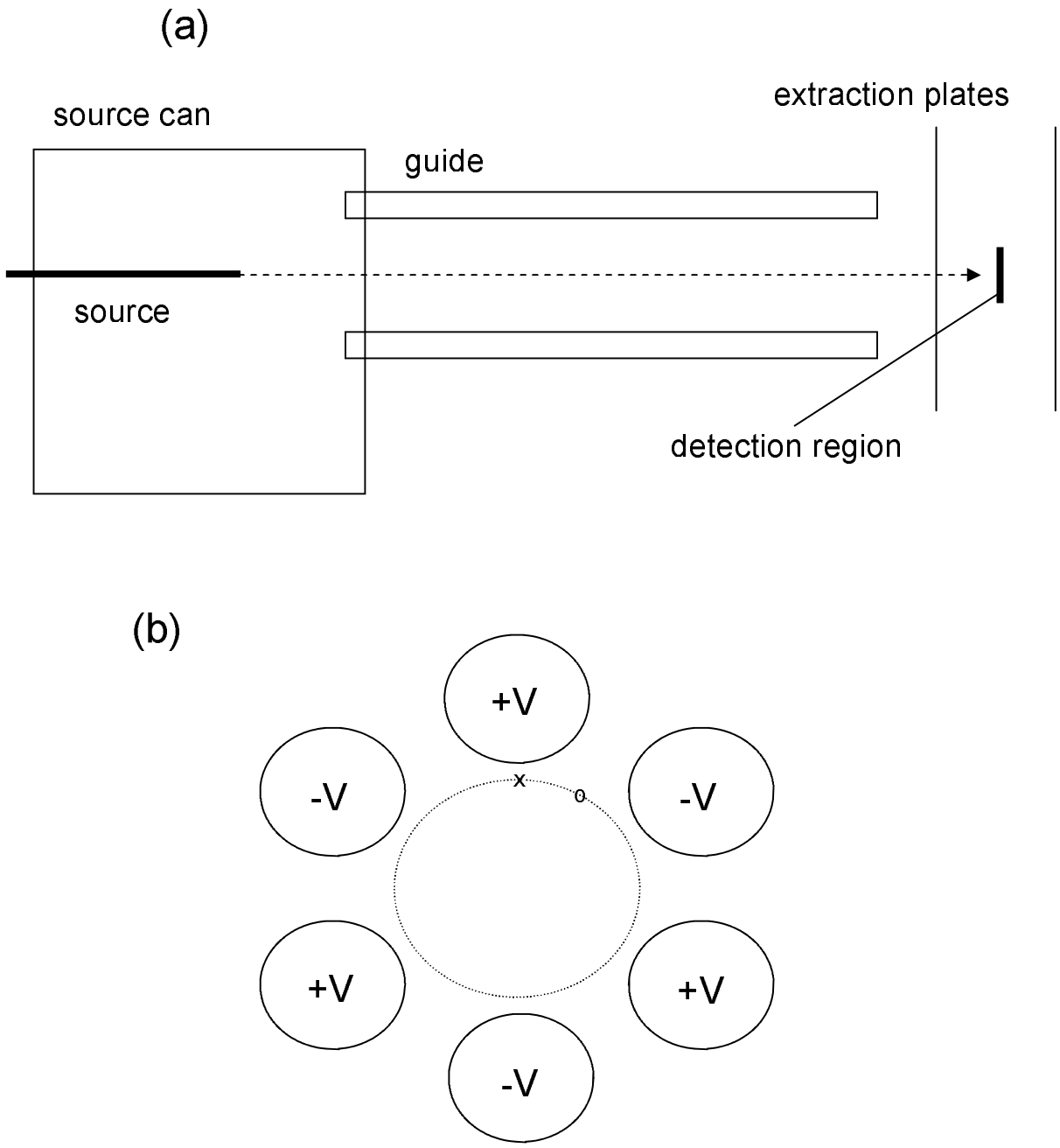

FIG. 4: (a) Schematic of the experimental apparatus (not to scale). (b) Cross section of the hexapole guide. The central circle defines the highest edge of the two-dimensional guide potential. On this central circle the cross and small open circle indicate points of lowest and highest guide potential, respectively, along the edge of the guide.

hexapole Stark guide. As illustrated in Fig. 4a, in this apparatus there does exist a line-of-sight between the input and the output. The hexapole guide, a cross section of which is shown in Fig. 4b, consists of six wires, with positive and negative voltages placed on alternating wires, and produces electric fields as high as 65 kV/cm. Although our objectives are different, our NO guide is functionally identical to the hexapole NO guide used by Stolte and coworkers [69, 70]. The primary difference is that we use a 77 K effusive source, while Stolte and coworkers use a molecular-beam source. The electric field inside the guide is not azimuthally symmetric. Along the circle that defines the highest edge values of the guide potential, the potential energy attains a minimum at each wire and a maximum halfway between each wire (Fig. 4b). Calculating the electric field inside the guide, we find that the easiest escape route for the particles corresponds to a field strength of 35 kV/cm at a guide voltage of 4.5 kV.

Particles whose trajectories are not along a line-of-sight to the output will be guided to the output if their transverse kinetic energy is smaller than the energy of their Stark interaction with the electric field. Due to this collimation effect, the number of molecules at the output will be enhanced. Because the Stark interaction energy is small compared to the average thermal energy of the beam, only the cold fraction is collimated. Further details of the apparatus are described in Ref. [71].

In the present experiments, we observe enhancement of the number of molecules in the lowest rovibrational state of $N^{14}O^{16}$. The particles are detected by exciting the transition $|X^2\Pi_{1/2}, v = 0, J = 1/2\rangle \rightarrow |A^2\Sigma_{1/2}, v = 0, J = 3/2, N = 2\rangle$ at 226.180 nm [72]. The excited A state is then ionized with 327 nm laser radiation, and the resulting cations are detected on a microchannel plate. To measure the effect of the guide on the molecular beam, the number of particles in the $|^2\Pi_{1/2}, v = 0, J = 1/2\rangle$ state is measured as the guide voltage is increased from 0 to 4.5 kV.

We now present data for the enhancement of NO molecules due to passage through the Stark guide. Since this enhancement depends on the Stark interaction, we can use the variation of this quantity with guide voltage to assess the theoretical treatment in Sec. III in the context of experiments on cold molecules. Figure 5a shows the number of ions detected by the microchannel plate. Because fluctuations in the number of detected molecules were smallest at the highest count rates, we normalized the data in this figure to the number of ions detected with maximum voltage applied

to the Stark guide, $V = 4.5\,\mathrm{kV}$.

In each measurement we count the number of ions collected during 320 laser pulses with a particular voltage on the guide, and divide the result by the corresponding number of ions for a voltage of 4.5 kV. In order to determine the statistical error we take ten consecutive measurements of this type. We then repeat this process on several days, adjusting the alignment of the ionizing lasers and the input pressure of NO in order to evaluate systematic errors in the apparatus. The data are subject to a systematic error that is comparable in magnitude to the statistical uncertainty, which we determine by comparing data taken with different configurations. We add the systematic error (in quadrature) to the statistical error to determine the error bars in Fig. 5a, which correspond to a 2-σ confidence interval.

We model the electric field $\mathcal{E}(\mathbf{r})$ using the numerical software program SimION [**?**] including in the model file the conducting surfaces of the source can, the source tube, the guide, and the detection plates. Motion of particles in the guide is calculated by finding the force on the particles, $\mathbf{F} = -\boldsymbol{\nabla} U(\mathbf{r})$, where the potential energy $U(\mathbf{r})$ is given by the Stark shift $\Delta E^{\mathcal{E}}_{v,J,M_J,\Omega}$ of Eq. (24b) as determined using the two-state model of Sec. III A. [The dependence on $\mathbf{r}$ enters the Stark shift through the $\mathbf{r}$-dependent electric field strength, which appears in the matrix element of Eq. (23).] Only molecules in states whose energy energy increases with increasing electric field (so-called "low-field seeking states") are guided. From the potential energy $U(\mathbf{r})$ for our system we create an equivalent electric field for ion propagation in an identical geometry. The SimION program calculates Monte-Carlo trajectories of ions in arbitrary electric fields. So once we have found $U(\mathbf{r})$ for our system, we create an equivalent electric field for ion propagation. Thus, the SimION *ion*-trajectory simulator calculates our *neutral* particle trajectories.

In simulating the output of the guide, we assume that the source provides an isotropic angular distribution, although we considered only particles whose trajectories permitted them to enter the guide. In a previous measurement, we determined that the speed distribution is proportional to $v^2 \mathrm{e}^{-\alpha v^2}$ (where α is constant) as in a standard one-dimensional Maxwell-Boltzmann distribution. The expected speed distribution for the flux from an effusive source is proportional to v^3 [71]. The time during which laser radiation is on, however, is small compared to that required for

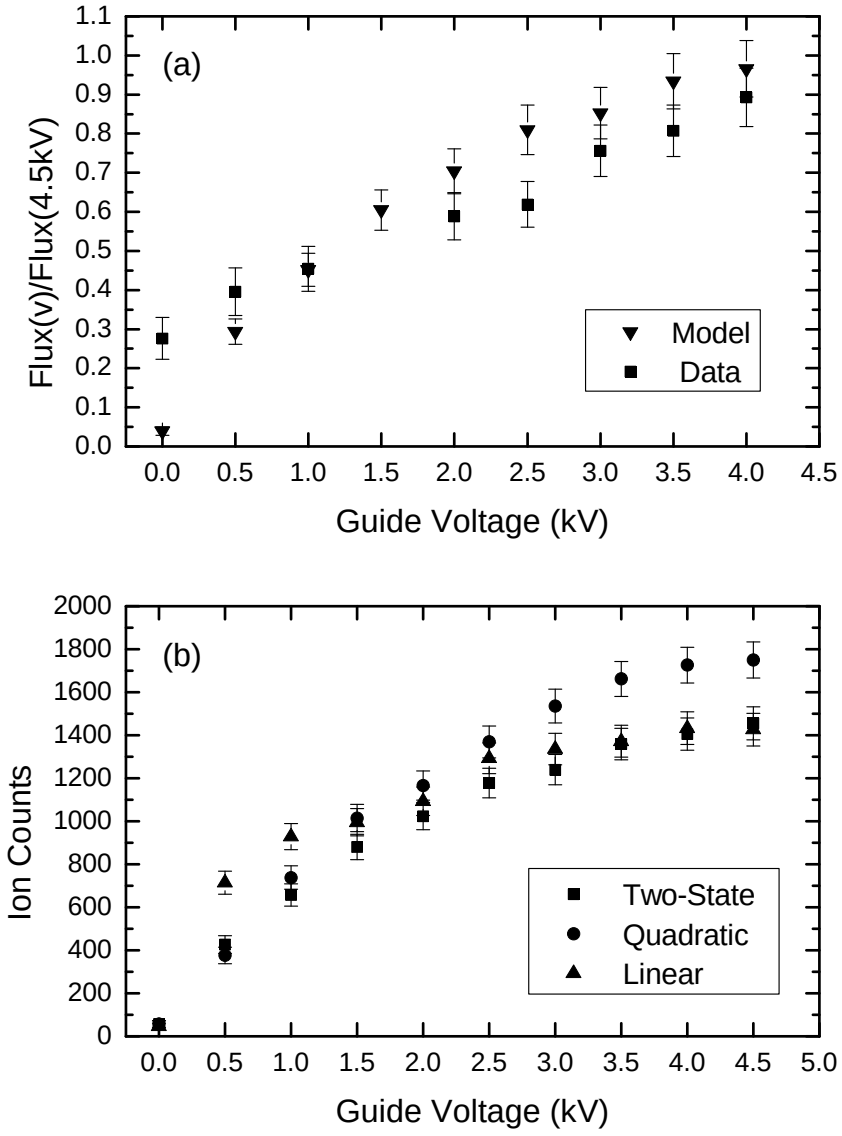

FIG. 5: The flux of particles leaving the guide in the $J = 1/2$ ground rovibrational state as a function of guide voltage. (a) Comparison to measured data. The flux is normalized to the flux at the maximum voltage, 4.5 kV, and the data is compared to *normalized* fluxes calculated using two-state equations for the Stark shift in Sec. III. Note carefully the discussion in the text of the effects of the normalization procedure used in this figure. (b) Simulation of the experiment in which the flux is *not* normalized. The simulated fluxes were calculated using the two-state model and the linear and quadratic approximations.

the particles to undergo any significant movement. Therefore we measure the density directly. Assuming this speed distribution, we found the temperature of the gas to be 77 K, in agreement with a thermistor measurement of the temperature of the source tube. For each voltage on the guide we simulated 20,000 trajectories and counted the number of particles that were successfully guided into the detection region. The result of each simulation at each voltage was divided by the corresponding value for 4.5 kV; as noted above, this step normalizes the data. *Thus, no fitting parameters were involved in generating the comparison in Fig. 5a.*

The error bars for both the experiment and the Monte-Carlo simulations represent a 2-σ confidence interval. As Fig. 5a shows, the model and the data disagree significantly only for a guide voltage of 0 kV. We believe this disagreement results from incomplete modeling of fringing fields at the input. At the input of the guide, a dialectric piece holds the wires in place. This piece will modify the fields at the entrance—an effect that cannot be easily simulated in SimION. Note that this effect is present in all data, since these data are normalized to the output at 4.5 kV. Since improperly modeling the input fields will similarly affect data simulated at different voltages, the largest such effect will appear in data at 0 kV. We conclude, therefore, that the results from the two-state model are consistent with the measured data over the entire range of voltages considered. Unfortunately, the error in the experimental data and the simulations precludes detecting a statistical difference between results calculating using the two-state model and using the quadratic and linear perturbation-theory approximates. This effect is exacerbated by the choice of normalization, which forces all models to converge at a guide voltage of 4.5 kV.

Figure 5b shows a direct comparison—without normalization—of the simulated ion counts assuming the two-state, quadratic, and linear models. The system modeled in this figure is identical to the experimental configuration. For each model, 20,000 trajectories are run for each guide voltage. The error bars correspond to a 2-σ confidence interval, where σ is the square root of the number of ion counts detected. These simulations show clear disagreement between the linear and two-state models at lower fields, and disagreement between the quadratic and two state models at higher fields predicted by Fig. 2.

We conclude that because the two-state model is as easy to implement as the

perturbation-theory equations and does not suffer from breakdown in the relevant range of experimental fields, which in terms of the dimensionless parameter defined in Eq. (31) ranges as high as $\eta = 4.5$ [see Fig. 2], the two-state model should clearly be used in analysis of such experiments.

V. CONCLUSIONS

In previous literature concerning NO, the Stark effect for $^2\Pi_{3/2}$ states has been often described as "linear" and that for $^2\Pi_{1/2}$ states as "quadratic." Each of these characterizations implies a particular perturbative model. We have demonstrated experimentally and theoretically that, for field strengths which are relevant to trapping cold NO these characterizations and the approximations they imply are untenable.

The experimental data in Fig. 5 shows that for NO in its ground state, the first- and second-order approximations (26c) and (27) to the Stark shifts are inaccurate for applied electric field strengths on the order of 100 kV/cm. These observations are elaborated for the *class* of radicals to which NO belongs in Figs. 2 and 3. These figures further show that for such fields the Stark shift in the two-state model, given in Eqs. (24) and in generic form in Eqs. (32), is accurate where perturbation theory is not. (Our results also demonstrate that two previous calculations of Stark shifts are in error[80].) Our two-state equations for the Stark shifts, combined with Eqs. (9) for the rovibronic energies (including spin-orbit and spin-uncoupling effects) and Eqs. (11) for the splitting of the Λ doublet, consistitute an accurate resource for cold-molecule experiments in which the molecules have an odd number of electrons and a $^2\Pi$ ground state.

Acknowledgments

The authors are grateful to Drs. Gregory A. Parker and Jim Shaffer for useful suggestions for improving the manuscript. This project was supported in part by the US National Science Foundation under Grant. PHY-0354858 and by the Office of Naval Research under Grant N00014-02-1-0601.

[1] S. Chu, Rev. Mod. Phys. **70**, 685 (1998).

[2] C. N. Cohen-Tannoudji, Rev. Mod. Phys. **70**, 707 (1998).

[3] W. D. Phillips, Rev. Mod. Phys. **70**, 721 (1998).

[4] E. A. Cornell and C. E. Wieman, Rev. Mod. Phys. **74**, 875 (2002).

[5] W. Ketterle, Rev. Mod. Phys. **74**, 1131 (2002).

[6] J. D. Weinstein, R. deCarvalho, T. Guillet, B. Friedrich, and J. M. Doyle, Nature **395**, 148 (1998).

[7] H. L. Bethlem, G. Berden, F. M. N. Crompvoets, R. T. Jongma, A. J. A. V. Roij, and G. Meijer, Nature **406**, 1558 (2000).

[8] J. L. Bohn, Phys. Rev. A **63**, 052714 (2001).

[9] D. DeMille, Phys. Rev. Lett. **88**, 067901 (2002).

[10] N. E. Shafer-Ray, K. A. Milton, B. R. Furneaux, E. R. I. Abraham, and G. R. Kalbfleisch, Phys. Rev. A **67**, 045401 (2003).

[11] J. J. Hudson, B. E. Sauer, M. R. Tarbutt, and E. A. Hinds, Phys. Rev. Lett. **89**, 023003 (2002).

[12] M. R. Tarbutt, H. L. Bethlem, J. J. Hudson, V. L. Ryabov, V. A. Ryzhob, B. E. Sauer, G. Meijer, and E. A. Hinds, Phys. Rev. Lett. **92**, 17302 (2004).

[13] E. Abraham, B. Bichsel, and N. Shafer-Ray, Bul. Am. Phys. Soc. **48**, 128 (2003).

[14] M. Mizushima, Phys. Rev. **109**, 1557 (1958).

[15] M. Mizushima, *The Theory of Rotating Diatomic Molecules* (John Wiley & Sons, New York, 1975).

[16] C. A. Burrus and W. Gordy, Phys. Rev. **92**, 1437 (1953).

[17] J. J. Gallagher, F. D. Bedard, and C. M. Johnson, Phys. Rev. **93**, 729 (1954).

[18] J. J. Gallagher and C. M. Johnson, Phys. Rev. **103**, 1727 (1956).

[19] C. A. Burrus and J. D. Graybeal, Phys. Rev. **109**, 1553 (1958).

[20] P. G. Favero, A. M. Mirri, and W. Gordy, Phys. Rev. **114**, 1534 (1959).

[21] A. R. Hoy, J. W. C. Johns, and A. R. W. McKellar, Can. J. Phys. **53**, 2029 (1975).

[22] R. A. Frosch and H. M. Foley, Phys. Rev. **88**, 1337 (1952).

[23] M. Mizushima, Phys. Rev. **94**, 569 (1954).

[24] R. Beringer, E. B. Rawson, and A. F. Henry, Phys. Rev. **94**, 343 (1954).

[25] C. C. Lin and M. Mizushima, Phys. Rev. **100**, 1726 (1955).

[26] M. Mizushima, Phys. Rev. **105**, 1262 (1957).

[27] W. L. Meerts and A. Dymanus, J. Mol. Spectrosc. **44**, 320 (1972).

[28] R. Janoschek, Pure Appl. Chem. **73**, 1521 (2001).

[29] G. Herzberg, *Molecular Spectra and Molecular Structure I: Spectra of Diatomic Molecules* (Van Nostrand, New York, 1950), 2nd ed.

[30] A. H. Saleck, G. Winnewisser, and K. M. T. Yamada, Mol. Phys. **76**, 1443 (1992).

[31] M. H. Alexander, R. Pandresen, R. Bacis, R. Bersohn, F. J. Comes, P. J. Dagdigian, R. N. Dixon, R. W. Field, G. W. Flynn, K. H. Gericke, et al., J. Chem. Phys. **89**, 1749 (1988).

[32] E. Klisch, S. P. Belov, R. Schieder, G. Winnewisser, and E. Herbst, Mol. Phys. **97**, 65 (1999).

[33] H. W. Kroto, *Molecular Rotation Spectra* (Wiley, New York, 1975).

[34] J. M. Brown, J. T. Hougen, K. P. Huber, J. W. C. Johns, L. Kopp, H. Lefebre-Brion, A. M. Merer, D. A. Ramsey, J. Rostas, and R. N. Zare, J. Mol. Spectrosc. **55**, 500 (1975).

[35] J. H. Van Vleck, Phys. Rev. **33**, 467 (1929).

[36] R. S. Mulliken and A. Christy, Phys. Rev. **38**, 87 (1931).

[37] R. de Vivie and S. D. Peyerimhoff, J. Chem. Phys. **90**, 3680 (1989).

[38] J. H. Van Vleck, Rev. Mod. Phys. **23**, 213 (1951).

[39] J. D. Graybeal, *Molecular Spectroscopy* (McGraw-Hill, New York, 1988).

[40] P. F. Bernath, *Spectra of Atoms and Molecules* (Oxford University Press, New York, 1995).

[41] H. Lefebvre-Brion and R. W. Field, *Perturbations in the Spectra of Diatomic Molecules* (Academic Press, New York, 1986).

[42] K. P. Huber and G. Herzberg, *Constants of Diatomic Molecules*, Molecular Spectra and Molecular Structure IV (Van Nostrand Reinhold, New York, 1979).

[43] R. N. Zare, A. L. Schmeltekopf, W. J. Harrop, and D. L. Albritton, J. Mol. Spectrosc. **46**, 33 (1973).

[44] S. Green and R. N. Zare, Chem. Phys. **7**, 62 (1975).

[45] R. N. Dixon and D. Field, Proc. R. Soc. London Ser. A **368**, 99 (1979).

[46] M. H. Alexander and P. D. Dagdigian, J. Chem. Phys. **80**, 4325 (1984).

[47] E. Hill and J. H. V. Vleck, Phys. Rev. **32**, 250 (1928).

[48] A. Goldman and S. C. Schmidt, J. Quant. Spectrosc. Radiat. Transf. **15**, 127 (1975).

[49] F. H. Geuzebroek, M. G. Tenner, A. W. Kleyn, and H. Zacharias, Chem. Phys. Lett. **187**, 520 (1991).

[50] W. T. Rawlins, M. E. Fraser, and S. M. Miller, J. Phys. Chem. **93**, 1097 (1989).

[51] A. Amiot, J. Mol. Spectrosc. **94**, 150 (1982).

[52] A. H. Saleck, K. M. T. Yamada, and G. Winnewisser, Mol. Phys. **72**, 1135 (1991).

[53] K. J. Hallin, J. W. C. Johns, D. W. Lepart, A. W. Mantz, D. L. Wall, and K. N. Rao, J. Mol. Spectrosc. **74**, 26 (1979).

[54] H. Margenau and A. Henry, Phys. Rev. **78**, 587 (1950).

[55] C. Amiot, R. Bacis, and G. Guelachvili, Can. J. Phys. **56**, 251 (1978).

[56] A. S. Pine, J. W. C. Johns, and A. G. Robiette, J. Mol. Spectrosc. **74**, 52 (1979).

[57] R. M. Neumann, Astrophy. J. **161**, 779 (1970).

[58] F. P. Billingsley II, J. Chem. Phys. **62**, 864 (1975).

[59] S. R. Langhoff, C. W. Bauschiler Jr., and H. Partridge, J. Chem. Phys. **89**, 4909 (1988).

[60] S. R. Langhoff, C. W. Bauschlicher, Jr., and H. Partridge, Chem. Phys. Lett. **223**, 416 (1994).

[61] W. T. Rawlins, J. C. Person, M. E. Fraser, S. M. Miller, and W. A. M. Blumberg, J. Chem. Phys. **109**, 3409 (1998).

[62] Y. Liu, Y. Guo, J. Lin, G. Huang, C. Duan, and F. Li, Mol. Phys. **99**, 1457 (2001).

[63] M. G. Tenner, E. W. Kuipers, W. Y. Langhout, A. W. Kleyn, G. Nicolasen, and S. Stolte, Surface Sci. **236**, 151 (1990).

[64] T. Helgaker, P. Jørgensen, and J. Olsen, *Molecular Electronic-Structure Theory* (Wiley, New York, 2000).

[65] H. L. Bethlem and G. Meijer, Int. Rev. Phys. Chem. **22**, 73 (2003).

[66] B. Ghaffari, J. M. Gerton, W. I. McAlexander, K. E. Strecker, D. M. Homan, and R. G. Hulet, Phys. Rev. A **60**, 3878 (1999).

[67] E. Nikitin, E. Dashevskaya, J. Alnis, M. Auzinsh, E. R. I. Abraham, B. R. Furneasux, M. Keil, C. McRaven, N. E. Shafer-Ray, and R. Waskowsky, Phys. Rev. A **67**, 045401

(2003).

[68] S. A. Rangwala, T. Junglen, T. Rieger, P. W. H. Pinske, and G. Rempe, Phys. Rev. A **67**, 043406 (2003).

[69] S. Stole, J. Reuss, and H. Schwartz, Physica **57**, 254 (1972).

[70] D. V. D. Ende and S. Stolte, Chem. Phys. **89**, 121 (1984).

[71] B. Bichsel, C. McRaven, M. A. Morrison, N. Shafer-Ray, and E. R. I. Abraham, in preparation (2005).

[72] J. H. M. W Gary Mallard and K. C. Smyth, J. Chem. Phys. **76**, 3483 (1982).

[73] J. T. Hougen, Tech. Rep. 115, Nat. Bur. Stand., Washington D C (1970).

[74] See the special issue on cold polar molecules: Euro. Phys. J. D **31** (2004).

[75] Diverse symbols for this quantity proliferate through the literature, including $\boldsymbol{\jmath}$, **N**, **R**, and **J**. We have chosen **N** because it's the only one of the commonly used symbols that doesn't represent another physical observable.

[76] The operator $\hat{\sigma}_v(xz)$ acts on electronic coordinates in the *molecular* reference frame. But the *conventional* definition of the total-parity operator, which is denoted by $\hat{E}^*$, is the operator that inverts electronic (and nuclear) coordinates *in a space-fixed ("laboratory") coordinate system*. Hougen [73] showed that the effect of $\hat{\sigma}_v(xz)$ on a rovibronic wave function in the molecular frame is equivalent to the action of $\hat{E}^*$ in the laboratory frame. Because electronic wave functions are calculated in the molecular frame, discussions of the parity of molecular wave functions are couched in terms of $\hat{\sigma}_v(xz)$ rather than $\hat{E}^*$.

[77] In earlier literature on Λ doubling [see, for example, Refs. 35, 36], these states were denoted c and d. In this notation, the $|d\rangle$ state of a particular rotational (J) state of a particular spin-orbit electronic state of NO lies above the $|c\rangle$ state. The symmetry properties of these states have been analyzed by Alexander and Dagdigian [46] and an alternative proposed notation in Alexander et al. [31]. In their notation, the Λ-doublet states of the $^2\Pi_{1/2}$ level are denoted $\Pi(A')$ and $\Pi(A'')$, respectively; these designations are reversed for the $^2\Pi_{3/2}$ level.

[78] Note that electric dipole transitions in NO are governed by the selection rules $e \leftrightarrow f$ for the Q branch and $e \leftrightarrow e$ and $f \leftrightarrow f$ for the P and R branches.

[79] The actual basis states for this calculation should be the e/f eigenstates. Strictly, these

states are perturbed by the L-uncoupling operator and so are not actually simple linear combinations of the $|\pm\Omega\rangle$ states as in Eqs. (6b) and (6b). But the off-diagonal matrix elements of the L-uncoupling operator are so small compared to the splitting $\Delta\epsilon^{fe}_{v,J,\Omega}$ between the e and f states that we can neglect the first-order corrections to the perturbed e and f eigenfunctions and use the zero-field states of Eqs. (6b) [see p. 127 of Ref. 41].

[80] Mizushima [14] presents linear Stark shifts for the $J = 1/2, M_J = 1/2$ and $J = 3/2, M_J = 1/2, 3/2$ states. We find his results to be an order of magnitude too large. In addition, Hoy et al. [21] presents a graph of the $J = 3/2$ and $J = 5/2$ rovibrational levels for these two spin-orbit states for field strengths up to 50 kV/cm based on the linear and quadratic perturbation approximations, respectively. For the $^2\Pi_{3/2}$ state, we find that their graphical results is too large by approximately a factor of two.